Exploring Multi-Dimensional Coupling and Information Transfer in a Trapped-Ion Array: A Quantum Network Perspective

Dissertation

zur Erlangung des Doktorgrades der

Fakultät für Mathematik und Physik der

Albert-Ludwigs-Universität Freiburg

universität freiburg

Vorgelegt von:

Deviprasath Palani

Geboren in Villupuram,

Tamil Nadu, India

Betreuer:

Prof. Dr. Tobias Schätz

Zweitbetreuer:

Prof. Dr. Giuseppe Sansone

Dezember 2024

Dekan:	Prof. Dr. Michael Růžička
Erstgutachter:	Prof. Dr. Tobias Schätz
Zweitgutachter:	Prof. Dr. Frank Stienkemeier
Datum der mündlichen Prüfung:	24.02.2025
Prüfungskomitee:	Prof. Dr. Bernd von Issendorff
	Prof. Dr. Heinz-Peter Breuer
	Prof. Dr. Tobias Schätz

Abstract

The limitations of classical computing in predicting the emergent properties of interacting constituents highlight the need for a fully configurable quantum simulator. Many-body physics problems, particularly in higher dimensions and involving long-range interactions, remain challenging to approximate, motivating researchers to develop near-exact simulators for precise configurations.While many researchers pursue different approaches, a fully connected and extendable quantum network that enables quantum state engineering, facilitates interactions, and allows for precise measurement represents a promising architecture for exploring quantum phenomena. The realization of such networks depends on robust quantum state manipulation, precise control over interactions, and efficient state transfer between distributed nodes. Among various platforms, the trapped-ion array platform emerges as a highly suitable candidate due to its unparalleled control fidelity, inherent long-range interactions, and features that enable scalability. Using surface electrode traps fabricated by Sandia National Laboratories, we demonstrate a triangular array with thirteen individual sites located across three layers spanning 40–70 μm. Utilizing the three lowest-lying sites with inter-site distances of 40 μm, prior work in our group demonstrated single-site control, inter-site coupling, and Floquet-engineering coupling. Building on these techniques, we introduce two significant advancements. First, we achieve flexible multi-dimensional steering of phonons via intra-site coupling within individual trapping sites, enabled by a laser-free technique operating in under $100\,\mu$s. Second, we realize deterministic physical transport of ions across a 2D+ array, utilizing ancilla sites, with a transport success rate of 0.99999, while preserving quantum states. These capabilities enrich the trapped-ion array toolbox with additional control and establish it as an extendable quantum network with interconnected distributed nodes, addressing core requirements for modularity and robustness in quantum systems. Efforts to mitigate surface contaminant-related noise using in-situ cleaning techniques have not yet achieved significant noise reduction. However, detailed characterization of technical noise sources provides insights into motional mode heating and informs strategies for improving system stability. These advancements lay the foundation for extendable, multi-dimensional architectures for quantum simulations, enabling the exploration of multi-dimensional quantum phenomena, as well as applications in computation and precision metrology.

Table of Contents

1 Introduction

To explain the dynamics of microscopic systems (constituents), quantum theory currently provides the most effective approach. However, the complexity and limitations of numerical methods in simulating many-body interactions and predicting emergent properties, especially in higher spatial dimensions, call for a different method. A fully connected, reconfigurable quantum network with distributed nodes for quantum processing represents a natural extension of the foundational principles suggested by Feynman, who envisioned a quantum device governed by quantum mechanics to understand such interactions [1, 2]. Whether utilized for digital quantum simulation (DQS) or analog quantum simulation (AQS), such a device must meet the following requirements, as proposed by DiVincenzo [3] and Cirac et al. [4]: (1) A quantum system with many constituents, such as bosons and/or fermions; (2) Initialization of simple quantum states; (3) Engineering of interactions among constituents; (4) High-fidelity measurement of outcomes; and (5) Verification of results. Numerous platforms have been proposed to fulfill these requirements, as reviewed by Georgescu [5]. These approaches can be broadly classified into two categories: (1) Small-scale systems designed to control many constituents, such as photons (bosons) [6] and electrons [7], which have demonstrated near-ideal analogues at finite scales; and (2) Large-scale systems targeting individual control, such as platforms utilizing artificial atoms like superconducting qubits [8] and quantum dots [9], which currently face challenges in replicating ideal indistinguishable constituents. Cold-atom-based platforms offer complementary capabilities, initializing large identical lattices [10] and arranging them into arbitrary configurations for short durations of few seconds. Progress in cold-atom systems has enabled the study of higher spatial dimensions [11], paving the way for exploring multi-dimensional many-body problems, such as bilayer systems [12, 13].

A quantum network comprises interconnected nodes capable of performing quantum state engineering, including entanglement distribution. Trapped-ion systems are highly suitable candidates for these nodes, offering state-of-the-art control fidelities, inherent long-range interaction capabilities, and versatility in quantum state manipulation. Unlike many small-scale systems, trapped ions excel as both local node processors and effective communication channels for high-fidelity information transfer. They bridge the gap between quantum simulation and communication network architectures [14–17], thereby fulfilling many of the essential requirements. Additionally, trapped ions inherently combine two quantum degrees of freedom: electronic states (fermions) and motional states (bosons), forming a built-in analog hybrid that enables the verification of various fundamental interactions [16, 18]. Their uniquely controllable nature makes trapped ions indispensable tools for probing complex dynamics [19], performing precision metrology of otherwise inaccessible systems [20, 21], and integrating into hybrid plat-

forms [22–24]. Among the many approaches pursued with trapped ions, two key strategies offer essential tools for realizing networked architectures:

1. **Bottom-Up Approach:** Advances in fabrication technology have provided the tools necessary for scalable trapped-ion systems [25]. Following Wineland et al.'s suggestion [15], researchers have addressed scalability using the quantum charge-coupled device (QCCD) architecture. This method splits large 1D Coulomb crystals of ions into functional few-ion systems, physically transporting them to perform different tasks in parallel [26–28]. Such systems are well-suited for DQS, leveraging the current best two-qubit gate fidelities.

2. **Top-Down Approach:** This approach focuses on enabling individual addressing within large ensembles of ions, including long ion chains in a common potential [29], 2D crystals [30–32], and 2D crystals in Penning traps [33]. Recent efforts have expanded this approach to explore additional spatial dimensions, such as bilayer systems [34], laying the groundwork for simulating multi-dimensional quantum phenomena.

Although there are proposals for simulating multidimensional systems in 1D crystals [35], an AQS device with a near-exact lattice design tailored to specific configurations offers a complementary approach to results from other platforms [36]. By leveraging the long-range Coulomb interaction capabilities of trapped ions, a fully configurable AQS for higher spatial dimensions requires significantly fewer resources than a DQS [37]. A trapped-ion array platform with multiple sites is particularly well-suited for simulating a variety of interesting physical models [24, 38], operating without critical error-correction requirements, while also serving as a promising prototype for quantum network devices. Most of the approaches mentioned above, however, work with or have been implemented using linear arrays of trapped ions, limiting their ability to simulate multidimensional phenomena directly. Using advanced fabrication techniques, initial attempts to realize two-dimensional trapped-ion arrays achieved inter-site distances of approximately 50 μm, enabling the first investigations of dipole-dipole interactions via Coulomb forces [39, 40]. In our group, surface-electrode traps fabricated by Sandia National Laboratories in collaboration with the NIST ion storage group were used to develop a 2D trapped-ion array platform. The electrodes were optimally shaped [41] to create an array of 13 confined sites arranged in three distinct layers, hovering 40–70 μm above the fabricated surface. Exploiting the three lowest-lying trapping sites, which form an equilateral triangular array with side lengths of 40 μm, this platform was introduced to investigate prototype 2D physics, including frustrated spin systems and Aharonov-Bohm physics. In addition, Mielenz, Kalis, Hakelberg, and Kiefer et al. in our group enriched the 2D trapped-ion array toolbox by demonstrating individual control of trapping sites with low crosstalk [42, 43], realizing 2D inter-site interactions [44], and engineering directional control over phonon-mediated coupling within 2D arrays [45]. These

advancements established the foundation for further exploration of multidimensional quantum phenomena and contributed to the development of trapped-ion arrays as promising candidates for modular and extendable quantum networks.

In this thesis, we explore a trapped-ion array as a small-scale quantum network platform, emphasizing its potential for investigating multi-dimensional quantum phenomena and advancing the capabilities of quantum networks. With inter-ion spacings of 15–40 μm, this system provides unparalleled control over quantum interactions, enabling the study of fundamental processes critical to understanding and scaling towards large quantum systems. Chapter 2 and Chapter 3 describe the experimental platform based on surface-electrode traps and detail the methods for controlling individual ions and exploiting all available degrees of freedom. From a quantum network perspective, this work contributes by demonstrating two novel techniques that enhance the scalability and modularity of the trapped-ion array platform, paving the way for robust quantum state transfer and entanglement distribution across interconnected nodes. First, in Section 4.1, we implement intra-site coupling of motional degrees of freedom, a key technique for steering phonon-mediated interactions within a site. This laser-free approach enables efficient state manipulation, dynamic control, and routing of quantum information, ensuring flexible connectivity across the network. Section 4.1.2 further explores its application in preparing simple motional quantum states. Second, in Section 4.2.2, we achieve deterministic inter-site transport inspired by quantum charge-coupled device (QCCD) architectures. By incorporating an additional site positioned 10 μm above the triangular 2D array, we extend the array to a 2D+ configuration, preserving quantum states during transport with high fidelity. These efforts are analyzed in Section 4.2, offering insights into the system's stability and operational limits. Together, these implementations advance the trapped-ion array as a modular, scalable, and extendable quantum network prototype. At micrometer-scale distances, the interplay between interaction strength, fidelity, and noise presents unique challenges. Section 4.3 addresses these issues through noise characterization and mitigation efforts, including argon-ion sputtering to reduce motional heating. These developments establish a foundation for extending trapped-ion arrays into multilayer configurations, enabling the exploration of complex, higher-dimensional quantum behaviors [13, 34]. Furthermore, this work positions the trapped-ion array as a complementary platform operating at micrometer scales, excelling in precision and controllability. It serves as an ideal candidate for exploring quantum phenomena, verifying results [46], and extending the system with a quantum network approach toward large-scale quantum systems. The techniques demonstrated here, such as coherent ion transport and precise control of motional states, could be foundational for realizing quantum repeater nodes, distributed quantum processors, and hybrid architectures that integrate trapped-ion systems with photonic [23] or superconducting qubits [47].

Personal contributions: 2019-Present

In late 2019, I inherited the experimental setup (AnlageH), including the hybrid magnetic field [48], and the optical setup from Dr. Frederick Böckling (also known as Hakelberg) and Dr. Philip Kiefer. The optical setup comprises two infrared fiber lasers, two additional lasers shared with another experiment, 14 acousto-optic modulators, five frequency-doubling cavities, and an experimental control system. I used these setups to perform argon-ion treatments on a linear trap. Since 2020, I have worked with four different surface-electrode traps, handling commissioning, calibration, experiment execution, and data analysis under the supervision of Prof. Dr. Tobias Schätz and Dr. Ulrich Warring. I gained expertise in UHV techniques under the guidance of Dr. Frederick Böckling and Jörn Denter. Alongside Dr. Philip Kiefer, we calibrated the argon sputtering gun, learned to handle frequency-doubling cavities, experimental control, and optimized optical beam paths. With the help of Lennart Guth and Dr. Ulrich Warring, we transferred the triangular array to the AnlageH setup. There, I calibrated the system and performed transport experiments using tools developed by Dr. Philip Kiefer, Dr. Frederick Böckling, and Jan-Philipp Schröder, as published in [49]. Inspired by [50, 51], I implemented multi-mode coupling in a trapped-ion array and conducted preliminary tests. I achieved three-dimensional motional ground-state initialization at a single site, with the potential to extend this across the entire array. I have completed more than 100 iterations of argon-ion treatments on four different traps and studied motional mode variations due to surface modifications (a journal article in preparation). Furthermore, I have integrated compatible instruments into a centralized system (ARTIQ) capable of controlling advanced trap architectures with nearly 100 electrodes [52] to support future experimental demands. I have commissioned and maintained database infrastructure (InfluxDB), interfacing it with the current data management system and an in-house-maintained messaging/logging platform (Mattermost). I also developed semi-automated features to enhance precautionary measures. As part of the ion trapping section, I participated in discussions concerning experiments and provided technical support for the Paul trap experiment (Paula).

I also contributed to the Master's Laboratory course, helping to commission two experiments, *Diamonds* and *Electromagnetically Induced Transparency* (*EIT*), into the FP (Lab course) catalog. For the *Diamonds* experiment, under the supervision of Dr. Ulrich Warring, I implemented and benchmarked the ARTIQ [53] system with NV centers as part of my Master's thesis. we commissioned the lab course experiment and provided a fully online-compatible setup. For the EIT experiment, designed by Dr. Daniel von Schönfeld under Dr. Leon Karpa's supervision, I aligned optical elements and designed LabVIEW-based programs for controlling instruments. We observed EIT spectra, used it as quantum memory (light storage), and published its metrology applications [54] (not part of this thesis).

List of Publications

1. D. Palani, F. Hasse, P. Kiefer, F. Boeckling, J.-P. Schroeder, U. Warring, and T. Schaetz, "High-fidelity transport of trapped-ion qubits in a multilayer array," *Phys. Rev. A*, vol. 107, no. 5, p. L050601, May 2023.
https://doi.org/10.1103/PhysRevA.107.L050601

2. D. Palani, D. Hoenig, and L. Karpa, "In situ ac Stark shift detection in light storage spectroscopy," *Journal of Physics B: Atomic, Molecular, and Optical Physics*, vol. 54, no. 16, p. 165402, Sep. 2021.
https://doi.org/10.1088/1361-6455/ac2001

3. F. Hasse, D. Palani, R. Thomm, U. Warring, and T. Schaetz, "Phase-stable traveling waves stroboscopically matched for superresolved observation of trapped-ion dynamics," *Phys. Rev. A*, vol. 109, no. 5, p. 053105, May 2024.
https://doi.org/10.1103/PhysRevA.109.053105

In preparation

1. A. Colla, F. Hasse, D. Palani, T. Schaetz, H-P. Breuer, and U. Warring, "Observing Time-Dependent Energy Level Renormalisation in an Ultrastrongly Coupled Open System".
https://doi.org/10.48550/arXiv.2408.15928

2. D.Palani, F. Hasse, P. Kiefer, F. Boeckling, U. Warring, and T. Schaetz, "In-Situ Argon-Ion Treatment of multi-material layered surface-electrode traps," ***in preparation***.

2 Experimental Setup & Control

In this chapter, we present the core components and control systems built around surface electrode traps with a focus on extending the ion-trapping array using a bottom-up approach. This setup supports precise ion storage, manipulation, and data acquisition systems essential for scaling to larger arrays. We begin by detailing the ion trapping hardware in Section 2.1, which includes surface electrode traps, an ultra-high vacuum (UHV) chamber, and detection systems for stable confinement. The next section, Control Fields (Section 2.2), describes the laser systems, radio-frequency (RF) fields, and microwave sources necessary to address the electronic and motional states of the ions, all engineered for stable and precise control to support integration in larger ion arrays. Finally, we outline the control interface and data acquisition system in Section 2.3, which includes the experiment input and output system (EIOS) and time series databases for real-time monitoring, efficient data handling, and scalable experimental control. Together, these systems provide a robust foundation for extending the trapped-ion array with a modular bottom-up strategy.

2.1 Ion Trapping Hardware

This section provides an overview of the hardware required for a trapped-ion array, including the surface electrode traps from Sandia National Laboratories housed within an UHV chamber to ensure isolation for ion control. Two distinct trapping architectures are used: a triangular array and a linear trap, each selected for specific experimental configurations. We also describe the setup within the UHV chamber, which includes ports and feedthroughs for control fields as well as the detection setup for resolving individual ions and collecting experimental data.

2.1.1 Surface Electrode Traps

We use surface electrode traps manufactured by Sandia National Laboratories [55] in collaboration with NIST. Two types of trap architecture are used: 1) a triangular array and 2) a linear trap. Figure 1 shows the chip carrier with triangular arrays fabricated using multilayered complementary metal-oxide-semiconductor (CMOS) metal technology. In Fig. 1a, two triangular arrays are shown: a 80-µm array [42, 56] and a 40-µm array [44, 45], positioned approximately 3.5 mm apart on a carrier 10 mm × 10 mm. For trapping operations, only one array can be used at

a time; for this work, we primarily use the 40-µm array. The zoomed image in Fig. 1a (bottom-left) shows the 40-µm array with two distinct RF electrodes, each with a unique shape, along with 30 segmented electrodes in the top metal layer. The unique shape of the RF electrodes is designed to create an array of individual trapping sites forming an equilateral triangle with a side length of 40 µm, using the Gapless Approximation algorithm [57] to allow basic 2D quantum simulations [58] with control over individual constituents. Briefly, the gapless approximation algorithm assumes that there are no gaps between electrodes, still treating electrodes as mutually isolated and that all electrodes are on the same plane, calculating the resulting potential and gradients at the position of the minimum due to finite potentials applied to selected electrodes.

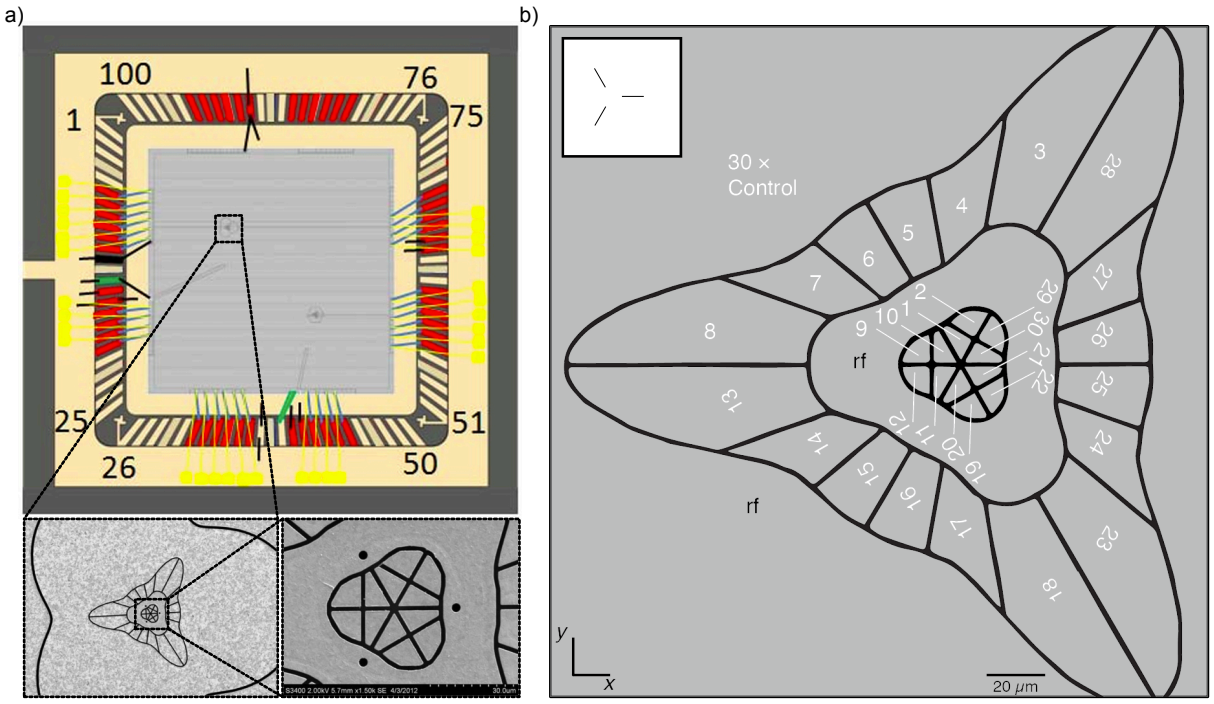

Figure 1: 40-µm triangular array. Panel (a) shows the 10 mm × 10 mm chip carrier with a 40-µm and an 80-µm array positioned approximately 3.5 mm apart, off-centered. The bottom-left image shows a zoomed-in view of the 40-µm array with the outer and inner RF electrodes, along with the segmented control electrodes. Another close-up image on the bottom-right provides a detailed view of the inner segmented control electrode and loading holes, which form an equilateral triangle with a side length of 40 µm, marking the pseudo-potential minima for trapping three ions to create a triangular array. Panel (b) shows the segmented electrodes labeled with corresponding numbering, connected to feedthroughs for control via upstream electronics. The top-left schematic depicts the empty array with lines connecting all four trapping sites, including the lower-lying triangular sites and an ancillary site, indicating the positions of individual trapping sites. This schematic will be used in later sections to indicate platform information relevant to the corresponding experiment.

We use multi-metal layer traps (up to 4 layers), fabricated using CMOS and micro electronic

mechanical systems (MEMS) technology. The top layer is coated with $\approx$ 50 nm gold, underlaid by a platinum-titanium composite layer of $\approx$ 50 nm, which serves as a diffusion barrier. Beneath this, a thick aluminum layer is deposited over a dielectric substrate. Additional metal layers cover exposed dielectric regions, effectively shielding trapped ions from external noise. As shown in Fig. 1a (bottom right), electrode islands are connected via long vias that extend up to approximately 10 µm in length, to ensure electrical connectivity. Each control electrode is equipped with an on-board capacitor 820 pF to suppress RF voltage pickups. The electrodes, depicted in Fig. 1a, are wire-bonded to the pads of a ceramic pin grid array (CPGA) to enable external connectivity. Figure 1b shows a close-up image of the segmented control electrodes, which are used to provide stable potential configurations and to coherently manipulate trap frequencies. Using these electrode labels, we calculate the potentials required to be applied to each electrode to efficiently manipulate the trapping parameters.

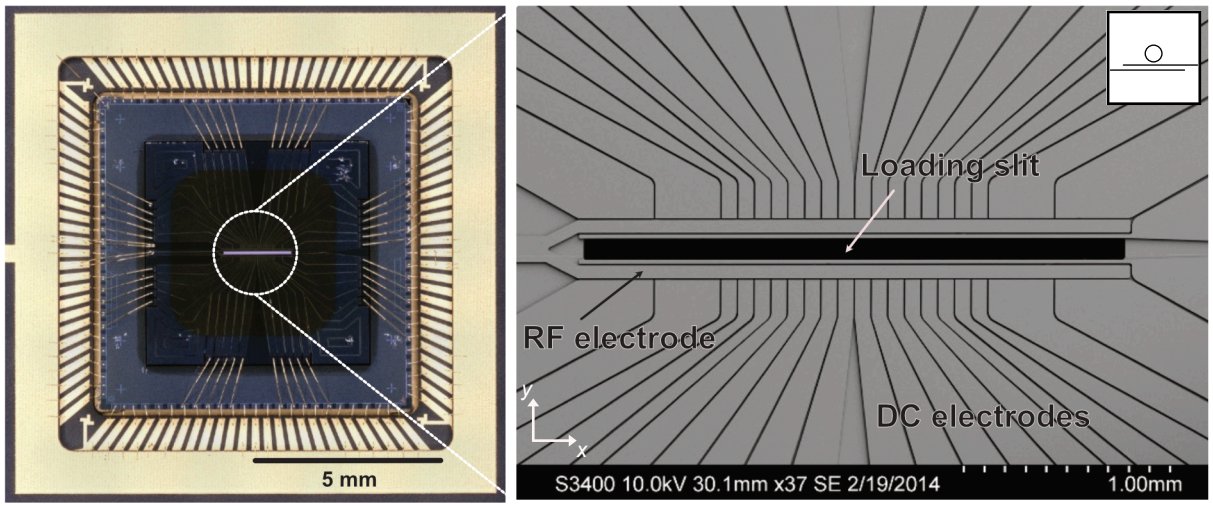

Figure 2: Linear trap array. The left image shows a composite multi-layered linear trap fabricated by Sandia National Laboratories. It is wire-bonded to a 10 mm $\times$ 10 mm chip carrier, providing 42 active connections to control electrodes and an RF electrode for trapping, storing, and manipulating potentials for the trapped ions. The right image offers a closer view of the loading and experimental zone, featuring a loading slit that allows hot vapor from the resistive oven positioned beneath to access the trapping region. A pair of long rails, marked as the RF electrode, is supplied with an oscillating potential to enable confinement in two radial directions (perpendicular to the RF rails). Along the axial direction, confinement is provided by a DC electric field generated by a combination of potentials applied through all control electrodes to establish a stable axial trapping field. The top-left schematic depicts the linear array and will be referenced in later sections when discussing corresponding experiments.

Similarly, a linear trap (referred to as Thunderbird or Eurotrap) [59–61] is also used in our experimental setup. Figure 2 shows the 10 mm $\times$ 10 mm chip carrier with linear trap. The zoomed image reveals a single RF electrode split into two rails (resembling a tuning fork) to create a pseudo-potential minimum parallel to the RF rails, approximately 83 µm above the

electrode. Axial confinement is achieved by static potentials generated through multiple control electrodes. The trap includes 42 control electrodes to fine-tune potentials and gradients. As shown in the close-up image, a long slit in the middle of the RF electrode allows the hot vapor of the atomic candidate to access the trapping region. Like the triangular array, this linear trap features an on-board 1 nF capacitor to filter noise and suppress unwanted pickups. Our experimental setup accommodates both trap architectures with minimal modifications to the software configurations.

2.1.2 Vacuum and Detection Assembly

To commission surface electrode traps and facilitate light-matter interactions, we use a custom-made UHV chamber, as shown in Fig. 3. This chamber features a monolithic design with six windows optimized via anti-reflection(AR) coatings for UV lasers at wavelengths around $\lambda \approx 280\,\text{nm}$, essential for experimental operations. Positioned in the center of the chamber, the chip traps are driven by a RF signal via a high quality helical resonator (marked 4). Additional feedthroughs provide access to other controllable components, such as control electrodes for trap parameter adjustments and a magnesium source for ionization. To achieve UHV conditions, we employ a combination of a turbomolecular pump[1] (marked 1), an ion getter pump[2] (marked 5), and a titanium sublimation pump (marked 6), reaching pressures as low as 10^{-11} mbar. This vacuum level is monitored by an ion gauge (marked 7), with a noise floor near 10^{-11} mbar. The magnified view in Fig. 3 also highlights two permanent magnets (Magnets I and II) generating a stable 10.95 mT magnetic field, setting the quantization axis $\vec{B}$. Three pairs of coils mounted along each axis enable fine-tuning of the magnetic field, compensating for drifts due to environmental fluctuations. The overlaid diagram also shows laser paths, including Doppler cooling, repumping, and Raman beams, each entering through specific windows to meet geometric requirements for their intended interactions.

Figure 4 illustrates the custom-designed chip holder, built in-house to host surface electrode traps fabricated by Sandia National Laboratories. A gold-plated metal component, commonly referred to as a mask (marked 1), serves as both a shield against electrical noise and a source of global potential, applied through a dedicated electrical connection (marked 4). The mask is electrically isolated from other components using PEEK spacers[3]. In the center of the mount is a $10\,\text{mm} \times 10\,\text{mm}$ CPGA socket with 104 pin slots, designed to support advanced traps with up to 100 control electrodes [55]. Although our setup requires no more than 42 connections, this configuration allows flexibility for future expansions. Each required pin is connected to the UHV

[1] Agilent TwisTorr 304FS
[2] Agilent VacIon Plus 300 Starcell
[3] Polyether ether ketone (PEEK) is a stable insulating material compatible with UHV conditions.

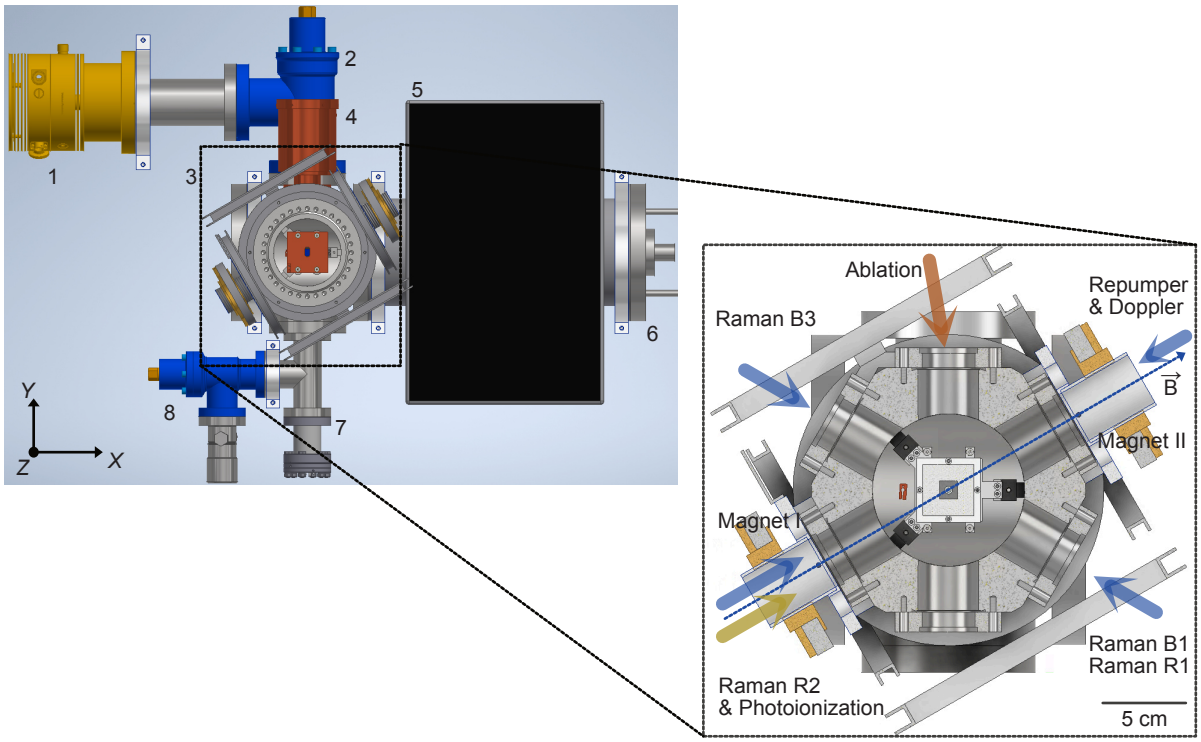

Figure 3: Ultra-High Vacuum (UHV) chamber with beam configuration. The left image shows a top view of a technical rendering of the UHV chamber and its peripheral components: 1) a turbo-molecular pump connected to a scroll pump, achieving pressures around 10^{-9} mbar; 2) a corner main valve for sealing the chamber; 3) a hexagonal monolithic chamber with a chip holder and six windows, optimized via anti-reflection (AR) coatings in the UV range, providing laser access essential for light-matter interactions; 4) a high-quality helical resonator (in red) to drive the traps with a radio frequency; 5) an ion-getter pump to remove getterable materials, reaching pressures as low as 10^{-11} mbar; 6) connectors for a titanium sublimation pump; 7) an ion gauge to monitor chamber pressure, with a noise floor around 10^{-11} mbar; and 8) an additional inlet and precision valve for controlled inert gas input during specific procedures. The zoomed image provides a cross-sectional view, illustrating permanent magnets (in yellow) that generate a stable magnetic field $\vec{B} \approx 10.95\,\text{mT}$, setting the quantization axis. Three pairs of coils mounted along each axis enable fine-tuning of the magnetic field. The laser configuration includes Doppler cooling and repumping beams, polarized along the $\vec{B}$ axis. Four Raman beams (B_1, R_1, R_2, B_3) enter through three windows to meet geometric requirements for light-matter interactions. Additionally, an ablation laser (in red) and a photo-ionization beam (in yellow) facilitate the production and ionization of magnesium atoms to generate ions.

feedthrough using Kapton insulated[4] wires to maintain stable control of the trap electrodes within the UHV environment. To produce magnesium ions, we use two loading methods. The first is a magnesium wire wrapped around a pillar (marked 2) approximately 10 mm from the trapping site, supporting laser ablation loading. The second method uses a resistive oven in a fused silica enclosure (marked 5) containing two magnesium wires. By passing currents of 1 to 5 A, the oven generates a controlled vapor of magnesium, which enters the trapping region through designated loading holes or slits for the photo-ionization process. These dual mechanisms enable precise and reliable ion loading, ensuring experimental consistency.

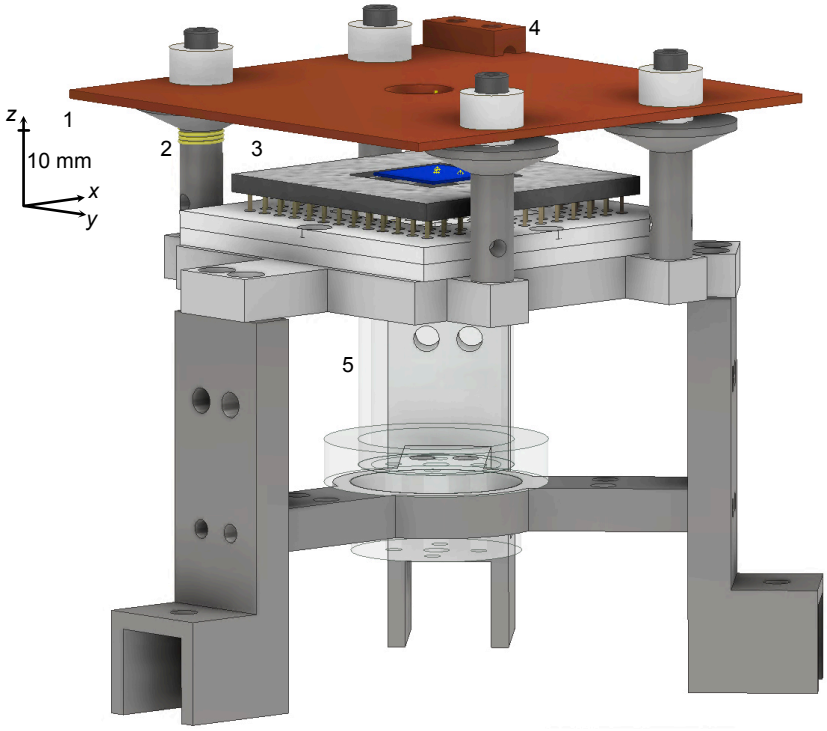

Figure 4: Chip holder and its peripherals. Positioned at the center of the UHV chamber, supported by three metal brackets attached to the chamber. 1) A metal mask that acts as both a shield against electrical noise and a provider of global potential in the Z-direction. It also contains holes to facilitate access, such as for collecting light from the trapped ions for imaging or photon counting. 2) Magnesium wire (shown in yellow for clarity; actual color is similar to gray-white): three turns wound around a pillar approximately 10 mm from the trapping site. 3) A $10\,\text{mm} \times 10\,\text{mm}$ chip carrier capable of hosting up to 104 pins. In this setup, up to 50 pins are connected to two feedthroughs (two D-sub 25-pin connectors), which are sufficient to operate the two surface electrode traps fabricated by Sandia National Laboratories. 4) A connector to bias the metal mask. 5) A resistive oven housing two magnesium wires in a fused silica enclosure, which can be heated on demand by passing currents ranging from 1 to 5 A for up to a few minutes to produce hot magnesium vapor through loading holes or slits for subsequent photo-ionization.

Figure 5 provides a lateral view of the detection setup, highlighting the optical components of

[4]Kapton is a high-temperature polyimide material suitable for vacuum insulation.

the detection and imaging system. The setup is mounted on a custom UHV top flange supporting a tilted beam path, designed to integrate additional in-vacuum equipment, such as a sputtering gun positioned at a 30° angle for applications like surface cleaning. The detection system consists of an electron multiplying charge-coupled device (EMCCD)[5] (marked 1) to spatially resolve multiple ion configurations and a photon multiplier tube (PMT)[6] (marked 2) for high-temporal-resolution photon counting during experimental sequences. A motorized flipper mirror facilitates on-demand switching between the EMCCD, used for ion loading, and the PMT, used for high-speed photon detection, eliminating the need for manual adjustments and improving operational efficiency. A secondary optical table (marked 3) holds the optics to direct and reshape laser beams through specific chamber windows, ensuring precise ion-laser interaction. The main collection objective[7] is tilted at 16°, allowing light collection while accommodating other vacuum equipment. Positioned approximately 50 mm from the ions, this objective achieves a 40x transverse magnification with a resolution of $0.32\,\mu\text{m}$/pixel at the EMCCD, sufficient to resolve the ions at a close spacing. An optical bandpass filter[8] blocks stray light from external sources before the flipper mirror, enhancing the signal-to-noise ratio during fluorescence detection. Although the tilted configuration supports additional in-vacuum equipment, such as the sputtering gun, it results in a minor reduction in collection efficiency. Overall, this set-up is optimized for spatially resolved ion imaging, high-speed photon detection, and versatile in-vacuum functionality such as in-situ sputtering, meeting the requirements for precise and complex experimental operations.

[5] iXon Ultra 888
[6] Hamamatsu H8259-02
[7] Sill Optics S6ASS2060/199, effective focal length 57.3 mm at 266 nm UV
[8] Schott UG5

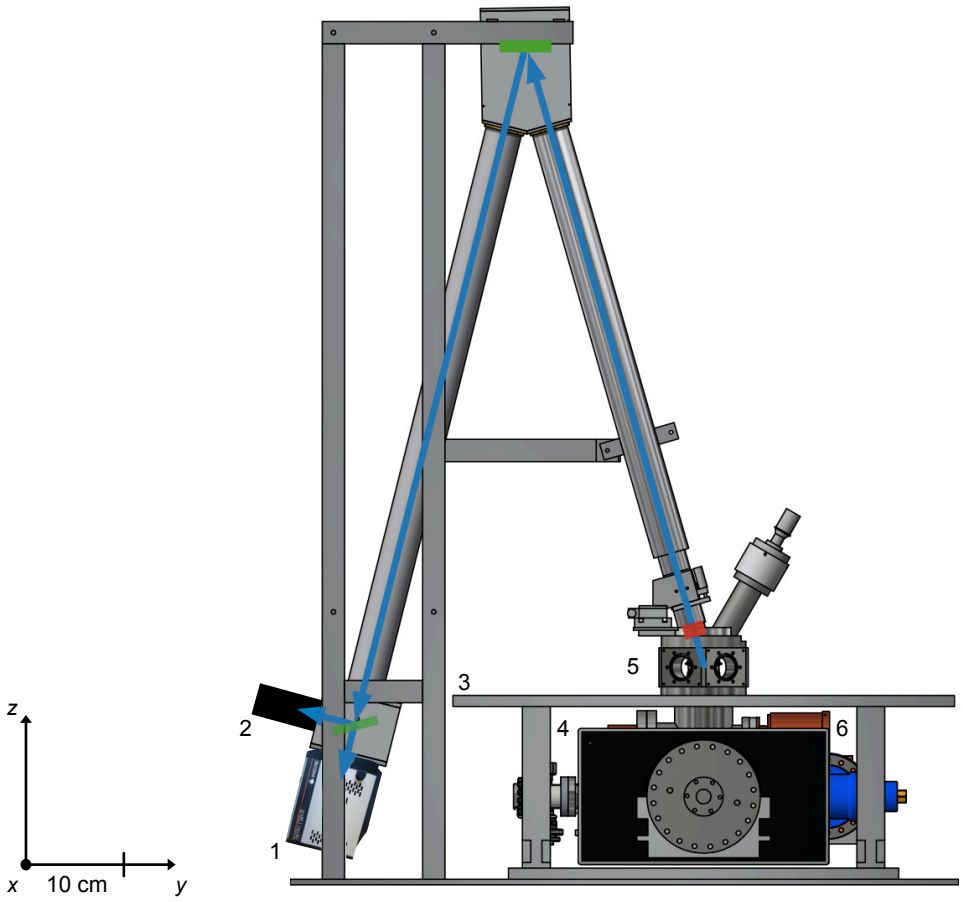

Figure 5: Imaging optics: lateral view of the setup. Image adapted from the thesis of Hakelberg [62]. 1) An electron multiplying charge coupled device (EMCCD), part of the imaging system with a magnification of 40x, to resolve trapped ions with a resolution of $0.32\,\mu$m/pixel. 2) A photon multiplier tube, part of the detection system, to count photons resulting from an experiment. A flipper mirror is used to direct photons either to the EMCCD or to the PMT. 3) A second optical breadboard to host optics near the chamber windows for addressing light-matter interactions with trapped ions. 4) An ion getter pump (IGP) and titanium sublimation pump (TSP) for achieving ultra-high vacuum pressures. 5) The chamber with six windows for light access. 6) A helical resonator with high Q for the radio-frequency drive.

2.2 Control Fields

In this section, we document all sources of control fields, ranging from DC to 10^{15} Hz (lasers), required to enable a trapped ion oscillator. The first subsection describes the laser sources and associated peripherals used to control the electronic degrees of freedom of a $^{25}Mg^{+}$ ion. Following this, we outline the instrumentation for the RF field for ion trapping, the generation of arbitrary waveforms to enable and manipulate the motional degrees of freedom, and the microwave circuitry to address the hyperfine sublevels of the $^{25}Mg^{+}$ ion.

2.2.1 Laser Systems

In our experiments, $^{25}Mg^{+}$ ions were selected as the trapped ion candidate. Figure 6 illustrates the relevant transitions and their labels in a quantization field of 10.95 mT. The nuclear spin ($I = 5/2$) of ^{25}Mg causes a hyperfine splitting in the ground state, producing two energy levels: $F = 2$ and $F = 3$. This quantization field further raises the degeneracy of the energy levels as a result of coupling to the magnetic field, resulting in distinct sublevels. Laser sources with wavelengths near 280 nm are required to address the D1 and D2 transitions [63], while an additional source at 285 nm is used for the photo-ionization of neutral magnesium atoms [56, 62, 64, 65].

To address these states, we utilize the $S_{1/2}, F = 3, m_F = +3$ to $P_{3/2}, F = 4, m_F = +4$ cyclic transition for Doppler cooling and the $S_{1/2}$ to $P_{1/2}$ transition for repumping to achieve high-fidelity state preparation. The non-degenerate $F = 2$ and $F = 3$ states serve as a two-level system, which we manipulate via two-photon processes using far-detuned Raman beams (detuned by approximately 20 GHz from the $S_{1/2}$ to $P_{3/2}$ transition) or through magnetic dipole-allowed transitions using a microwave field. To generate laser wavelengths near 280 nm, we use infrared (IR) lasers, as there are no direct laser sources available at these wavelengths. We rely on commercial fiber lasers [66] and/or home-built vertical external cavity surface emitting lasers (VECSELs) [65, 67–69] operating near 1120 nm, with two frequency-doubling stages to reach target UV wavelengths, as shown in Fig. 7. For photo-ionization purposes, we use VECSELs operating near 1140 nm or dye lasers operating near 570 nm. For more details on the implementation of such laser systems, please refer to the work of Kiefer et al. [65].

In this setup, an IR laser beam (approximately 1.7 W) passes through an optical isolator and enters a bowtie-type doubling cavity, formed by four mirrors (M1-M4) with a lithium triborate (LBO) crystal positioned between mirrors M3 and M4. The matching of modes is achieved by adjusting the crystal temperature, typically maintained at around 90 ° C, with a stability of 10 mK. A piezo-mounted mirror (M2) enables active feedback stabilization of the cavity using

an analog proportional-integral-derivative (PID) control loop and the Hänsch-Couillaud locking technique [70], with reference signals collected by a differential photodiode. The 560 nm light ($2\omega_{\text{laser}}$) produced by the LBO cavity, typically 500–600 mW, is directed into a second bowtie cavity containing a beta barium borate (BBO) crystal between mirrors M3 and M4. Approximately 10% of the $2\omega_{\text{laser}}$ light is diverted for absolute reference, using iodine-based saturation absorption spectroscopy or a wavelength meter[9]. Unlike the LBO crystal, mode matching for the BBO crystal is achieved by adjusting the angle, with mirrors M3 and M4 placed off-center to compensate for the walk-off angle. The BBO cavity is flooded with oxygen and the crystal is kept at 40–$50\,^{\circ}$C to prevent condensation. The final UV output at $4\omega_{\text{laser}}$, with a power range of approximately 30–50 mW, is directed to acousto-optic modulator (AOM) setups, as shown in Fig. 8, for further frequency fine-tuning as required. For photo-ionization, we use an in-house developed VECSEL laser operating at 1140 nm, directed to the chamber after two frequency doublers to address the $S_0 - P_1$ transition. Our in-house developments in VECSEL laser systems [65] and monolithic SHG setups [69] have significantly reduced the complexity and instability of previous systems while addressing the scarcity of laser sources. This configuration provides a stable and precise laser system for addressing transitions in Mg ions across various experimental tasks.

Reference (Wavemeter or I_2)	Transition	Beams	$\Delta/2\pi$(MHz) (w.r.t Reference)	No. of AOM's (passes)
1072.085 340 THz (UV)	$S_{1/2} - P_{3/2}$	BDx	+450	1 - Double pass (2x)
		BD	+430	1 (2x)
		BDD	+120	1 (1x)
		Raman B_1,B_3	20,000 + 1100	3 (5x)
		Raman R_1,R_2	20,000 - 440	1(2x)
1069.339 644 THz (UV)	$S_{1/2} - P_{1/2}$	RD	+800	2 (2x)
		RP	-800	2 (2x)

Table 1: Current laser beams and their reference frequencies, along with AOM detunings for B=10.95 mT. Raman B and R beams have a relative detuning $\delta_{\text{B-R}}/2\pi \approx 1541.067$ MHz, achieved with 4 AOMs (operating configuration: 1-single pass and 3-double pass) operating near $\omega_{\text{DDS}}/2\pi \approx 220$ MHz. In case of repumper beams (RP and RD), have a relative detuning $\delta_{\text{RD-RP}}/2\pi \approx 1600$ MHz, operating near $2\pi \times 200$ MHz.

Figures 8 and 9 provide detailed top views of two optical tables, showing the functional sections and labeling all the acousto-optic modulator (AOM) setups used for frequency tuning. These setups are essential for tasks such as Doppler cooling and detection [65], where 2-3 AOMs are used. For the repumper beams, we employ two beams with relative detuning $\delta_{\text{RD-RP}}/2\pi \approx 1600$ MHz through four double-pass AOMs to address the ground state manifolds $F = 2$ and $F = 3$, facilitating efficient state preparation. Additionally, the Raman beam setup employs up to four AOMs to address two levels via a two-photon process, with a relative detuning $\delta_{\text{B-R}}/2\pi \approx 1541$ MHz to match the qubit transition frequency ω_{qubit} (MW0). Table 1 lists all detunings with respect to the D1 and D2 transitions [63].

[9] High Finesse WS-U

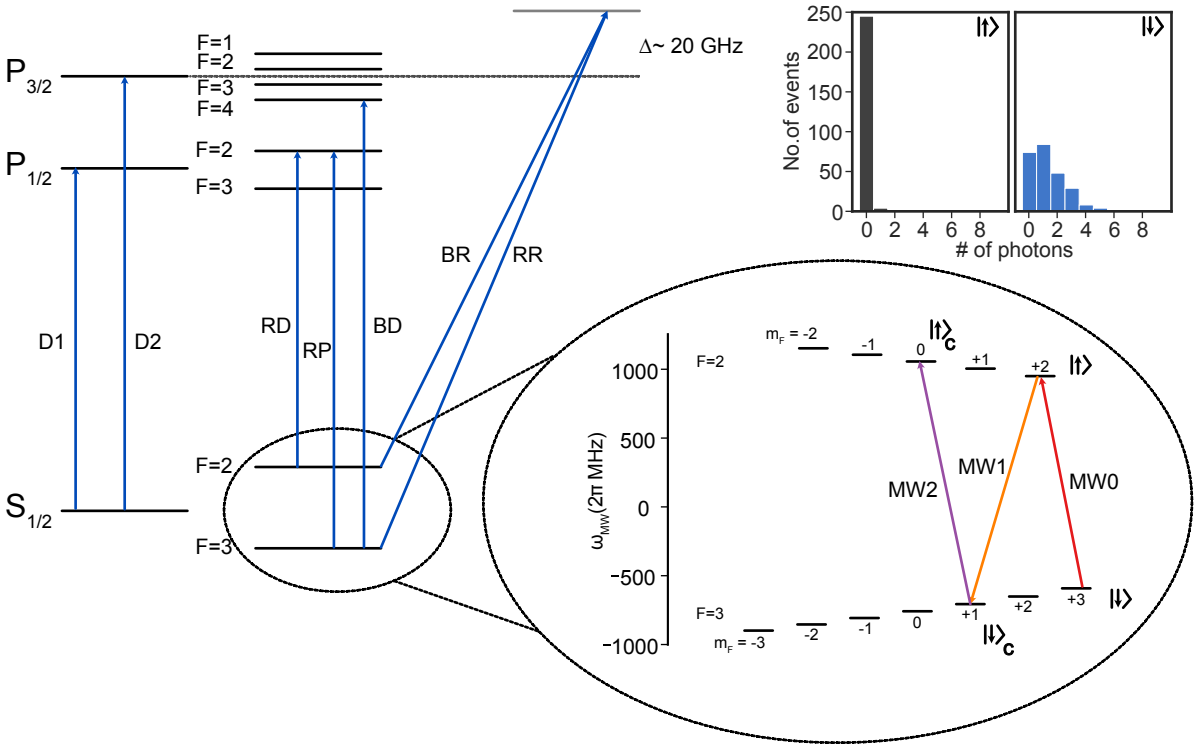

Figure 6: Energy level scheme of $^{25}Mg^{+}$. The D_1 and D_2 transitions are illustrated based on [63, 71]. For Doppler cooling, we use the cyclic $S_{1/2}$ $F = 3, m_F = +3$ to $P_{3/2}$ $F = 4, m_F = +4$ transition, with a linewidth of $\Gamma/2\pi \approx 41.8$ MHz. Three BD beams are introduced: one far-detuned by 8Γ, one detuned by $1/2\Gamma$, and one on-resonant; two are used for cooling, and one is used for detection. For repumping, we employ two beams from the D_1 laser (RD and RP), with relative detuning $\delta_{\text{RD-RP}}/2\pi \approx 1600$ MHz, to address the F=3 and F=2 levels for effective state preparation. Sub-Doppler cooling is achieved with two far-detuned beams (Raman R, and B), $\Delta/2\pi \approx 20$ GHz with respect to cyclic transition, and having a relative detuning, matching the qubit frequency $\delta_{\text{B-R}}/2\pi \approx 1541$ MHz(MW0). These beams target two levels with an appropriate k-vector to efficiently address the motional degree of freedom, enabling resolved sideband cooling and spin-motion coupling. In the zoomed section, non-degenerate states of the hyperfine manifold are shown under $\vec{B} \approx 10.95$ mT, with magnetic dipole-allowed transitions marked as MW0, MW1, and MW2. The top plot shows a histogram differentiating $|\downarrow\rangle$, represented as bright with $\bar{N}_{|\downarrow\rangle} \approx 2$, from dark $|\uparrow\rangle$ states, with $\bar{N}_{|\uparrow\rangle} \approx 0.2$.

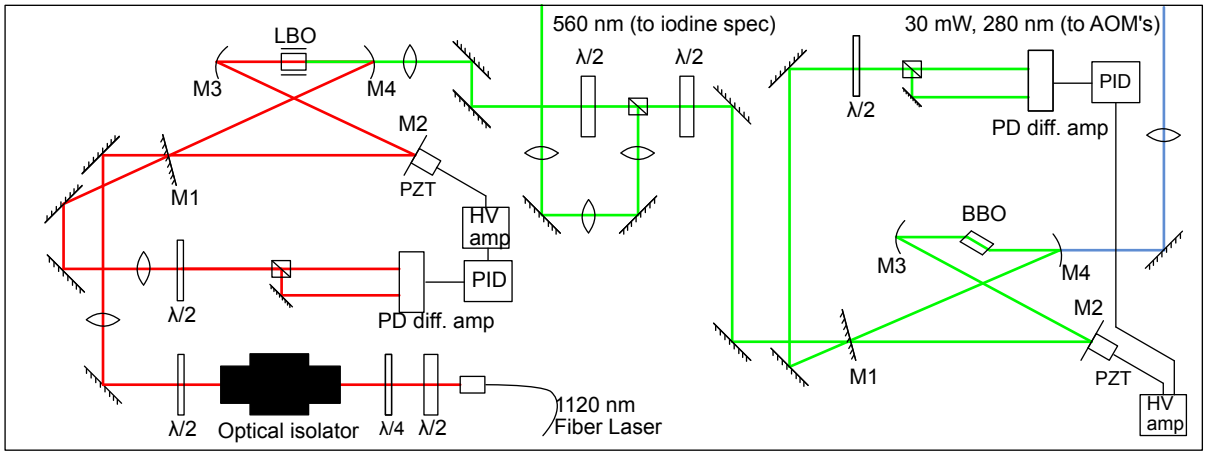

Figure 7: Second-harmonic generation (SHG) setup. This typical setup (not to scale) generates $4\omega_{\text{laser}}$ light at 280 nm from an infrared (IR) source operating at 1120 nm, seeded by a fiber laser. The system includes two bow-tie type optical cavities with four mirrors each: a lithium triborate (LBO) cavity on the left and a beta barium borate (BBO) cavity on the right. Multiple lens systems are used to achieve appropriate beam parameters for maximal conversion efficiencies. Mode matching for the LBO cavity is achieved by adjusting the crystal temperature, while for the BBO cavity, it is achieved by angular alignment. Both cavities feature M2 mirrors mounted on piezoelectric actuators, with active feedback provided by an analog PID control system using the Hänsch-Couillaud locking technique. After the LBO cavity, a portion of the output is directed to a Doppler-free saturation absorption spectroscopy setup with iodine molecules (I_2) for absolute referencing and to a wavelength meter for monitoring and active locking. The UV beam exiting the BBO cavity is directed towards acousto-optic modulator (AOM) setups for further frequency tuning, tailored for specific experimental requirements.

After frequency tuning, the laser beams are directed to a separate optical table, where they are aligned to interact with the trapped ions through specific windows in the chamber. The Doppler and repumper beams are combined, σ^+-polarized, and enter via a glan laser (GL) polarizer aligned along the quantization axis $\vec{B}$. Four Raman beams (B_1+R_1, R_2, and B_3) enter through three distinct windows: R_2 is $\sigma \pm$ polarized, while B_1 and B_3 are π polarized. The photo-ionization laser (indicated in yellow for the sake of clarity) overlaps the Raman R_2 beam. An ablation-based loading mechanism is provided by a pulsed laser[10] positioned near the chamber window, which directs light onto the magnesium wire (shown in Fig. 4). All laser beams are focused at an approximate waist in the range of 10–30 μm unless otherwise specified. Each AOM is driven by either standalone direct digital synthesizer (DDS) boxes or DDS channels managed by the experimental control system.

[10]Integrated Optics: Matchbox Laser

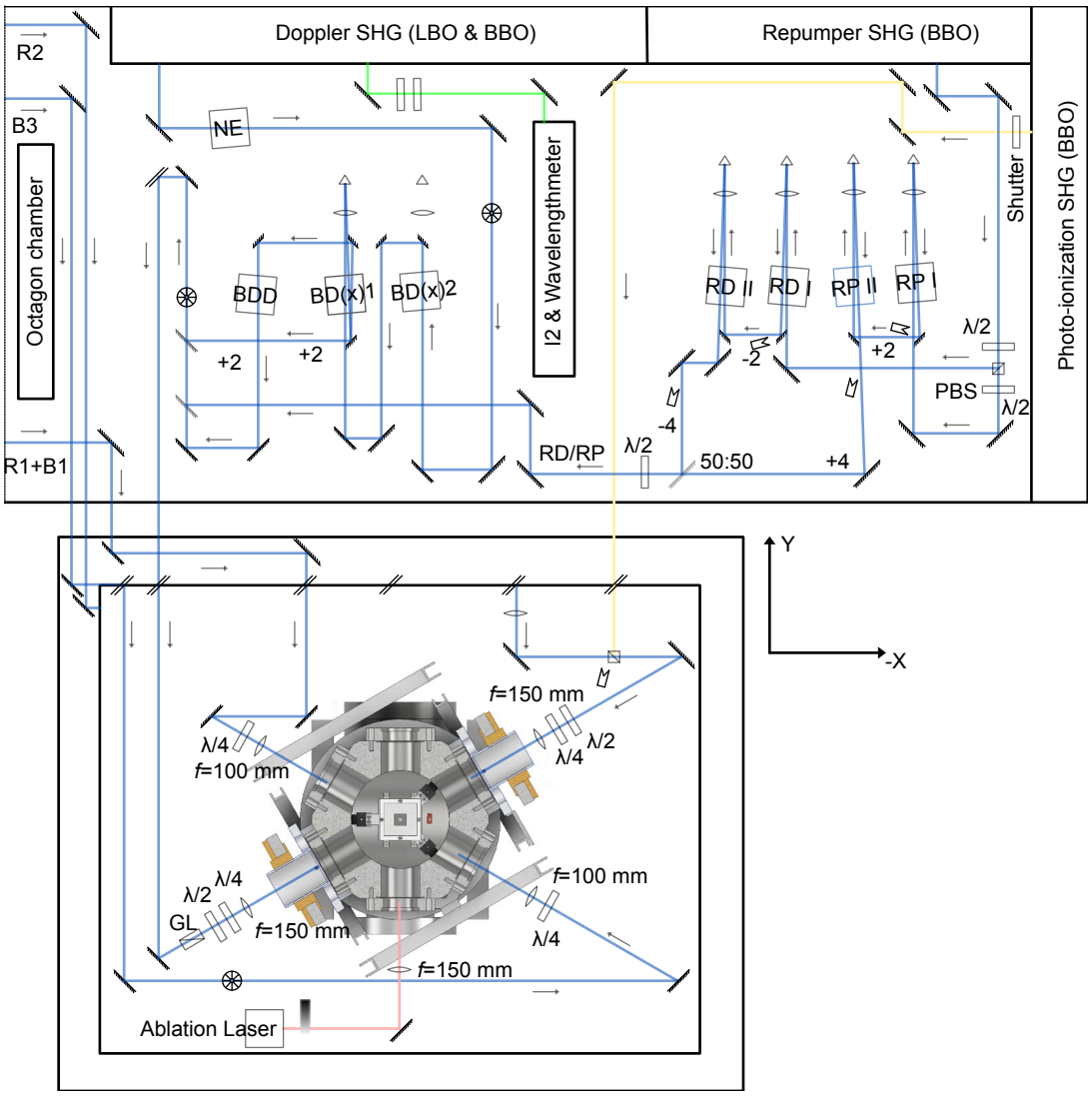

Figure 8: Doppler, photo-Ionization, and repumper beams. A schematic of two optical tables (not to scale), with one table hosting SHG setups similar to Fig. 7 for each laser system. For Doppler beams, three AOMs produce the far-detuned Doppler beam (BDD), the $\Gamma/2$-detuned BD, and the on-resonant BDx beams. BD(x)2 generates an additional set of Doppler beams for localized addressing with focused beams. All Doppler beams are combined using 50:50 beam splitter, pass through a beam-cleaning pinhole, and are directed to the UHV chamber. The beams are aligned with the quantization axis $\vec{B}$ and enter the chamber via a GL polarizer. For repumping, two beams of equal power with relative detuning $\delta_{\text{RD-RP}}/2\pi \approx 1600\,\text{MHz}$ using four double-pass AOMs, combined with the Doppler beams, and reach the UHV chamber at approximately $1\,\mu\text{W}$ (approximately 50% of the saturation intensity). The photo-ionization beam exits the SHG box, is controlled by a shutter, and is combined with the Raman R2 beam before entering the chamber. A pulsed ablation laser, positioned close to the chamber, is focused with an $f = 150$ mm lens onto the magnesium wire shown in Fig. 4. The second half of the setup hosts laser systems that produce far-detuned beams used as Raman beams, as shown in Fig. 9.

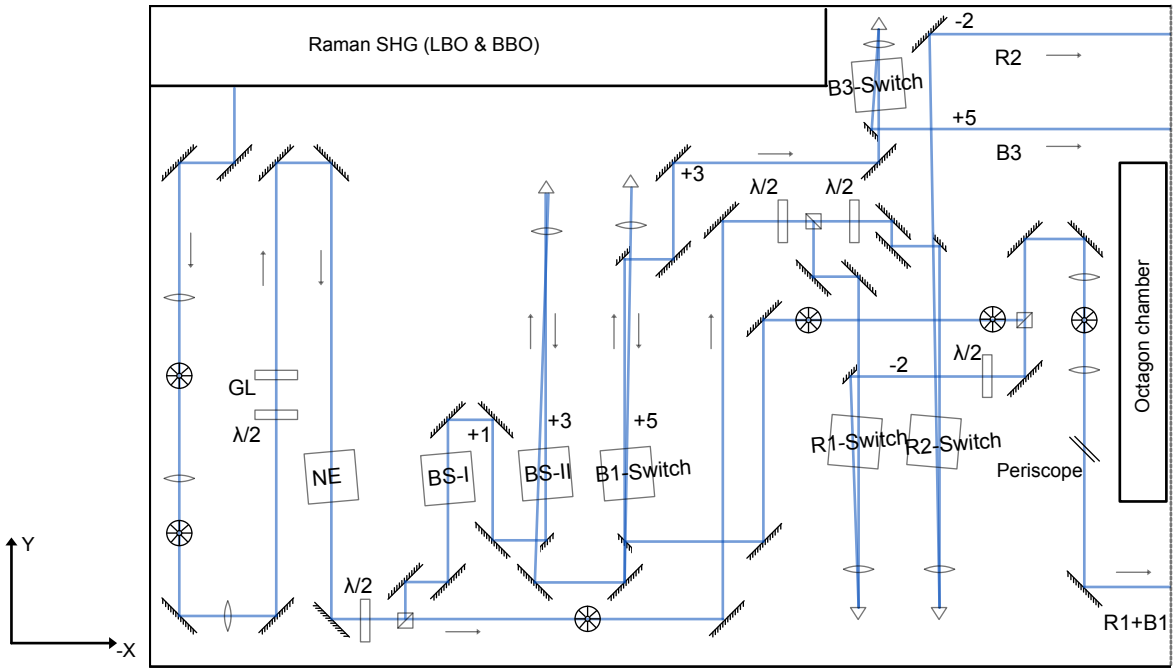

Figure 9: Raman laser systems. This setup represents one-third of the entire system, with the remainder shown in Fig. 8. A UV beam emitted from the SHG cavity is reshaped and optionally noise-reduced via a dedicated AOM. The system is divided into two primary branches: Raman B and Raman R. For the Raman B branch: after passing through a single-pass and a double-pass AOM shifter, the beam is directed through the B_1 or B_3 switch AOM to achieve the desired beam configuration, resulting in a net shift of $+5\omega_{\mathrm{DDS}}$. For the R branch, two AOMs, labeled R_1 and R_2, are used to achieve the appropriate Raman beam configuration, yielding a total shift of $-2\omega_{\mathrm{DDS}}$ orders. By combining both branches, we achieve a relative detuning of $\delta_{\mathrm{B\text{-}R}}/2\pi \approx 1541\,\mathrm{MHz}$, which addresses the chosen qubit transition via a two-photon process. The beams B_1 and R_1 are overlapped on a polarizing beam splitter (PBS) and enter through a single window, while R_2 and B_3 follow separate paths and enter through different windows to meet specific experimental requirements, such as spin-motion coupling (see Sec. 3.1.2).

2.2.2 DC - GHz Control

In this subsection, we describe the control instrumentation, organized into three functional sections: 1) RF, 2) a stack of AWGs for generating signals ranging from DC up to MHz frequencies, and 3) MW circuitry for addressing hyperfine splitting in the 2 GHz range. We provide a brief overview of the working principles of these functional sections.

RF Setup for Ion confinement and Manipulation

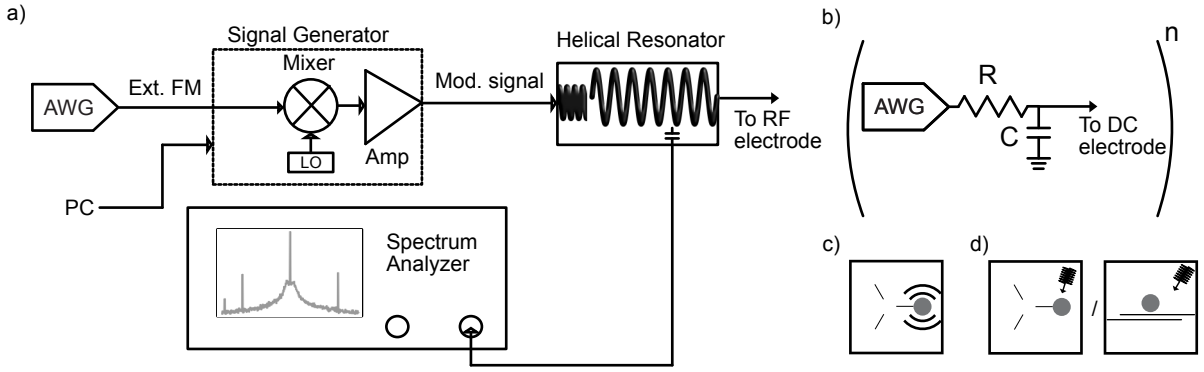

Figure 10: Integral components for controlling oscillating and static components of the potential. (a) **RF Electrode:** Driven by a standalone signal generator connected to the helical resonator, which drives the RF electrode. The frequency or amplitude can be optionally modulated with a single AWG channel to manipulate the motional degree of freedom of a trapped ion. (b) **Control Electrodes:** Individual channels of the AWG are connected to the embedded control electrodes and the mask via a single-stage RC low-pass filter, providing a stable static potential for manipulating motional parameters. Using the in-built DDS and DAC functions of the AWG, we can locally modulate and coherently manipulate the motional degrees of freedom in real time, employing single or multiple electrodes as needed. (c) A schematic diagram of the triangular array illustrates the modulation of potential either via the RF electrode through external modulation or via a local electrode at frequencies comparable to trap frequencies. (d) Two trap architectures are shown: the triangular array and the linear trap, each with a sinusoidal signal directed towards the ion to indicate on-resonant coherent excitation at trap frequencies. These schematics will be referenced in later sections to indicate these specific experimental sequences.

Our surface electrode traps are operated using a single source signal generator[11] with the low phase noise option enabled, achieving noise levels well below -100 dBc. In a standalone configuration, we drive the trap via a helical resonator (shown in Fig. 3) at up to 30 dBm near the drive frequency $\Omega_{\mathrm{RF}}/2\pi \approx 60$ MHz (see Fig. 10), with options for modulation of frequency and amplitude via an external port. The signal generator accepts commands from computing devices over a network connection, allowing tuning of the RF amplitude, frequency, and various parameters via serial commands executed by a computing device. A capacitor near the

[11] Rohde & Schwarz SMA100B

secondary coil of the helical resonator enables us to monitor the RF resonance and adjacent noise features using a spectrum analyzer, facilitating quality estimation and noise characterization. Our surface electrode traps are operated using a single-source signal generator[12] with the low phase noise option enabled, achieving noise levels well below -100 dBc. The primary role of this RF setup is to provide oscillating potentials to the RF electrode, generating a pseudopotential landscape (see Fig. 15) for ion confinement. In the triangular array, this landscape provides confinement in all three directions, while in the linear trap, confinement is achieved in two directions. The trap is driven via a helical resonator (Fig. 3) at up to 30 dBm near the drive frequency $\Omega_{\mathrm{RF}}/2\pi \approx 60$ MHz (Fig. 10). This setup also enables modulation of the RF electrode near the motional mode frequencies, allowing coherent manipulation of the motional degrees of freedom. The signal generator accepts commands from computing devices over an ethernet connection, enabling precise control of various parameters such as RF amplitude, frequency, and modulation details. A capacitor near the secondary coil of the helical resonator provides real-time monitoring of the RF resonance and noise features using a spectrum analyzer, ensuring high-quality operation and noise characterization.

AWG Setup for Control Electrodes

The arbitrary waveform generator (AWG) setup provides static potentials to the control electrodes, enabling precise control of the electric fields and curvatures for ion trapping and manipulation. In the linear trap, this setup controls all three fields and five curvatures, while in the triangular array, the system controls 24 degrees of freedom (8x3) through 30 control electrodes. These electrodes are connected to 30 out of 36 available AWG channels, with some channels also used for coherent excitation of the motional modes. The AWG stack[13] comprises 36 channels, each capable of generating stable voltages with a resolution of 0.3 mV, within the range of $\pm\,10\,\mathrm{V}$. Additionally, each channel features a DDS functionality, enabling the generation of oscillating potentials at frequencies up to $\omega_{\mathrm{DDS}}/2\pi \leq 20\,\mathrm{MHz}$, with a system clock operating at $\omega_{\mathrm{clock}}/2\pi \approx 50\,\mathrm{MHz}$. The channels are distributed across 12 boards, organized into 4 groups, where one board in each group serves as the master, interfacing with a computer for programming. Each AWG channel is connected to the control electrodes through first-order low-pass filtering components located at the vacuum feedthroughs[14], as shown in Tab. 10. These filters ensure stability by attenuating high-frequency noise while allowing smooth interpolation during waveform playback. Furthermore, an internal mixer circuit enables real-time modulation of the RF electrode via an external modulation port (Fig. 10, panel a). This setup provides a dynamic and precise control framework for both static and oscillating potentials, facilitating coherent manipulation of motional degrees of freedom and supporting advanced experimental

[12] Rohde & Schwarz SMA100B
[13] PDQ - Pretty Darn Quick boards developed at NIST
[14] D-SUB 25

sequences such as ion transport (see Sec. 3.2.4).

Microwave Setup For Qubit Manipulation

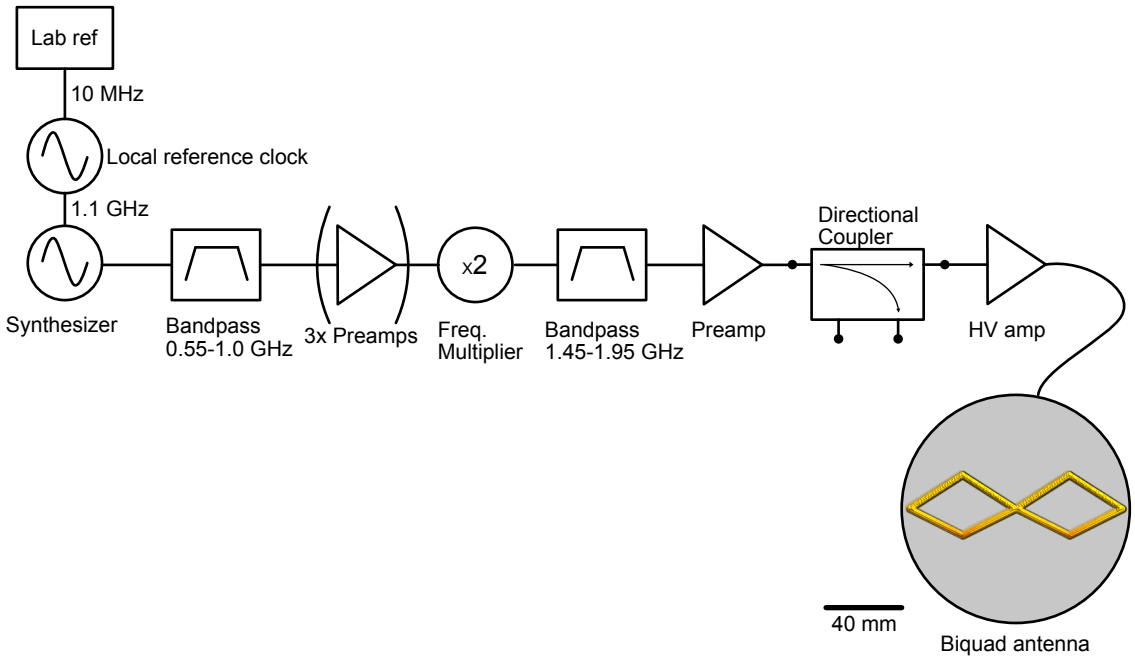

Figure 11: Microwave source for qubit manipulation. The microwave (MW) setup drives magnetic dipole-allowed transitions in the ground-state hyperfine manifold of the $^{25}Mg^{+}$ ion, targeting transitions in the range of $\omega_{MW}/2\pi \approx 1.5$–$1.9\,\text{GHz}$. A synthesizer with a DDS generates frequencies in the range of 0–$0.55\,\text{GHz}$, with a local oscillator clock operating at $\omega_{clock}/2\pi \approx 1.1\,\text{GHz}$ providing the reference input. The mirror signal, $(\omega_{clock} - \omega_{DDS})$, is filtered through a bandpass filter, isolating carrier frequencies in the range of 0.55–$1.0\,\text{GHz}$. Amplifiers and attenuators condition the signal for a frequency doubler, producing the target frequency range of 1.5–$1.9\,\text{GHz}$. Another bandpass filter isolates the desired MW signal, which is then further amplified. The final MW signal is monitored for back reflections using a directional coupler and transmitted via a homebuilt Biquad antenna, positioned approximately $10\,\text{cm}$ outside the UHV chamber and optimized for efficient signal transmission at $\omega_{MW}/2\pi$.

The microwave (MW) setup is designed to drive the magnetic dipole-allowed transitions in the ground-state hyperfine manifold (see Fig. 6) of the $^{25}Mg^{+}$ ion, targeting transitions in the range of $\omega_{MW}/2\pi \approx 1.5$–$1.9\,\text{GHz}$. A synthesizer with a direct digital synthesizer (DDS)[15] generates frequencies $\omega_{DDS}/2\pi$ in the range of 0–$0.55\,\text{GHz}$. The DDS clock is provided by a local oscillator[16] operating at $\omega_{clock}/2\pi \approx 1.1\,\text{GHz}$, which produces a mirror signal in the range of $(\omega_{clock} - \omega_{DDS})\,\text{GHz}$. This signal is filtered through a bandpass filter[17], isolating the carrier

[15] AD9744 DDS
[16] AXTAL AXPLO2600-FT-10-1100 Rev.1
[17] Minicircuits VBFZ-925-S+

frequency in the range of 0.55–$1.0\,\mathrm{GHz}$. The filtered signal is amplified using preamplifiers[18] and attenuators[19], as needed, to achieve the required input power for a frequency doubler[20]. The frequency doubler outputs microwave signal $\omega_{\mathrm{MW}}/2\pi$ in the range of 1.5–$1.9\,\mathrm{GHz}$, targeting the hyperfine transitions. An additional bandpass filter[21] further isolates the desired signal and suppresses spurious components. The filtered signal is subsequently amplified using a preamp[22] and a high-power amplifier[23]. To monitor back reflections, a directional coupler[24] is used, ensuring stable transmission. Finally, the amplified signal is transmitted through a home-built Biquad antenna, designed to maximize efficiency at $\omega_{\mathrm{MW}}/2\pi$. The antenna is positioned approximately $10\,\mathrm{cm}$ from the trapped ions, outside the UHV chamber.

[18] ZX60-8008E-S+
[19] Minicircuits VAT-4+
[20] ZX90-2-11-S+
[21] Minicircuits VBFZ-1690-S+
[22] ZX60-4016E+
[23] ZHL-30W-252-S+
[24] OmniSpectra 20063-20

2.3 Control interface & Data Acquisition

With the essential hardware and control fields implemented, an efficient interface is required to synchronize various components of the experimental setup. This interface facilitates high-temporal resolution in experiments, enabling precise control and streamlined data acquisition, analysis, and data storage. Figure 12 provides a schematic overview of the entire setup, illustrating the integration of hardware and software components necessary for stable and scalable experimental control.

The control hardware encompasses essential input and output modules for manipulating both the electronic and motional degrees of freedom in the trapped ions. Input components, such as the AWG, RF sources, B-field coil driver, microwave sources, and laser systems, establish the necessary control fields. Outputs are primarily acquired through EMCCD imaging and PMT photon-counting systems. To achieve the required high temporal resolution, the system is based on FPGA-based control devices, such as the pulse sequencer [25], AWG, DDS, and data-acquisiton system (DAQ) [26]. These FPGAs provide application-specific functional modules designed to meet the high-precision demands of quantum experiments, such as sub-nanosecond timing and simplified troubleshooting. Control and acquisition systems are interfaced with computing platforms via various protocols [27], allowing synchronized operation across all components.

The core of the interface is the experiment input and output system (EIOS), integrated with a graphical user interface (GUI) using the Experiment-PC. The EIOS manages and controls all experimental parameters, configuring the AWG, DDS channels, and pulse sequencer to execute tasks such as Doppler cooling, state initialization, and coherent state manipulation. The GUI enables real-time monitoring, efficient troubleshooting, and direct access to raw data. During each experiment, photon counts, as the primary output, are processed by the PMT and recorded via TTL counters. The Pulse Sequencer and DAQ systems coordinate the experimental sequences, ensuring precise control of fields and synchronized data collection with nanosecond-level temporal accuracy. After each experiment, the EIOS compiles all relevant data, including configured parameters and execution scripts, into a single result file, facilitating streamlined retrieval and analysis.

To enhance stability and laboratory efficiency, we employ various micro-services for real-time monitoring and reporting. A time series database, InfluxDB[28], stores long-term data to evaluate

[25] Paulbox
[26] Meilhaus
[27] TCP/IP, USB, and PCI
[28] InfluxDB OSS

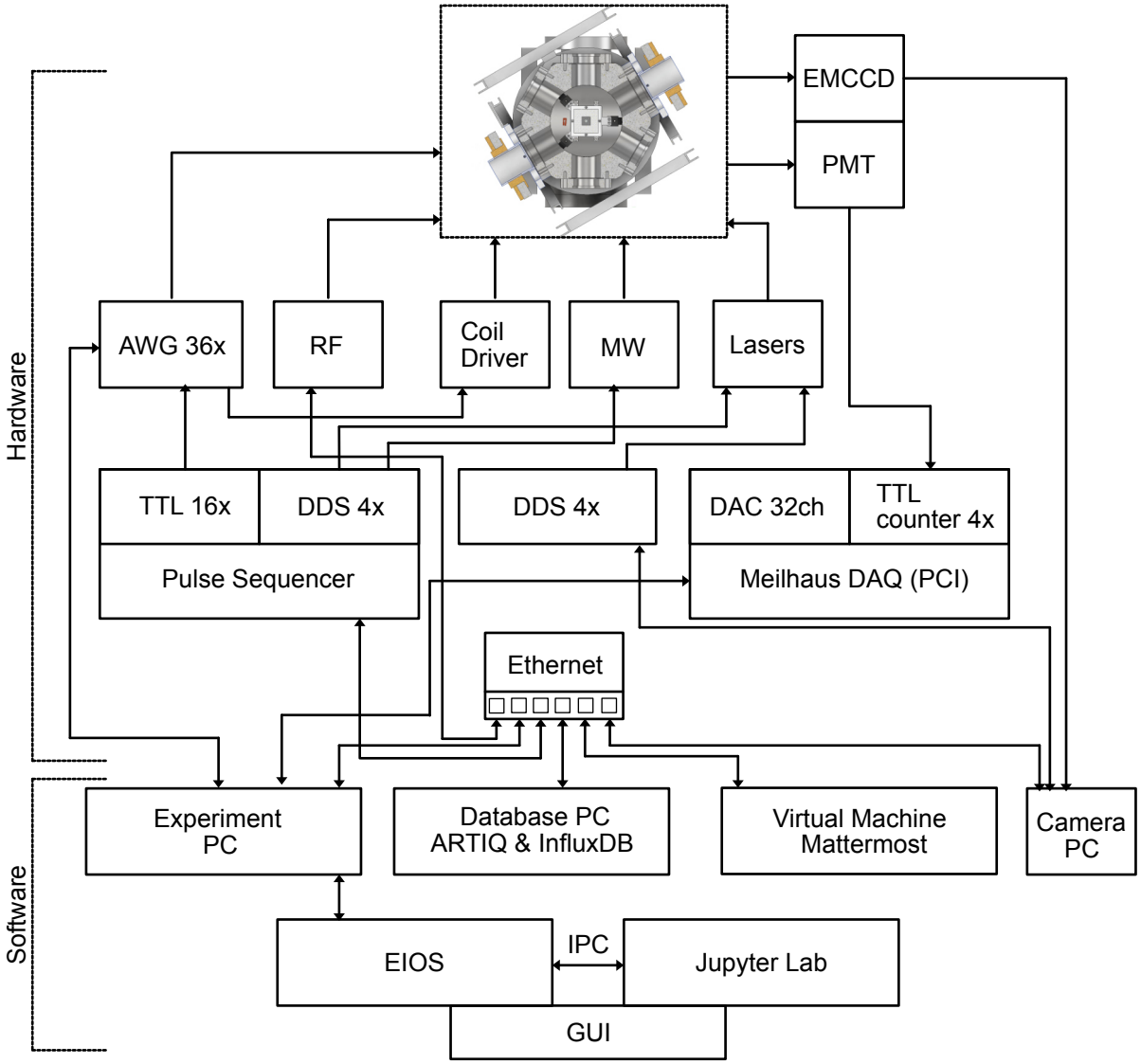

Figure 12: Software and hardware control system architecture. A schematic representation of the integrated hardware and software control systems used in the experiment. The hardware components (top section) include key devices such as the EMCCD camera, PMT, and various control modules (AWG, RF sources, coil drivers, MW sources, and lasers) to manage ion trapping, manipulation, and detection. Pulse sequencing is managed through TTL and DDS channels, while signal acquisition and processing are handled by DAC and TTL counters connected to the data acquisition System (DAQ). The software components (bottom section) are networked through a central Database PC running advanced real-time infrastructure for quantum physics (ARTIQ) and a database (InfluxDB), which communicates with other PCs, including the Experiment PC, Virtual Machine (for Mattermost), and Camera PC. The system enables precise monitoring and real-time adjustments through interfaces such as Jupyter Lab, GUI, and EIOS, which facilitate data analysis and experimental control.

component stability and performance trends, while semi-automated services provide regular reports and alerts for troubleshooting and maintenance. This setup also includes a multi-user platform, Mattermost, to receive automated notifications for any deviation in performance or component failure, allowing preemptive interventions. InfluxDB's flexible schema-less design facilitates seamless integration of new data types for historical tracking, offering efficient data retrieval and minimal programming effort. By combining InfluxDB with Mattermost, the system enhances the stability and reliability of experiments, reducing maintenance time, and supporting proactive lab management. Looking for scalability, the current pulse sequencer could be replaced with a community-supported open-source system, such as Sinara [29] hardware, integrated via the advanced real-time infrastructure for quantum physics (ARTIQ) environment (see Appendix C). This upgrade would support the scalability requirements of the experimental setup by providing a modular framework for more extended configurations.

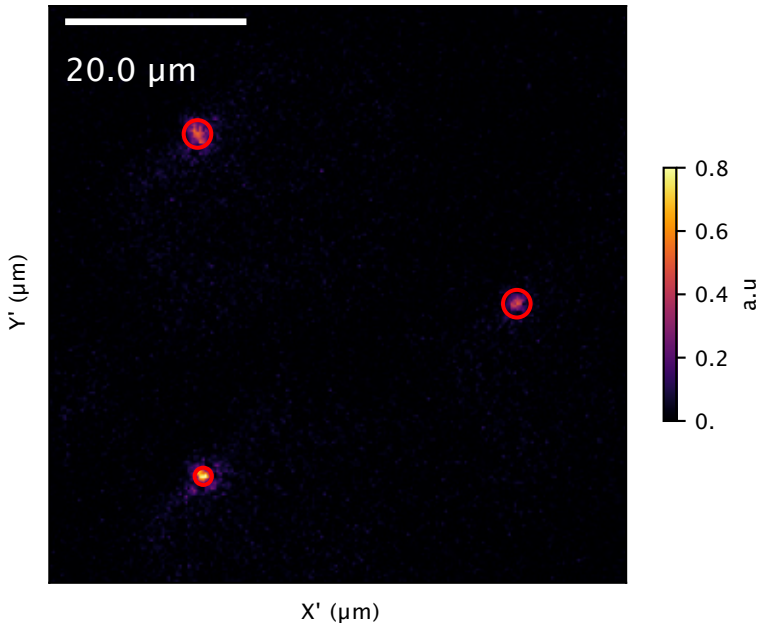

Figure 13: Ion detection and position marking using the OpenCV package. This example image shows a trapped-ion triangular array. We demonstrate the use of the SimpleBlobDetection function in OpenCV to identify and distinguish the trapped ions within the imaging area. The detection algorithm applies a thresholding technique to isolate the ion images from background noise by setting an intensity cutoff, ensuring that only pixels above this threshold are considered. The detected ions are marked at their centroid positions, allowing for precise localization. These positions are then written to the database and saved to result files. Any changes in ion position, such as those caused by stray fields or the presence of other isotopes, can be easily identified with this method.

In our experimental setup, high-resolution EMCCD imaging combined with the SimpleBlobDetection function in OpenCV allows accurate identification of trapped ions and determination of their absolute positions relative to the trap reference [72]. By applying a carefully chosen inten-

[29] community driven control electronics licensed under CERN OHL v1.2

sity threshold, the algorithm isolates the images of the ions from the background noise, marking the centroid position of each ion for precise localization. These positions are recorded in a database and saved in result files, enabling the tracking and analysis of positional shifts due to factors such as stray fields or isotope presence. In addition to SimpleBlobDetection, alternative methods like the Laplacian of Gaussian (LoG) technique can enhance detection by identifying circular features in non-uniform lighting conditions through edge enhancement [73]. For long-term monitoring, we systematically log metadata, including ion positions, intensity profiles, and other ion properties, into a database. This information enables historical tracking, anomaly detection, and consistency between experiments, supporting optimal trapping conditions and experimental reliability over time.

As quantum experiments grow in complexity, fast execution of calibration sequences is essential to maintain reproducibility and consistency. Using modern computing systems and application-specific devices like FPGAs, experimental efficiency has improved greatly. An efficient repetition of measurements allows for faster hypothesis verification. This approach mirrors challenges faced by data scientists and software engineers, who need efficient ways to reproduce system states or bugs under specific conditions. In our case, we use Jupyter Lab, combined with essential Python packages, to streamline experiment management and reduce redundant tasks. By interfacing Jupyter Lab with our EIOS via an inter-process communication (IPC) protocol, we can set attributes, manage datasets, schedule experiments, retrieve data from result files, conduct analyses, store results in the database, and set as attributes for upcoming measurements.

Figure 14 shows an example Jupyter cell that executes a typical experiment involving two-photon-stimulated Raman transitions. The cell performs the following actions:

1. **Control Parameters**: Sets the necessary parameters for the experiment, such as beam configuration, precooling requirements, and timing for specific beam combinations.

2. **Script Selection**: Specifies the script to run, scan the variables, the number of data points, the repetition count, the scan range, and the fit model for the analysis.

3. **Log Entry**: Automates logging of each experiment execution in the database, including fit model and results, ensuring reproducible data for future analysis.

4. **Script and Result File**: After the experiment, all relevant information is displayed to verify accuracy.

5. **Plot and Quick Analysis**: Data are displayed with model fit and corresponding results for

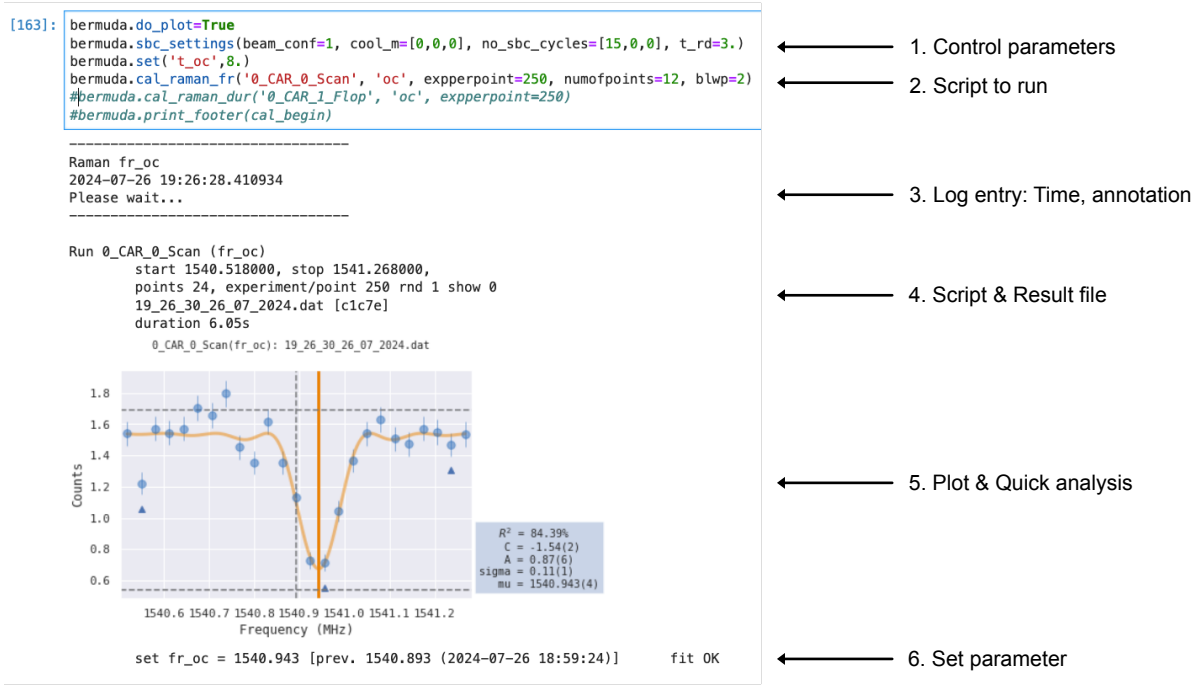

Figure 14: Software interface: Execution of an experiment via Jupyter Lab. The inter-process communication (IPC) connects the C-based experimental control system with Python-based data analysis platforms, such as Jupyter Lab. This interface enables experiment scheduling, quick data analysis, and the creation and manipulation of datasets that can be used by other related experiments. An example Jupyter cell demonstrates the following steps: 1) Control parameters are set using pre-written functions; 2) the experimental script is selected; 3) upon execution, key entries are logged for post-selection analysis; 4) after execution, the result filename is recorded in the log; 5) data is broadcasted via IPC and plotted using the Matplotlib package, along with fit functions to extract relevant information, such as resonance frequencies; and 6) extracted information is saved or appended to the result file, with selected observables written to the database for long-term analysis.

immediate review.

6. **Parameter Setting**: The fit result is saved as a dataset accessible to subsequent experiments, allowing for comparisons with previous results and further analysis.

In conclusion, integrating Jupyter Lab with our control system via IPC has improved our approach to experiment control and data analysis, providing the rapid feedback essential in complex quantum experiments. This setup enhances reproducibility with structured logging and database storage while simplifying data analysis through real-time visualization and parameter tracking. The ability to quickly adjust control parameters and repeat experiments allows us to fine-tune experimental conditions efficiently, which makes our laboratory better equipped to handle the precision and scalability required in complex experimental sequences.

3 Methods

In this chapter, we present both foundational and advanced techniques essential for experiments with a trapped-ion array, building on the experimental setup and control features described in the previous chapter. The basic section covers the primary methods required for ion storage, initialization, and cooling, including the theoretical principles that underlie trapped-ion confinement (Section 3.1.1) and the tools used to manipulate and detect electronic and motional states (Section 3.1.2). We also address practical limitations resulting from operational infidelities and instabilities in control fields, providing an overview of how these factors impact coherent operations on the electronic and motional states (Section 3.1.3). The advanced section (Section 3.2) expands on these foundational methods, introducing approaches to detect motional populations within a challenging measurement regime (Section 3.2.1), a laser-free approach for intra-site coupling of normal modes at a single trapping site (Section 3.2.2), an automated ion-loading process that enhances initialization efficiency (Section 3.2.3), and a transport technique to move ions between sites within the array, demonstrating a key feature of a prototype QCCD device (Section 3.2.4). In addition, we characterize noise sources, including preparations for in situ cleaning to address motional mode heating caused by surface contaminants, which is critical to maintaining system stability (Section 3.2.5).

3.1 Basic

In the basic section, we present the primary methods necessary to operate a trapped-ion array, covering key concepts of ion storage, initialization, and cooling. We begin with the theoretical principles of trapped-ion confinement (Section 3.1.1), followed by the tools and techniques used to manipulate and detect electronic and motional states within the array (Section 3.1.2). Furthermore, we examine the practical limitations that arise from operational infidelities and instabilities in control fields, highlighting their effects on coherent operations for electronic and motional states (Section 3.1.3).

3.1.1 Ion Storage

As a prerequisite, we need to confine single or multiple ions in a defined position in all directions for a prolonged duration [15, 16]. To confine a charged particle at a position (say r_0) with

potential Φ, we require harmonic confinement in all three directions, with restoring forces acting in case of small displacements $r_0 \pm \epsilon$. The potential Φ in quadratic form is given by Eq. 3.1.

$$\Phi = \frac{1}{2} \sum_i \sum_j r_i H_{ij} r_j, \quad \text{where} \quad i,j \in \{x,y,z\} \tag{3.1}$$

$$H_{ij} = \begin{bmatrix} \frac{\partial^2 \Phi}{\partial x^2} & \frac{\partial^2 \Phi}{\partial x \partial y} & \frac{\partial^2 \Phi}{\partial x \partial z} \\ \frac{\partial^2 \Phi}{\partial y \partial x} & \frac{\partial^2 \Phi}{\partial y^2} & \frac{\partial^2 \Phi}{\partial y \partial z} \\ \frac{\partial^2 \Phi}{\partial z \partial x} & \frac{\partial^2 \Phi}{\partial z \partial y} & \frac{\partial^2 \Phi}{\partial z^2} \end{bmatrix} \tag{3.2}$$

Here, the Hessian matrix H_{ij}, a 3×3 matrix(3.2), describes the second-order derivatives of the potential Φ to provide harmonic confinement. To ensure confinement, we need to fulfill two conditions:

1. The eigenvalues of the matrix must satisfy $\lambda_i > 0$ for $i \in \{x,y,z\}$.

2. The potential must satisfy the Laplace Eq. $\nabla^2 \Phi = 0$, which demands $\sum_{i=1}^{3} \lambda_i = 0$.

Since both conditions cannot be satisfied with only a static potential (as positive eigenvalues cannot sum to zero), due to Earnshaw's theorem, we require a time-varying potential component $\Phi(t)$ to confine ions at position r_0.

Let us assume a total potential Φ that includes an oscillating component $U(x,y,z,t)$ at a frequency Ω_{osc}, acting on a charge Q with mass M, and an optional static component U_{static}. The pseudopotential approximation Φ_{ps} (in eV units) is calculated using Eq. 3.3.

$$\Phi_{\text{ps}} \approx \frac{Q^2}{4M\Omega_{\text{osc}}^2} \left|\nabla U(x,y,z)\right|^2 \tag{3.3}$$

With a charged particle (for example, a magnesium ion) confined in a region with oscillating potentials, we can calculate stability conditions using the Mathieu equations [16]. For a given trapping architecture, the stability condition depends on the oscillating amplitude U, frequency Ω_{osc}, charge-to-mass ratio Q/M, and geometric factor κ. In our case, we used surface-electrode traps with corresponding $\kappa \approx$ 40–100 µm (depending on the ion-to-surface distances). Considering the pseudopotential approximation with provided control parameters for a single ion

in a confined region leads to three uncoupled orthogonal harmonic oscillator modes ω_i for $i \in \{x, y, z\}$. In practice, we can directly measure normal mode frequencies using light-matter interaction tools, which are proportional to the square roots of the eigenvalues $\omega_i^2 \propto \lambda_i$, and $\omega_i \approx \Omega_{\text{osc}}/10$.

In this work, we use two surface-electrode traps: a triangular array [42–45] and a linear trap [48], as shown in Fig. 1, and Fig. 2. In the case of the triangular array, the pseudopotential can be generated purely with an oscillating component at radio frequency (RF). In contrast, in the case of the linear trap, the oscillating component ensures confinement along two directions (λ_1, λ_2), while confinement in the third direction (λ_3) is provided with static potentials U_{static}, similar to a Paul trap [74].

We can write the Hamiltonian H_{trap} for all the (motional) harmonic oscillator modes for a single ion confined in a pseudopotential minimum (site) as given in Eq. 3.4, where $\bar{n}_i$ is the mean motional occupancy in mode i, and the zero-point energy is typically not included.

$$H_{\text{trap}} = \hbar \sum_{i=1}^{3} \omega_i \bar{n}_i \tag{3.4}$$

In case of the triangular array, under application of oscillating potential ($\Omega_{\text{osc}} \approx \Omega_{\text{RF}}$) to the RF electrode, using the setup shown in Fig. 10, at $\Omega_{\text{RF}}/2\pi \approx 52.4\,\text{MHz}$, around 26 dBm, leads to a zero-to-peak voltage $\text{V}_{\text{zp}} \approx 200\,\text{V}$ at the RF electrode. Considering Mg ions, a pseudopotential landscape featuring three distinct trapping sites($\text{T}_0, \text{T}_1, \text{T}_2$) as calculated, forming an equilateral triangle with side length of $40\,\mu\text{m}$ and height of $40\,\mu\text{m}$ from the surface [42–45]. Due to the shape of the RF electrodes, in addition to the designated three triangular sites, we find ten additional trapping sites , spanning from $50\,\mu\text{m}$ to $70\,\mu\text{m}$ above the surface, as shown in Fig. 15.

With 30 segmented control electrodes, we tune electric fields and curvatures at the trapping site $T_i \forall \{0, 1, 2\}$ in all directions. Considering a single trapping site(say T_i, we calculate fields(x,y,z), on- and off-diagonal curvature terms (see Eq. 3.2) along directions such as xx, xy, xz, yz, zz, considering the symmetric condition $H_{ij} = H_{ji} \forall\, i \neq j$, and also to satisfy Earnshaw's theorem. In total, we need eight degrees of freedom to control a single harmonic site, such as three fields and five curvatures. For three sites, we need 24(8x3) constraints, we have sufficient degrees of freedom to reshape the potential landscape, to displace, tune motional mode frequencies(ω_i), and change orientations of the mode vector(u_i). For example, for the application of a single field vector(say E_x (V/mm)), is a linear combination of potentials, applied to appropriate electrodes Φ_{el}, a dimensionless scaling factor $\bar{\text{E}}$, which takes into account

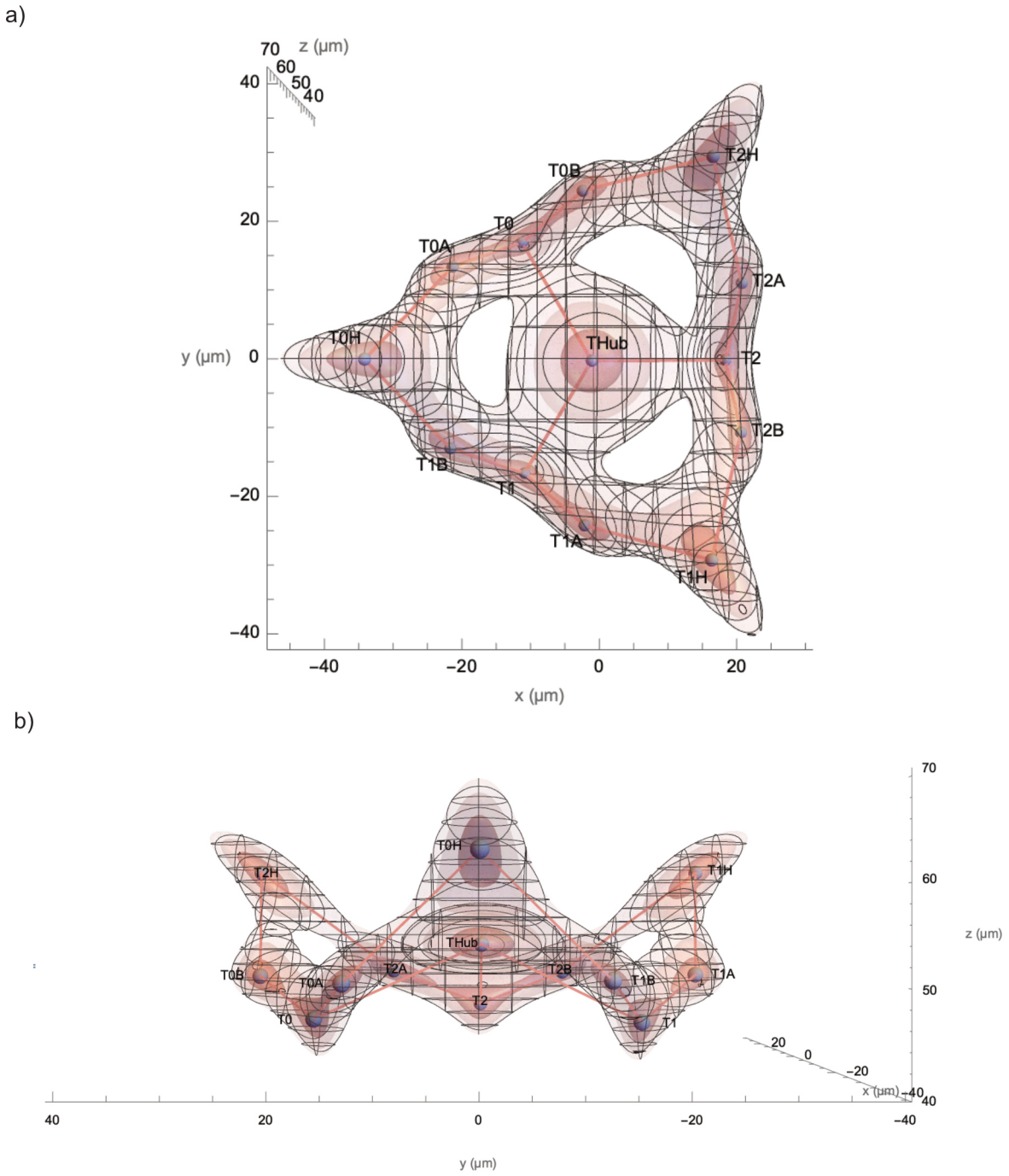

Figure 15: Top and lateral views of the potential landscape of a trapped ion array. The generated pseudo-potential equipotential landscape is calculated for an applied RF voltage of approximately $200\,\mathrm{V_{zp}}$ at $\Omega_{\mathrm{RF}}/2\pi \approx 52.4\,\mathrm{MHz}$, with an $^{25}\mathrm{Mg}^{+}$ ion. In this calculation, the segmented DC electrodes are treated as ground. The shape of the RF electrode creates thirteen RF null positions (blue disks) spanning distances from $40\,\mu\mathrm{m}$ to $70\,\mu\mathrm{m}$ from the surface, surrounded by seven mutually separating regions with multiple or single sites at $0.5\,\mathrm{meV}$ (red), enclosed by a $4\,\mathrm{meV}$ region (black mesh).

the relative distances of all electrodes with respect to the trapping site in Eq. 3.5.

$$E_x = \sum_{el}^{30} \bar{\mathrm{E}}\Phi_{el} \tag{3.5}$$

To realise independent control over three sites, we need to ensure sufficiently low cross-talk control possibilities. Ideally, the requirement is applying field and/or curvature at a particular site, with negligible to no effect on the other sites. In summary, considering all trapping sites, using a constrained convex optimization algorithm [75], all control potential configurations (for three sites) are optimized for individual electrodes, by reducing the squared norm of individually applied voltages. With the superposition rule, potentials for all fields and curvatures can be applied simultaneously to enable a control potential configuration Φ_c. In practice, we find stray fields due to various reasons, a total control potential configuration Φ_c is a combination of oscillating, static, and compensation for stray potentials as given in Eq. 3.6.

$$\Phi_c = \Phi_{\mathrm{RF}} + \sum_{el}^{30} \bar{E}\,\Phi_{el} + \Phi_{stray} \tag{3.6}$$

With optimized control potential configurations, recorded cross-talks were below 5% [42]. Thus, in principle, with three single ions trapped in triangular sites, we extend our Hamiltonian from Eq. 3.4 to Eq. 3.7 that accommodates all three sites and all nine uncoupled harmonic oscillator modes.

$$H_{\mathrm{trap}} = \hbar \sum_{T=0}^{2} \sum_{i=1}^{3} \omega_i \bar{n} \tag{3.7}$$

In case of linear surface electrode trap [76], shown in Fig. 2, where two RF electrode rails, together with 42 electrodes, are embedded in the same plane. With an applied RF potential at $\Omega_{\mathrm{RF}}/2\pi \approx 56\,\mathrm{MHz}$, at approximately $26\,\mathrm{dBm}$, the ion (s) is confined to a minimum common pseudopotential, along two radial directions(u_y, and u_z) at a distance of approximately $80\,\mu\mathrm{m}$ above the trap surface with axial confinement (u_x, parallel to the RF electrode) provided by a static potential with a combination of designated electrodes. Similarly to the triangular array, we use eight degrees of freedom, such as three fields (x, y, z) and five curvatures (xx, xy, xz, yz, zz).

Ion Loading and Doppler Cooling

To produce ions, we have two different procedures: 1. Magnesium oven and 2. Ablation. For the first procedure, we operate the Magnesium oven, installed under the surface-electrode trap, by resistive heating. In case of ablation, we produce hot magnesium atoms by breaking atoms from a Mg wire(shown in Fig. 4). Regardless of the method, we perform isotope-selective ionization, by tuning the frequency of the photo-ionization laser [77]. Photo-ionization of hot magnesium atoms occurs via a two-photon process. With Mg atoms starting with electronic configuration $[\mathrm{Ne}]3\mathrm{S}_2$, we use first-photon excitation from $\approx 285\,\mathrm{nm}$ photo-ionization(PI) laser, leading to $[\mathrm{Ne}]3S_1\,3P_1$, a second photon from Doppler laser(BDD) $\approx 280\,\mathrm{nm}$, or another photon from PI, leads to a single electron transferred into that continuum. By ensuring other control parameters and enabling an appropriate control potential configuration Φ_c, we confine(trap) the resulting single charged Mg atom. Figure 16 shows an experimental sequence, with option for ablation, or oven along with other laser beams involved.

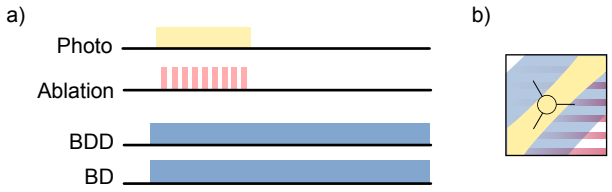

Figure 16: Ion-loading with ablation and cooling lasers . a) shows experimental sequence. We trigger photo-ionization laser in the presence of Doppler beams to assist the photo-ionization process, as well as to laser cool ions with high kinetic energy. In parallel, we trigger the pulsed laser for ablation loading, where a pulse train of a high power laser incident on a Mg wire to produce atoms. In case of the Mg oven/Resistive heating, we prewarm the oven by passing currents in the range of 1-5 A for a couple of minutes to produce an atom vapor. As a result of the photo-ionization via the two-photon process, a singly charged ion gets trapped in one of the RF pseudo-potential minima. b) depicts a cartoon of a triangular array to highlight the presence of photo-ionization beam, in the presence of a pulse train for the ablation process, as well as Doppler beams for the trapping assist. This schematic will be used in later sections to simplify the experimental sequences with a pictorial description.

For prolonged ion storage, we employ Doppler cooling beams to cool ions to the thermal limit $\mathrm{T_D}$. Unlike for neutral atoms [78], it is sufficient to address one dimension, since the restoring force is inherently provided by harmonic confinement if all motional motional modes are addressed. Figure 17a illustrates an experimental sequence with labels (1) and (2) indicating a typical initialization, and the final parts of an experiment. We use the beams in part (1), such as the Doppler beams (BDD and BD) for Doppler cooling to the thermal limit $\mathrm{T_D}$, and the near-resonance beam (BDx) shown in part (2), for fluorescence detection via PMT or EMCCD.

For Doppler cooling [79], we use a cyclic transition between the $F = 3, m_F = +3$ state of

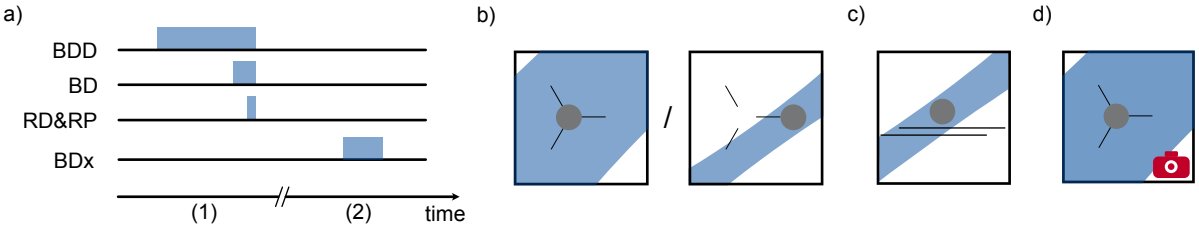

Figure 17: Experimental sequence of initialization and detection, and its cartoon depiction. a) shows experimental sequence including Doppler beams, and repumper beams for initialization, and detection. 1) Usually the first step in every experiment: we expose the ion for prolonged duration detuned Doppler beam (BDD) to cool hot ions. With gamma/2 detuned beam (BD), we reach thermal limit. With repumper beams, we optically pump, to prepare F=3, mF=+3 state with high-fidelity. 2) Typically the last step: For detection, we use near-resonant Doppler beam (BDx), and collect photons with PMT. b) shows two cartoons depicting a broader Doppler beam configuration to enclose all lower-lying sites of the triangular array. Also, we show a focused Doppler beam to address a single site of the triangualr array. c) we represent our linear trap array with this pictogram with two parallel RF electrode. d) shows another detection method using EMCCD camera, mostly during loading procedure.

the $S_{1/2}$ level and the $F = 4, m_F = +4$ state of the $P_{3/2}$ level, at a wavelength of approximately $280\,\text{nm}$ [63] (see Fig. 6). With a natural linewidth of $\Gamma/2\pi \approx 42\,\text{MHz}$, we employ two polarized beams σ^+ with a tunable beam waist ranging from 10 to $100\,\mu\text{m}$. One beam (BDD), far detuned at approximately 8Γ, is used to trap hot ions after ionization, while the other beam (BD), detuned by $\Gamma/2$, is applied for cooling to T_D. Given the saturation intensity of the cyclic transition, $I_\text{sat} \approx 2,550\,\text{W/m}^2$, we can calculate the scattering rate W using Eq. 3.8, where $I/I_\text{sat} = 2\Omega^2_\text{cyclic}/\Gamma^2$ and Δ is the detuning between the transition frequency and the laser frequency [80].

$$W = \frac{\Gamma}{2}\frac{\frac{I}{I_\text{sat}}}{1 + \frac{I}{I_\text{sat}} + \frac{4\Delta^2}{\Gamma^2}} \tag{3.8}$$

With $F_\text{scatt} = \hbar\, k\, W$ as scattering force, after several recoils due to spontaneously emitted photons, the trapped ion reaches thermal equilibrium at T_D.

For light-matter interactions, we define the Lamb-Dicke parameter $\eta = k.x_0$, where k denotes the vector of the interacting field, and x_0 is the width of motional mode's ground-state wave function. It defines the coupling strength between motional and addressed electronic states. Leibfried et al. [16] provides a detailed description of the scattering of trapped ions from the Lamb-Dicke regime, defined by $\eta^2\,\bar{n} \ll 1$. Within the Lamb-Dicke regime, scattering of a photon takes place as carrier transition, as well as motional sidebands. Such scattering can cause recoil induced motional population change. With the experimental parameters, we formulate the cooling (reduction in mean motion occupancy) and the heating rate (increase in mean mo-

tion occupancy) as given in Eq.3.9.

$$A_{\pm} = \eta^2 \left[W(\Delta) + W(\Delta \mp \omega_i) \right] \tag{3.9}$$

Using the rate equation formalism given in Eq. 3.10, we calculate the rate of change of motional population, for our laser beam parameters.

$$\frac{d}{dt}\bar{n} = \sum_{n=1}^{\infty} n \frac{d}{dt} P_n = -(A_- - A_+)\bar{n} + A_+ \tag{3.10}$$

Considering the control potential configuration (without additional curvature control from static fields) hosting three individual ions in three sites of the triangular array and a single ion in the linear trap, we calculate the Lamb-Dicke parameter (η) and the cooling rate ($\bar{R}$). The BD laser beam is detuned by $\Gamma/2$ relative to the $S_{1/2} - P_{3/2}$ transition, with a beam intensity of approximately $0.5\, I_{\text{sat}}$. Under steady-state conditions, the formula for the thermal limit simplifies to $n_{\text{th}} \approx \Gamma/2\omega_i$.

Table 2 lists all the calculated parameters. For relative cooling rates ($\Delta\bar{R}$), all values are normalized with respect to the motional mode ω_1 at the T_0 site. In absolute terms, we estimate 200 quanta/μs for ω_1 with an initial mean thermal population of $\bar{n} \approx 1000$. In practice, Doppler cooling durations ($\approx 50\,\mu$s) are sufficient to cool all addressed modes to their thermal limits. For the lowest-frequency mode in the linear trap, we observe $n_{\text{th}} \approx 16$, corresponding to $\eta^2\bar{n} \approx 1$, which does not satisfy the Lamb-Dicke criterion. For these motional mode, with $\Gamma \gg \omega_i$, the system operates in a weak-binding regime [43]. By engineering $\Gamma \ll \omega_i$ using two-photon stimulated Raman transitions (TPSRT) or electromagnetically induced transparency (EIT), further reductions in n_{th} are achievable [81, 82]. This regime is referred to as the strong-binding regime.

Site	Linear			Triangular array								
				T_0			T_1			T_2		
	ω_1	ω_2	ω_3	ω_1	ω_2	ω_3	ω_1	ω_2	ω_3	ω_1	ω_2	ω_3
$\omega/2\pi$	1.3	4	4.25	4	5	6	4	5	6	4	5	6
η	0.25	0.08	0.01	0.16	0.02	0.01	0.03	0.14	0.01	0.08	0.12	0.01
n_{th}	16	5	5	5	4	3	5	4	3	5	4	3
$\Delta\bar{R}$	0.74	0.25	0.006	1	0.02	0.006	0.04	0.95	0.006	0.25	0.7	0.006

Table 2: Lamb-Dicke parameters (η) and relative cooling rates ($\Delta\bar{R}$) for a single ion in the linear trap and the triangular array. All the motional mode frequencies are in MHz.

Figure 18 illustrates the pseudopotential landscape generated by the applied RF potential, creating a total of 13 trapping sites (blue dots). These sites are divided into seven regions spanning

over a 40–$70\,\mu$m height above the trap surface. The landscape is enclosed by a 4 meV potential barrier (black mesh), with a red-opaque region representing a depth of approximately 0.5 meV to facilitate ion storage. The inset shows a fluorescence image captured with our imaging optics, highlighting the capability to store four ions individually trapped in three fully controllable lower-lying trapping sites and an ancillary site approximately $10\,\mu$m above the triangular array, using the control potential configuration Φ_{pyramid}. We highlight the control features of our platform to facilitate such a configuration to store multiple ions at the thermal equilibrium T_D

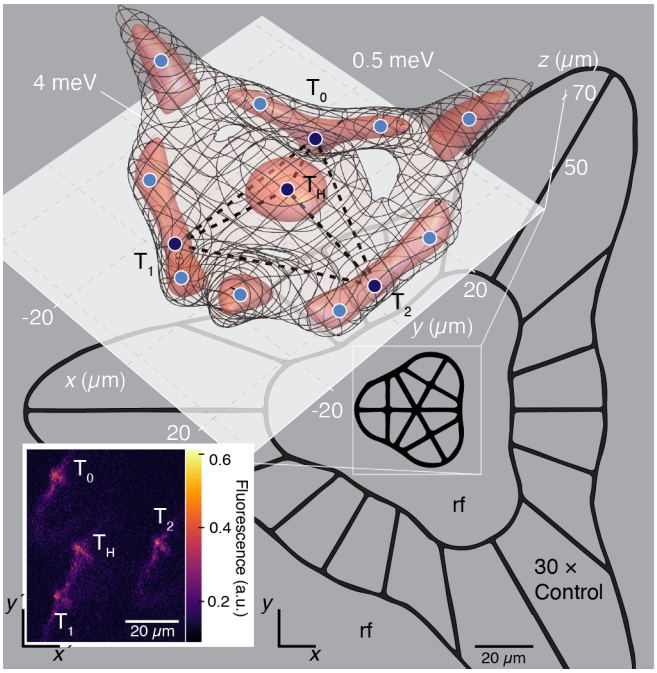

Figure 18: 3D potential landscape of the 40-μm array with fluorescence image of ions stored in all four trapping sites. Adapted from our publication [49]. The RF potential generates a pseudopotential landscape with a total of 13 trapping sites (blue dots), separated into seven regions and spanning a height of 40–$70\,\mu$m above the trap surface. These sites are surrounded by a red-opaque region (0.5 meV potential depth), facilitating ion storage, and enclosed by a 4 meV potential barrier (black mesh). The highlighted trapping sites (dark blue) form a pyramidal configuration, connected by dotted lines, and include three fully controllable lower-lying sites and one ancillary site positioned approximately $10\,\mu$m above the triangular array. The overlaid potential landscape assumes an RF voltage of $V_{RF} \approx 200\,V_{zp}$, validated by experimentally measured mode frequencies at individual sites. The inset fluorescence image, captured using imaging optics with a spatial resolution of $0.32\,\mu$m/pixel, shows four ions individually trapped at the designated sites under the control potential configuration Φ_{pyramid}.

Micro-Motion Minimization/Gradient Minimization

For a single trapped ion at a trapping site, presence of a stray field in an arbitrary direction displaces the ion from the calculated or actual RF pseudopotential minimum. This displacement induces additional ion motion at the RF drive frequency, $\Omega_{\text{RF}}/2\pi \approx 52.4\,$MHz, with amplitude A_{RF} (in dBm units), known as micromotion (MM). To suppress or minimize micromotion,

we tune the electric field E_i, $i \in \{x, y, z\}$ at the given site. In our setup, we report three methods that use an EMCCD camera and fluorescence from the ion collected by a PMT to minimize MM.

1. **In-plane minimization routine**: By controlling the RF drive amplitude as shown in Fig. 10, we track the in-plane displacement of the trapped ion using spatially resolved images captured with the EMCCD camera. Taking into account resolution limitations, we apply in-plane electric fields (E_x and E_y) to compensate for and minimize displacement by changing the RF amplitude. We conclude that this method is effective for in-plane adjustments, though it is limited by the camera resolution.

2. **Out-of-plane minimization routine**: Complementing the previous method, we tuned a curvature term addressing the direction out of the plane, denoted H_{xz}. Residual stray displacement in the out-of-plane direction causes in-plane displacement as a function of $\Delta H_{xz} \approx 1\,\mathrm{V/mm/100\,\mu m}$. By optimizing the global potential in the z-direction with a mask (see Fig. 4), we minimize the displacement due to ΔH_{xz}. Methods 1 and 2 are limited by resolution and by their inability to track residual displacements in the out-of-plane direction.

3. **Fluorescence optimization routine** [83]: By addressing the trapped ion with a laser beam (BDx) near resonance and with significant projection along the motional mode direction, the modulation index due to micro-motion is given by $\beta_{\mathrm{MM}} = |\langle u_i \cdot k_{\mathrm{BDx}} \rangle| A$, where u_i is the motional mode direction. We find that the resulting fluorescence spectrum, as a function of detuning ($\Delta_{\mathrm{MM}} = \omega_{\mathrm{laser}} \pm n\Omega_{\mathrm{RF}}$), is modulated and can be understood in terms of the Bessel functions [56], as given in Eq. 3.11.

$$W_{\mathrm{MM}}(\Delta_{\mathrm{MM}}, \beta_{\mathrm{MM}}) = \sum_{n=-\infty}^{\infty} J_n^2(\beta_{\mathrm{MM}}) W(\Delta_{\mathrm{MM}} - n\Omega_{\mathrm{RF}}) \tag{3.11}$$

   To suppress scattering at the first and/or second micro-motion sidebands, we tune the effective electric fields (αE_x and βE_y). By collecting fluorescence with the PMT, we compare fluorescence changes in the carrier and sidebands. From Tab. 2, we observe that the detection beam breaks the symmetry at most trapping sites, leading to some of the motional modes u_i with low or negligible η, resulting in minimal modulation of the fluorescence spectrum. In such cases, by comparing with Methods 1 and 2, we can significantly minimize micromotion.

3.1.2 Accessing Electronic and Motional States

In the case of $^{25}Mg^{+}$, the presence of nuclear spin ($I = 5/2$) causes a hyperfine splitting of the electronic states, as shown in Fig. 6 [84]. For the ground state manifold, the coupling between the angular momentum of a single electron ($S = 1/2$) and the nuclear spin results in two distinct energy levels, labeled $F = 2$ and $F = 3$. With a quantization field of $\vec{\mathrm{B}} = 10.95\,\mathrm{mT}$, the $F = 2$ and $F = 3$ states become nondegenerate, producing a total of 12 sublevels ($m_F = -F$ to $m_F = +F$) for both $F = 2$ and $F = 3$. We use the Breit-Rabi formalism to calculate eigenstates and relevant properties [85], as the magnitudes of hyperfine and magnetic field couplings are comparable. At $\vec{\mathrm{B}} = 10.95\,\mathrm{mT}$, a magnetic dipole-allowed transition between $F = 3, m_F = +1$ and $F = 2, m_F = 0$ is field-insensitive to first order ($d\omega_{\mathrm{qubit}}/dB \approx 0$), where ω_{qubit} denotes the energy difference between these two levels. In our experiments, we define a pair of hyperfine sublevels of $F = 2$ and $F = 3$ in the ground-state manifold as a two-level system. Throughout this thesis, we employ two specific transitions for experiments.

1. The most field-sensitive transition, between ($F = 3, m_F = +3$) and ($F = 2, m_F = +2$), has a sensitivity of approximately $-2\pi \times 21.76\,\mathrm{MHz/mT}$. We denote this transition by $|\downarrow\rangle$ and $|\uparrow\rangle$, labeling it as MW0.

2. The aforementioned least field-sensitive transition, denoted by $|\downarrow\rangle_c$ and $|\uparrow\rangle_c$, is labeled as MW2.

With these definitions, we express the Hamiltonian for the two-level system (a spin-$\frac{1}{2}$ analog) as given in Eq. 3.12, where $\hat{z}$ denotes the axis with respect to the quantization axis.

$$H_{\mathrm{spin}} = \frac{\hbar}{2}\omega_{\mathrm{qubit}}\hat{\sigma}_z \tag{3.12}$$

The Doppler beams (BD, BDD), aligned with $\vec{\mathrm{B}}$ and σ^+ polarized, assist to optically pump the $^{25}Mg^{+}$ ions into the $F = 3, m_F = +3$ state. However, because of branching ratios in the excited state, there is a residual population in multiple sublevels of the ground-state hyperfine manifold. To reduce this population, we employ two additional beams, RP and RD, which address the D_1 transition. RP and RD address the states $F = 2$ and $F = 3$, respectively, with polarization σ^+, detuned by $\delta_{\mathrm{RD/RP}}/2\pi \approx 1600\,\mathrm{MHz}$. After reaching thermal equilibrium T_D, two or three scattering events due to RD and RP lasers achieve preparation of selected state, say $|\downarrow\rangle$ with highest fidelity. Within the Lamb-Dicke regime ($\eta^2 \ll 1$), spontaneous emission from RP or RD does not alter the motional states.

To implement and control these defined states, we employ two primary tools: (1) a global microwave field (MW) and (2) a local two-photon-stimulated Raman transition (TPSRT).

The MW option functions globally due to its approximately uniform signal strength at all sites ($\lambda_{\text{MW}} \gg d_{\text{inter-site}}$) in the triangular array. With a motional mode frequency ω_i and a Lamb-Dicke parameter of $\eta \approx 0$ for the interacting MW field, there is negligible coupling to the motional states. The MW source frequency, provided by a quadrupler circuit (see Fig. 11), drives a biquad antenna with tunable parameters ω_{MW} and t_{MW}, allowing selective addressing of dipole-allowed magnetic transitions in the ground state manifold. For this spin-$\frac{1}{2}$ analog, the effective magnetic field B_{eff} of the MW signal interacts with the two-level system, described by $H_I = -\mu \cdot B_{\text{eff}}$, where μ is the magnetic dipole moment. The resulting Rabi rate Ω is proportional to B_{eff} [15]. Following time-dependent perturbation theory [86], the oscillating B_{eff} drives a coherent exchange between the two levels when in resonance ($\omega_{\text{MW}} \approx \omega_{\text{qubit}}$).

$$\mathrm{P}_{\downarrow}(t) = \sin^2\left(\frac{\Omega t}{2}\right) \tag{3.13}$$

In the case of using TPSRT (see Fig. 9), our definition as "local" is reasonable since beam waists can be optimized to address individual sites without limitations due to optical elements. Wineland et al. [15] provides a formalism for addressing a two-level system with B_{eff} using two far-detuned ($\approx 1000\Gamma$) beams, detuned such that $\omega_{L1} - \omega_{L2} \approx \omega_{\text{qubit}}$, as given in Eq. 3.14.

$$H_I = \hbar\Omega(\sigma_+ + \sigma_-)\left[e^{i[(\vec{k}_1 - \vec{k}_2)\cdot x - (\omega_{L1} - \omega_{L2})t + \phi]} + \text{h.c.}\right] \tag{3.14}$$

In the interaction picture, assuming that the motional and electronic states are time-independent, the resulting Hamiltonian is given by Eq. 3.15, where $\delta \approx \omega_i\,(n' - n)$, and n' and n are the final and initial motional states, respectively.

$$H_I' = \hbar\Omega\,\sigma_+ \exp\left(i\eta\left(ae^{-i\omega_i t} + a^\dagger e^{i\omega_i t}\right) - \delta t + \phi\right) + \text{h.c.} \tag{3.15}$$

With $\eta < 1$, we find that the interaction leads to coupling between motional and electronic states, and the resulting coherent drive between $|\downarrow, n\rangle$ and $|\uparrow, n'\rangle$ has a Rabi rate that depends on the motional state occupancy, as given in Eq. 3.16.

$$\Omega_{n',n} \equiv \Omega\left|\langle n'|e^{i\eta(a+a^\dagger)}|n\rangle\right| \tag{3.16}$$

With condition $\eta \ll 1$, $\Omega_{n',n}$ is approximately equal to Ω for the carrier ($n' = n$), $\eta n^{1/2}\Omega$ for the

Option	L1	L2	η	Angle
1	B_1	R_1	≈ 0	0° (co-propagating)
2	B_1	R_2	$0.2(1)$	120°
3	B_3	R_2	$0.2(1)$	120°
4	B_3	$-R_1$	$0.2(1)$	180° (anti-parallel)

Table 3: Summary of L1 and L2 configurations, Lamb-Dicke parameter (η), and angles between laser beams.

first red sideband ($n' = n-1$), and $\eta(n+1)^{1/2}\Omega$ for the first blue sideband [15]. By considering option (1), $B_1 \parallel R_1$, with $\eta \approx 0$ due to co-propagating beams, we can coherently manipulate electronic states while remaining insensitive to motional states. For precision metrology of these manifolds and for benchmarking our system, we additionally use Ramsey [87] and spin-echo sequences by separating the fields and controlling its parameters on demand. The combined operation of the MW and TPSRT fields (which are sensitive to motional states), with active synchronization, provides powerful metrology tools for the trapped-ion platform [88, 89].

For spin population analysis, we use log-likelihood analysis (Eq. 3.18) on the collected photons, following Poisson statistics (Eq. 3.17).

$$P(N|\overline{N}) = \frac{\overline{N}^N}{N!} e^{-\overline{N}} \tag{3.17}$$

In practice, we perform the spin population analysis in two steps. First, by assigning bright and dark electronic states, we determine the average number of photons $\bar{N}$ for the defined bright state $\bar{N}_{|\downarrow\rangle}$ and dark state $\bar{N}_{|\uparrow\rangle}$. Second, we analyze any given histogram of collected photons to determine the probability amplitude α.

$$\log \mathcal{L}(\alpha, \overline{N}_\uparrow, \overline{N}_\downarrow) = \sum_{i=1}^{k} \log P(N_i|\alpha, \overline{N}_\uparrow, \overline{N}_\downarrow) \tag{3.18}$$

As an example, we used the resulting normalized histograms ($N_{\text{exp}} \times N_{\text{data}}$) from coherent operations with MW and TPSRT, with multiple repetitions per experiment (e.g. $N_{\text{exp}} = 200$), collected over an integration duration of approximately $100\,\mu$s, to fit a two-Poisson distribution and assign $\bar{N}_{|\downarrow\rangle}$ and $\bar{N}_{|\uparrow\rangle}$ (e.g. ≈ 2 and ≈ 0.2), as shown in Fig. 6. Using these fixed parameters, we fit α for the histogram of each data point (N_{exp} for $i \in N_{\text{data}}$), resulting from multiple repetitions.

Figure 19 illustrates the initialization of electronic states, coherent manipulation, and detection

of the spin-state probabilities. We show some of the dipole allowed transitions (MW0, MW1, MW2) of the ground-state manifold and use MW fields to coherently drive and prepare states with high fidelity. For the preparation of the state of any sublevels of the hyperfine manifold, we always start from the MW0 transition, using a composite discrete pulse sequence shown in Fig. 19 panel(a),(c) and (e). With dedicated experimental sequences, we calibrate the frequency and duration using Rabi spectroscopy, as shown in Fig. 19. Similarly, for efficient detection, we always revert the composite pulses to $F = 3, m_F = +3$, followed by fluorescence collection and spin-state probability analysis. Typically, the detection variance is higher for superposition cases compared to nearly pure states, due to projection noise [90]. With reduced state preparation and measurement errors (SPAM), this spin-population analysis method can be extended to detect states due to multiple indistinguishable ions [91].

In the case of motional states, with the employed Doppler beams, we initialize the motional mode in the thermal limit, following the Maxwell-Boltzmann distribution as given by Eq. 3.19. For preparing a motional mode near the ground state, we used resolved sideband cooling with a two-photon-stimulated Raman transition (TPSRT). By selecting beam combinations from Tab. 3, specifically options (2) ($\angle(\mathrm{B}_1, \mathrm{R}_2) = 120°$), (3) ($\angle(\mathrm{B}_3, \mathrm{R}_2) = 120°$), and (4) ($\mathrm{B}_3 \parallel -\mathrm{R}_1$), we achieve $\eta \approx 0.2(1)$, allowing strong coupling of the motional and electronic states, following the Laguerre dynamics as given by Eq. 3.20. Figure 20 shows the relative transition rate (normalized to the motional-state-insensitive transition rate) for the carrier, blue, and red sidebands as a function of motional states for two values of η: 0.1 and 0.3.

$$P(n) = \frac{\bar{n}^n}{(\bar{n}+1)^{n+1}} \tag{3.19}$$

$$\Omega_{n',n} = \Omega \exp\left[-\frac{\eta^2}{2}\right] \sqrt{\frac{n_<!}{n_>!}}\, \eta^{|n'-n|} L_{n_<}^{|n'-n|}(\eta^2) \tag{3.20}$$

Here, $n_<(n_>)$ is the lesser (greater) of n' and n, and L_n^α is the generalized Laguerre polynomial given by Eq. 3.21.

$$L_n^\alpha(X) = \sum_{m=0}^{n} (-1)^m \binom{n+\alpha}{n-m} \frac{X^m}{m!} \tag{3.21}$$

For calculations, we truncate the maximum Fock states to about 150. To realize an arbitrary motional state, we use the Qutip [92] package to define or calculate Fock distributions.

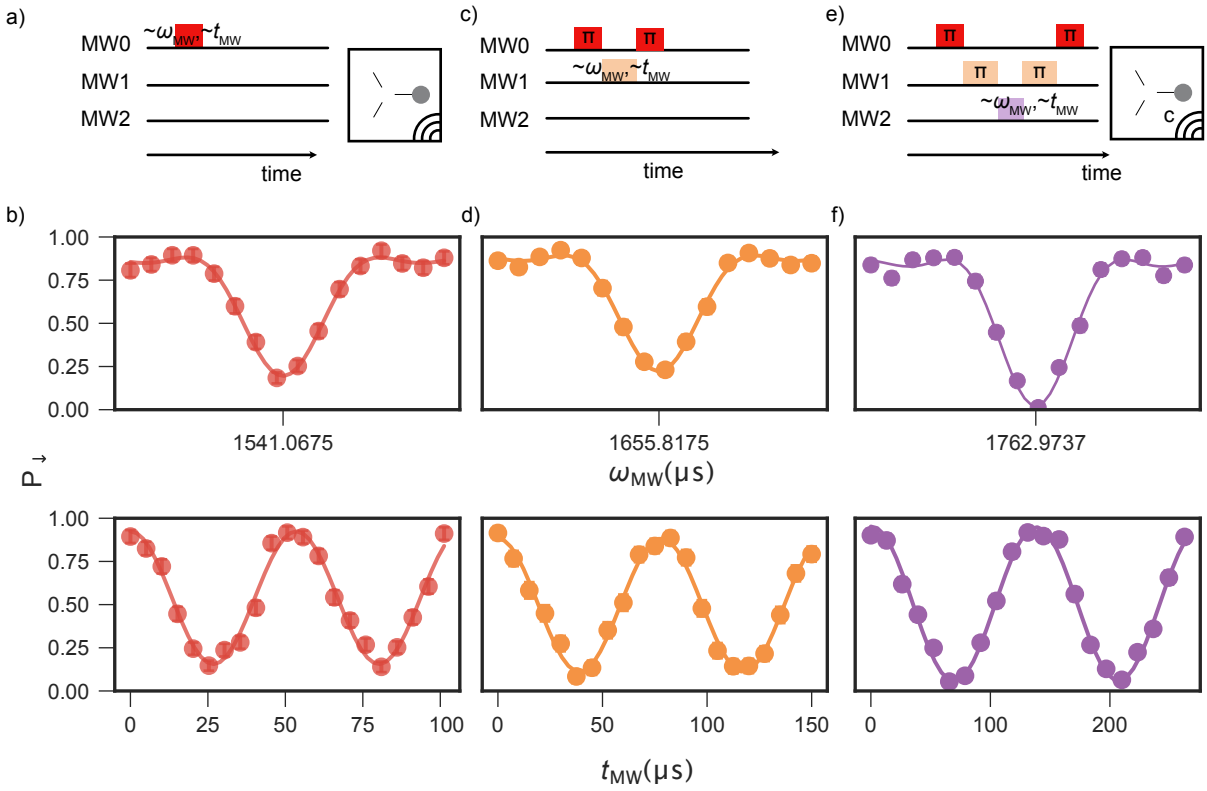

Figure 19: Qubit initialization. With all Doppler beams σ^+-polarized and aligned with the B-field, we prepare a single $^{25}Mg^+$ ion near the thermal limit, optically pumped to the $F = 3, m_F = +3$ state. Using MW, we can coherently prepare and utilize any two magnetic dipole-allowed transitions between sublevels of $F = 2$ and $F = 3$. Panel (a) shows the experimental sequence to couple the $F = 3, m_F = +3$ and $F = 2, m_F = +2$ sublevels, typically denoted as $|\downarrow\rangle$ and $|\uparrow\rangle$. This transition is labeled as MW0, with a field sensitivity of $-2\pi \times 21.76\,\mathrm{mT/MHz}$. A schematic with a triangular array and MW signal depiction is shown, which will be used to illustrate operations on the MW0 transition in later sections. Panel (b) shows two dedicated experimental measurements: first, scanning the transition frequency ω_{MW} to identify the resonance frequency and fine-tune the quantization field, and second, scanning the MW pulse duration t_{MW} to determine the duration that maximizes population in the $F = 2, m_F = +2$ state. Panel (c) shows the experimental sequence to probe the $F = 2, m_F = +2$ to $F = 3, m_F = +1$ transition after coherently preparing the $F = 2, m_F = +2$ state with pre-calibrated MW0 parameters. Panel (d) presents dedicated measurements to calibrate the transition frequency and π-pulse duration t_π. For detection, the ion is always shelved back to the $|\downarrow\rangle$ state. Panel (e) illustrates the experimental sequence for probing the most field-insensitive transition under the given quantization field, between the $F = 3, m_F = +1$ and $F = 2, m_F = 0$ levels, labeled as MW2. A schematic with the label **c** near the MW signal indicates the clock transition, which will be used to illustrate operations on the MW2 transition in later sections. Using pre-calibrated composite pulses, we prepare the $F = 3, m_F = +1$ state, followed by dedicated experiments shown in (f) to determine the transition frequency and t_π duration. For detection, the entire composite pulse sequence is played back in reverse to shelve the ion in the $|\downarrow\rangle$ state.

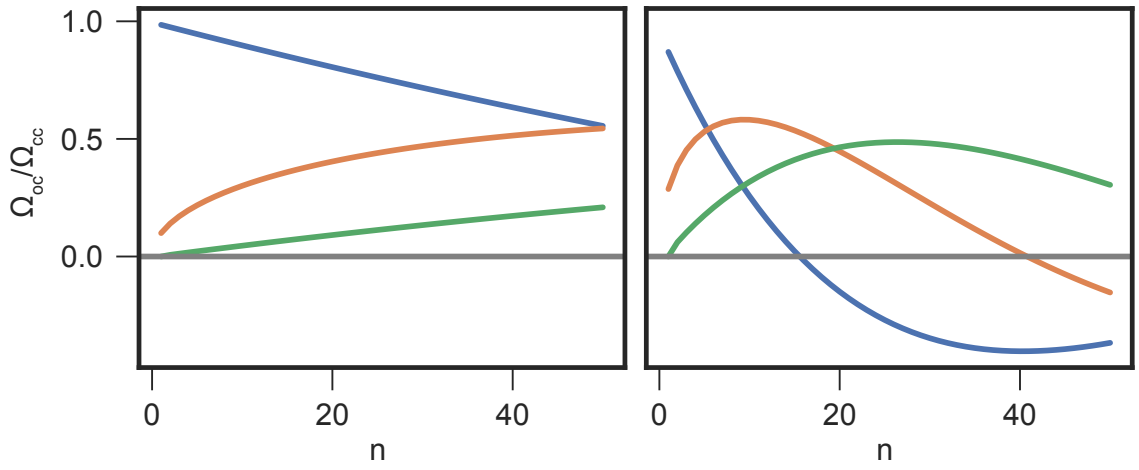

Figure 20: Comparison of $\Omega_{n',n}$ to the motional-state-insensitive TPSRT (with co-propagating beams). The left and right plots show carrier (blue), first (orange), and second (green) sideband dynamics for $\eta = 0.1$ and 0.3, representing a typical range for trap frequencies $\omega_i/2\pi$ in the range of $1 - 6$ MHz with Mg ions. In our case, for lower trap frequencies and with strong coupling, the Lamb-Dicke criterion is not satisfied ($\eta^2\bar{n} \approx 1$). We observe zero-crossing of the first sideband relative transition rate, leading to population trapping. In these exceptional cases, for sideband cooling, we employ interleaved higher-order sidebands, such as the second or third sideband, to transfer multiple phonons at once.

With a selected set of laser parameters that couple motional and electronic states, we enable coherent driving between the initial and final states ($|\downarrow, n\rangle$ and $|\uparrow, n'\rangle$), where $n' = n - 1$. As shown in Fig. 21a, after coherent transfer from the initial to the final state, we introduce a spontaneous process (RD/RP) to incoherently transfer $|\uparrow, n'\rangle$ to $|\downarrow, n'\rangle$ in two to three scattering events. Through multiple cycles of coherent transfer and incoherent processes, we reduce $\bar{n}_{th}$ to near the ground state. In the linear trap, we find that the lowest frequency mode does not satisfy the Lamb-Dicke criterion ($\eta^2\bar{n} \approx 1$). The right plot in Fig. 20 for $\eta \approx 0.3$ highlights a similar condition in which the population becomes trapped in $\bar{n} \approx 40$. In such cases, we employ higher-order sidebands, such as the second sideband, to enable the transfer of two phonons per coherent process to avoid population trapping.

In this work, we typically work with displaced (coherent) and thermal states. We use control and RF electrodes to prepare and coherently manipulate motional states. Using a single channel of an AWG, we drive at least one of the control or compensation electrodes with a uniform electric field for a fixed duration t_{exc} and amplitude E_{exc}, resonant with the frequency of the motional mode ω_i, which produces a vacuum state displaced with amplitude α and variance consistent with the uncertainty principle [93]. The probability distribution follows a Poisson distribution, as given in Eq. 3.22.

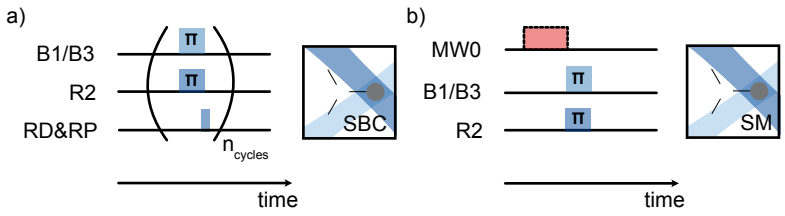

Figure 21: Experimental sequences for sideband cooling and spin-motion coupling. Panel (a) shows the experimental sequence for resolved sideband cooling using a motion-sensitive Raman beam configuration. With the relative detuning set to address the red sideband $\omega_{\text{qubit}} - \omega_i$, we expose the trapped ion to a two-photon process with pre-calibrated π-pulses. Subsequently, a short repumper beam is applied to induce a spontaneous decay process. This sequence is repeated multiple times for efficient cooling. In specific cases where the Lamb-Dicke criterion is not satisfied, we enable higher-order transitions $(\omega_{\text{qubit}} - n\omega_i)$ to assist with efficient cooling. The schematic with two crossed beams over an ion will be used in later sections to represent the resolved sideband cooling process. Panel (b) shows the sequence for spin-motion coupling. Using the same Raman beam configuration, we apply a calibrated two-photon pulse to imprint motional population information onto the spin state. In practice, we use an optional MW0 π-pulse to avoid recalibrating the two-photon beams during measurements. The schematic labeled as SM will be used in upcoming sections to represent the spin-motion coupling process.

$$P(n) = \frac{|\alpha|^{2n}}{n!} e^{-|\alpha|^2} \tag{3.22}$$

For a resonant drive, we find that the resulting $\bar{n}$ depends quadratically on the effective electric field (u_i, projected with the control electrode) and the duration t_{exc}, as given by Eq. 3.23.

$$\bar{n} = |\alpha|^2 = \left(\langle \vec{E}_{\text{exc}} \cdot \vec{u}_i \rangle\right)^2 \frac{t_{\text{exc}}^2 q^2}{8m\hbar\omega_i} \tag{3.23}$$

To analyze motional-state populations, we encode motional state information onto the electronic degrees of freedom, regardless of the binding regime. In the strong-binding regime, using TP-SRT to couple the motional and spin degrees of freedom (SM), we represent the population dynamics by Eq. 3.24, where decoherence γ_n accounts for the loss of coherence during spin-motion coupling.

$$P_{\downarrow}(t) = \frac{1}{2}\left(1 + \sum_{n=0}^{\infty} P_n e^{-\gamma_n t} \cos(2\Omega_{n',n} t)\right) \tag{3.24}$$

In the case of $\bar{n} \leq 3$, we use side-band contrast thermometry, as shown in Fig. 21b. By comparing

the contrast C of the red (RSB) and blue (BSB) sidebands under motion-sensitive TPSRT drive, we estimate $\bar{n}$ using Eq. 3.25, where $C = \frac{P_{\mathrm{RSB}}}{P_{\mathrm{BSB}}}$. In practice, we utilize an optional precalibrated pulse MW0 π in mid-experiment, to perform both red and blue sidebands subsequently to avoid systematics due to various drifts.

$$\bar{n} = \frac{C}{1 - C} \tag{3.25}$$

Figure 22 shows two examples: first, a motional mode at $\omega_1/2\pi \approx 3.8\,\mathrm{MHz}$, prepared in the thermal limit (gray) with $\bar{n} \approx 5$, where the contrasts of the red and blue sidebands are equal. In the second case, the same mode is prepared near the ground state using resolved sideband cooling, resulting in a near-complete suppression of the red sideband in the Fourier-limited spectrum. Alternatively, by tracking the spin-motion coupling as a function of the coupling duration t_{TPSRT}, as described in Eq. 3.24, we can fit a Fock distribution using prior information on decoherence γ_n and the transition rate between the initial and final states (e.g., $n = 0$ and $n = 1$) $\Omega_{1,0}$.

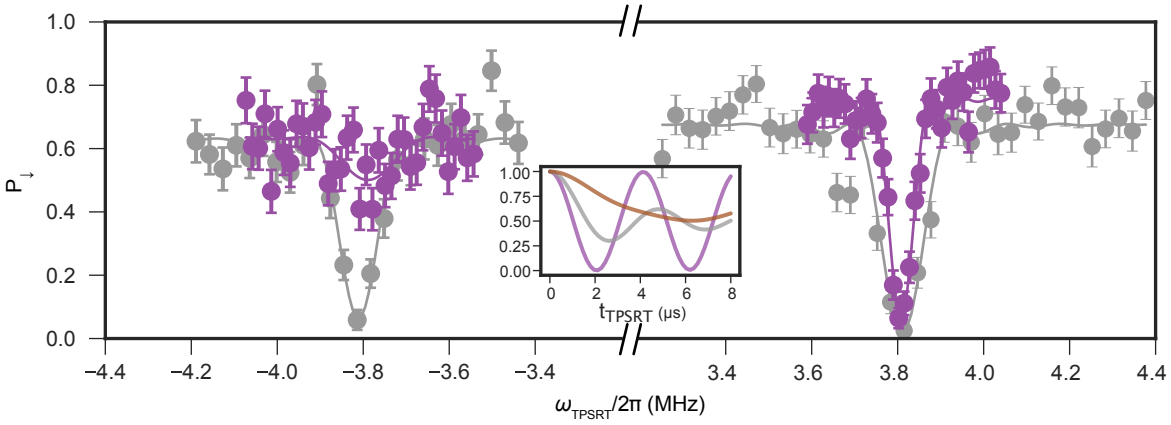

Figure 22: Detection of mean motional state population in the Lamb-Dicke regime. The plot shows experimental data for thermal ($\bar{n} \approx 5$, gray) and near-ground-state (purple) populations, measured via two-photon stimulated Raman transition addressing the lowest-frequency mode ($\omega_1/2\pi = 3.8\,\mathrm{MHz}$) at a fixed duration as a function of relative detuning ω_{TPSRT} over $2\omega_i$ (carrier transition not shown). By comparing the red and blue sideband amplitudes, we estimate the mean motional quanta in the range of approximately 0–3 quanta with high confidence. Inset: spin-motion trace at carrier frequency as a function of coupling duration t_{TPSRT} for three cases: near-ground-state (purple), thermal (gray), and $\eta^2\bar{n} \approx 1$ ($\bar{n} \approx 100$, brown).

In the weak-binding regime, we detect motional populations above the Lamb-Dicke criterion ($\eta^2\bar{n} > 1$) in the range of approximately 100–10,000 quanta. For a prepared coherent state, the extent of the wave function A_i modulates the fluorescence spectrum F_{ω_i}, due to the transfer of motional population to higher-order sidebands ($n\omega_i$), as given by Eq. 3.26. To accurately esti-

mate the motional population, we determine the modulation index $\beta = |\langle \mathrm{u}_i \cdot \mathrm{k}_{\mathrm{laser}} \rangle| \, A_i$, with calibration of parameters such as the effective overlap of the laser mode. For calculations, we assume minimized micromotion, suppressed anharmonic contributions, and on-resonant detection.

$$F_{\omega_i}(\Delta_{\mathrm{det}}, \beta) = \sum_{n=-\infty}^{\infty} \frac{J_n^2(\beta)}{(\Delta_{\mathrm{det}} + n\omega_i)^2 + (\Gamma/2)^2} \tag{3.26}$$

Figure 23 shows two cases of coherent excitation, prepared with the oscillation drive amplitude $U_{\mathrm{exc}} = 0.5\,\mathrm{V}$ and the excitation durations $t_{\mathrm{exc}} \approx 15\,\mu\mathrm{s}$ and $20\,\mu\mathrm{s}$. Using the drive frequency $\omega_{\mathrm{exc}}/2\pi$ as a scan variable, we detect the modulated fluorescence spectrum. With a Sinc model fit, we extract amplitudes and mode frequency information from the Fourier-limited spectrum. Based on amplitude information, using Eq. 3.26, we estimate $\bar{n}$ to be about 3000 and 5000 quanta, respectively.

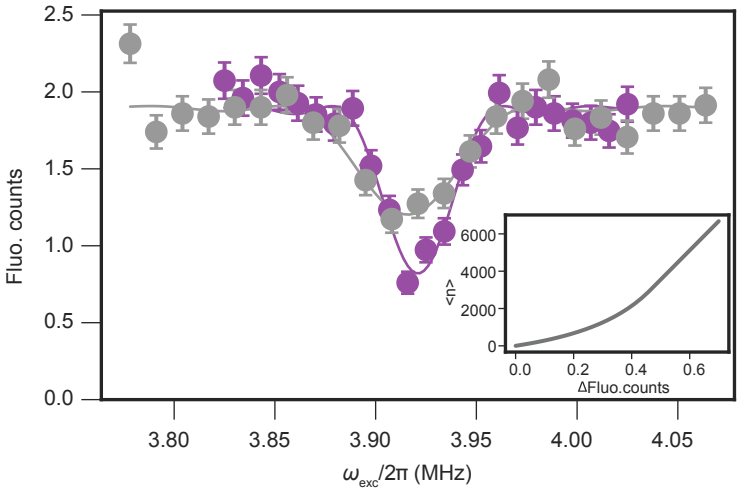

Figure 23: Detection of motional population in the weak-binding regime. The plot shows results of coherent excitation for two different excitation durations, $t_{\mathrm{exc}} \approx 15\,\mu\mathrm{s}$ (gray) and $20\,\mu\mathrm{s}$ (purple), with $U_{\mathrm{exc}} = 0.5\,\mathrm{V}$, leading to mean motional excitations of approximately 3,000 and 5,000 quanta, respectively. Inset plot shows estimated mean motional population as a function of relative fluorescence change, calculated using Eq. 3.26, assuming minimal micro-motion (MM) and negligible higher-order contributions.

3.1.3 Operational Limitations

In our platform, we evaluate the limitations of performing coherent operations within two primary components: the hyperfine ground-state manifold and the degrees of freedom of the harmonic oscillator. We define our spin-1/2 system using the hyperfine manifold (see Fig. 6), with laser-less control fields enabling high-fidelity state manipulation (see Fig. 19). The loss of coherence in the hyperfine manifold is mainly the result of decoherence and dephasing. The main sources of dephasing are (1) magnetic field fluctuations, (2) timing and phase jitter in control fields, which introduce state preparation errors, and (3) oscillating magnetic fields near resonance with certain magnetic dipole-allowed transitions. Regarding decoherence, the exceptionally long-lived nature of the manifolds rules out intrinsic decay mechanisms; however, induced processes from on- and off-resonant scattering events [63] may still contribute.

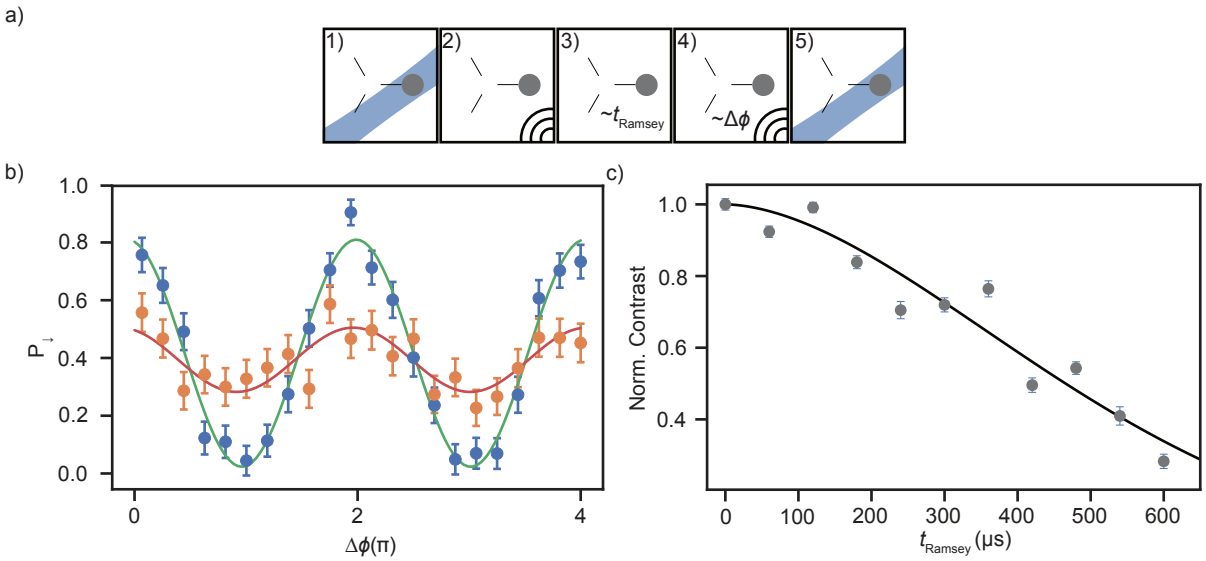

Figure 24: Estimation of dephasing time T_2^* via Ramsey spectroscopy on the most field-sensitive transition. (a) Experimental sequence: (1) A single ion is initialized at the T_2 site at the thermal limit and optically pumped into the $F = 3, m_F = +3$ state. (2) A calibrated $\pi/2$ microwave pulse creates a superposition between the $F = 3, m_F = +3$ and $F = 2, m_F = +2$ states. (3) A variable wait period, t_{Ramsey}, is applied. (4) An analysis $\pi/2$ pulse with a variable phase $\Delta\phi$ is then applied. (5) Finally, fluorescence is collected to estimate the spin-state probability. (b) Resulting $P_\downarrow$ for two wait times, 0 and 600 μs, as a function of analysis phase. (c) Normalized contrast as a function of t_{Ramsey}. An exponential model fit to the data gives a dephasing time of $T_2^* = 600(20)$ μs.

We employ the most field-sensitive qubit transition, $F = 3, m_F = +3 \leftrightarrow F = 2, m_F = +2$ (labeled MW0), which has a sensitivity of $-21.76\,\text{MHz/mT}$ [85], to assess the limitations of coherent operations due to accumulated factors. As shown in Fig. 24, we measure coherence time using Ramsey spectroscopy with separated fields and a variable waiting period t_{Ramsey}. Following a calibrated $\pi/2$ pulse to prepare the superposition state, we introduce a variable

waiting period and apply a second MW $\pi/2$ pulse with a variable analysis phase $\Delta\phi$ to examine interference effects. Using sinusoidal model fits, we extract the coherence amplitude and phase information as functions of different wait periods. Figure 24 presents the experimental data with normalized amplitudes, where exponential fits yield a T_2^* time of $600\,\mu\text{s}$. Given that the coherence time is considerably longer than that required for most laser and laserless interactions, we employ this transition as a two-level system for most experimental studies unless explicitly stated otherwise.

With the first-order least field-sensitive transition of the hyperfine manifold (labeled as $|\downarrow\rangle_c$ and $|\uparrow\rangle_c$) (see Fig. 6) at $\vec{\text{B}} \approx 10.95\,\text{mT}$, we measure the coherence time to benchmark field stability and assess the effect of induced decoherence due to incident radiation. Figure 25a shows the experimental sequence: a Ramsey spectroscopy with separated MW fields and a waiting duration t_{Ramsey}, as in the previous sequence (see Fig. 24), with one modification (neutral density filter) to distinguish two different conditions. First, composite pulses consisting of two π-pulses achieve complete population transfer from $F = 3,\, m_F = +3$ to $F = 3,\, m_F = +1$ via $F = 2,\, m_F = +2$, followed by a $\pi/2$-pulse to prepare the superposition state (see Fig. 19). Second, after a variable waiting duration and a $\pi/2$-pulse with a variable analysis phase $\Delta\phi$, we use reverse composite pulses to prepare the ion in $F = 3,\, m_F = +3$ for efficient fluorescence detection. To distinguish between mechanisms contributing to coherence loss, such as stray photon incidence and magnetic field instability, we introduce a neutral density (ND) filter on the beam path of the preparation and detection beams (BD, BDD, RP, RD, BDx) to significantly improve the optical extinction ratio (contrast between laser on- and off-conditions). We compensate for the reduction of overall intensity by increasing the output power of all beams, thus further increasing the contrast between on- and off-conditions. Figure 25b shows the collected relative coherence amplitudes as a function of the delay time t_{Ramsey}, with and without the ND filter. We achieve T_2^* dephasing times of about 10 ms without the ND filter. With the ND filter reducing the impact of stray photon incidences, we estimate a ten-fold improvement in T_2^*. Compared with the linear trap (as shown in Tab. 4), we report magnetic field stabilities of up to 10^{-4}, resulting in coherence times of up to 6 seconds [48]. We suspect the presence of oscillating fields $\vec{\text{B}}$ from pseudopotential generating RF fields near $\Omega_{\text{RF}}/2\pi = 52\,\text{MHz}$, along with the intricate design of the RF electrodes, contributes to the coherence loss. Spin-echo sequences can be employed to estimate the presence of oscillating magnetic fields near the vicinity of the ion [48]. Nevertheless, the currently measured coherence time is sufficiently longer than most of the pulsed experimental routines in this work.

In the case of harmonic oscillator modes, we benchmark factors that contribute to overall coherence loss. In this work, we define "motional dephasing" as mechanisms that lead to a loss of phase information between different Fock states where energy is conserved. We use "motional decoherence" to describe cases in which energy is not conserved, such as in motional mode

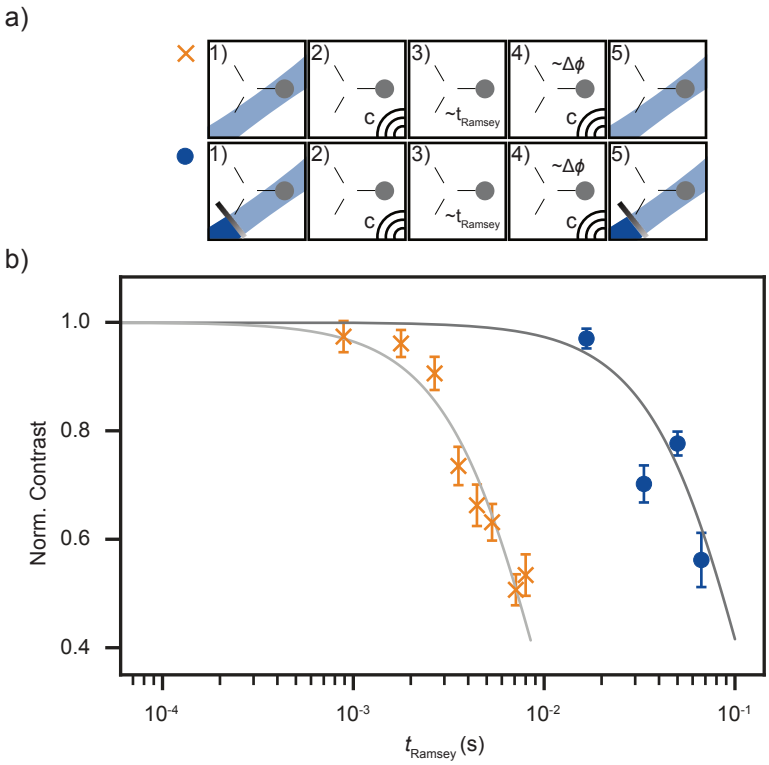

Figure 25: Induced decoherence in ground-state hyperfine states due to interaction with stray photons. Using Ramsey spectroscopy and the field-insensitive transition ($F = 3, m_F = +1 \leftrightarrow F = 2, m_F = 0$), we estimate T_2^* under different conditions. (a) shows two similar experimental sequences, with and without a Neutral Density (ND) filter. In the second case (disk), the ND filter is placed in the path of the preparation beams (BD, BDD, RP, and RD) to attenuate stray light and improve the optical extinction ratio (contrast between laser on and off states). 1) In both cases, a single $^{25}Mg^+$ ion is initialized at the T_2 site, cooled to the thermal equilibrium T_D, and optically pumped to the $F = 3, m_F = +3$ state. 2) The electronic superposition state of $F = 3, m_F = +1$ labeled as $|\downarrow\rangle_c$ and $F = 2, m_F = 0$ labeled as $|\uparrow\rangle_c$ is prepared using a composite Ramsey MW $\pi/2$ pulse. 3) After a waiting period t_{Ramsey}, the ion interacts with ambient environment. 4) A second $\pi/2$ pulse with a variable phase $\Delta\phi$ probes the coherence, followed by shelving pulses to prepare the ion in the $F = 3, m_F = +3$ state. 5) Finally, the fluorescence is collected for spin-state analysis. (b) shows the data for normalized contrast (extracted with sinusoidal fits on interference results) as a function of the wait duration t_{Ramsey}, with and without the ND filter. A ten-fold increase in coherence time is observed with ND filter isolation, indicating that near- and off-resonant stray light interactions contribute to decoherence of the internal state.

	Ion-to-surface distance (μm)	T_2^* (MW0)	T_2^* (MW2)
Linear trap	80	500-600 μs	6 s [48]
Triangular array	40 (T_2 site)	600 μs	>100 ms

Table 4: Comparison of dephasing times between two surface-electrode trap platforms on most and least field sensitive transitions.

heating. On our platform, coherence limitations stem from motional dephasing caused by fluctuations in the parameters of generating potentials and control fields, as well as from motional decoherence arising from various noise sources.

For both trapped-ion platforms (see Fig. 1 and Fig. 2) (linear and triangular arrays), we assess the bandwidth limitations of the motional modes generated due to confinement predominantly by either static or oscillating fields. For this estimation, we employ displaced thermal states with variable coherent excitation durations (t_{exc}) to determine the minimal resonance width (σ_{exc}), which defines the bandwidth limit for manipulating the addressed motional mode. In both platforms, we initialize a single ion at thermal equilibrium (T_D) (at T_2 site of the triangular array). Using a coherent oscillating field $A\cos(\omega_{\text{exc}}t_{\text{exc}} + \phi)$, applied via appropriate control electrodes, we generate displaced thermal states, followed by fluorescence collection via a PMT for analysis within the weak-binding regime (see Fig. 23). As the excitation duration t_{exc} varies, we adjust the signal amplitude A to maintain a constant excitation rate. Applying a Sinc model fit to the fluorescence data as a function of frequency (ω_{exc}), we extract resonance widths (σ_{exc}) across excitation durations and plot them in Fig. 26b and Fig. 26c. Using a composite model fit that includes the Fourier limit $(1/t_{\text{exc}})$ + offset, we find bandwidth limitations ($\sigma_{\text{exc}}/2\pi$) of approximately 10 Hz and 1 kHz for motional modes confined predominantly by static (linear trap) and oscillating fields (triangular array), respectively.

To estimate the motional dephasing rate [94, 95], we apply a displacement operator D to an initial state, resulting in $|\alpha\rangle$. After an optional waiting duration t_{wait}, a second displacement operation is applied with a controlled relative phase ($\Delta\phi$), producing $|2\alpha\rangle$ for $\phi = 0°$ and returning to the initial state $|\text{init}\rangle$ for $\phi = 180°$. By scanning the relative phase $\Delta\phi$ as a function of the waiting time t_{wait}, we observe interference effects to evaluate coherence amplitudes, analogous to the Ramsey technique (see Fig. 24). Figure 27 shows the experimental sequences executed in two motional modes on two different platforms. In the case of the linear trap (see Fig. 2), we choose the motional mode generated by confinement provided by a static field. In the case of the triangular array (see Fig. 1), we choose the motional mode generated by confinement provided by an oscillating field. The inset plot shows experimental data for two different waiting durations (t_{wait}) of 0 and $500\,\mu\text{s}$, as an example acquired for the triangular array. Using a sinusoidal model fit, we extract contrast information as a function of t_{exc}. In Fig. 27b, we plot the extracted coherence amplitudes over various waiting durations (t_{wait}). Using a model fit that includes exponential decay, we determine dephasing times of approximately $500\,\mu\text{s}$ and $15\,\text{ms}$ for the two motional modes on the two different platforms.

In our methods, we briefly outline some systematic factors that lead to an under- or overestimation of observables. Since methods for determining decoherence involve coherent states with high amplitudes, we must consider contributions from anharmonicities introduced by the trap

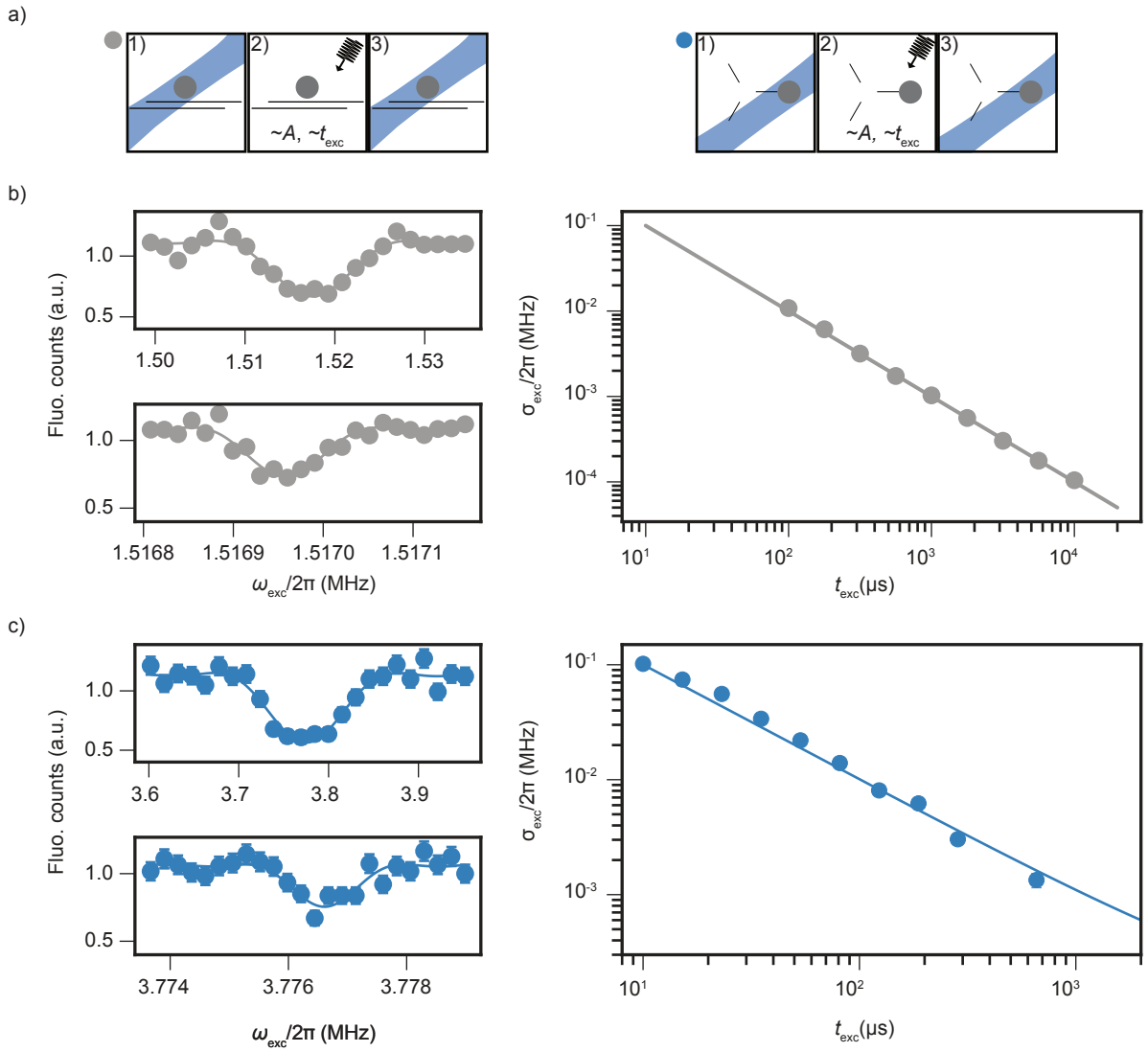

Figure 26: Bandwidth of the motional modes in two platforms. In case of the linear trap, the confinement is provided by a static field and in the case of the triangular array, the confinement is provided by an oscillating field. (a) illustrates identical experimental sequences performed on the axial (statically confined) mode (gray disk) in the linear surface-electrode trap (shown in Fig. 2) and on a radial mode (blue disk) in the triangular array. 1) A single ion is initialized at the thermal limit using Doppler beams. 2) The motional mode of choice is coherently excited with a rectangular pulse of variable frequency ω_{exc}. For each pulse duration t_{exc}, the pulse amplitude A is scaled to ensure a constant excitation rate. 3) Finally, fluorescence detection is used to analyze the motional mode observables (using Eq. 3.26). (b) (left) shows two example plots with t_{exc} of 10 and $10,000\,\mu\text{s}$; using a Sinc model fit, we find resonance widths $(\sigma_{\text{exc}}/2\pi)$ of $100\,\text{kHz}$ and $100\,\text{Hz}$, respectively. (b) (right) plots resonance widths (σ_{exc}) as a function of t_{exc}, with a composite model fit (Fourier limit + offset, gray fit) showing that the bandwidth $(\sigma_{\text{exc}}/2\pi)$ for the motional mode confinement provided with the static field approaches approximately 10 Hz. Similarly, (c) (left) shows two example plots with coherent excitation durations t_{exc} of $10\,\mu\text{s}$ and $285\,\mu\text{s}$, yielding resonance widths $(\sigma_{\text{exc}}/2\pi)$ of $100\,\text{kHz}$ and $3\,\text{kHz}$, respectively. (c) (right) summarizes the data with a fit, indicating that the bandwidth $(\sigma_{\text{exc}}/2\pi)$ of the motional mode confined with an oscillating field approaches approximately 1 kHz.

configuration. Additionally, most active components of the control field are neither referenced nor actively stabilized, so amplitude, timing, and phase jitters in the control fields can alter our estimations. Lastly, the bandwidth and dephasing of a chosen motional modes are highly susceptible to changes in control potential configurations, such as variations in mode orientation, gradients, and positional shifts. For improved sensitivity, we can prepare a superposition state, such as $|0\rangle$ and $|1\rangle$ on the Fock basis, or in Schroedinger cat states, to analyze different decoherence mechanisms [16]. Furthermore, techniques such as reconstructing the density matrix or the Wigner function can provide further insight [96]. Overall, we infer that the oscillating RF field provided by our setup (see Fig. 10a) is relatively less stable compared to the static fields provided by multiple channels of AWG (see Fig. 10b). We can employ active stabilization techniques on the oscillating field to improve its stability [97, 98].

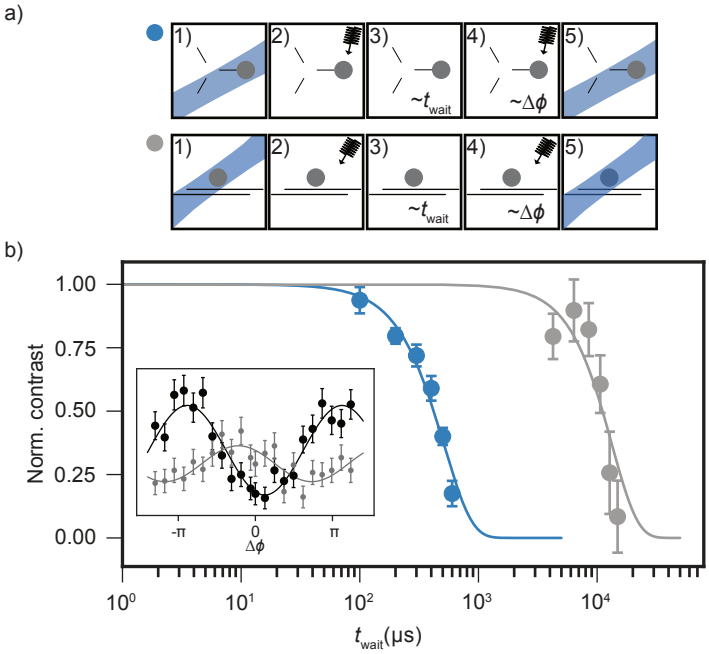

Figure 27: Estimating motional phase coherence of two motional modes in two different platforms (linear and triangular array). (a) illustrates two identical experimental sequences performed on two platforms: Triangular array (blue) and Linear trap (gray). 1) A single ion is initialized at the thermal limit. 2) We apply the first coherent rectangular pulse for a fixed duration at a pre-calibrated trap frequency to prepare a displaced thermal state. 3) Following a variable waiting duration t_{wait}, the trapped ion oscillator interacts with the environment. 4) Next, we apply a second identical displacement pulse with a variable relative phase $\Delta\phi$. 5) Finally, fluorescence detection is performed for analysis. (b) shows extracted data for various delay durations across the two different platforms. The inset shows two examples (from triangular array) with wait durations (t_{wait}) of 0 and 500 μs, with coherence amplitudes extracted via sinusoidal model fit. For the motional mode confined with an oscillating potential, we estimate a dephasing time of $527(22)$ μs with an exponential decay model fit, compared to the motional mode confined with a static potential, which demonstrates a dephasing time of approximately 15 ms.

The second major factor in coherence loss is the coupling of harmonic oscillator modes to a noisy environment. Regardless of the noise source, we can model it as a thermal source that induces incoherent excitations of the motional mode. Additionally, irrespective of the coupling strength, scaling factors, or types of mechanism, we use a single trapped-ion mode as a sensor to estimate noise levels in our ambient-temperature setup. We benchmark our platform across different regimes using two different methods: sideband thermometry (see Fig. 28) in the strong-binding regime ($\Gamma \ll \omega_i$) and fluorescence-based method (see Fig. 23) in the weak-binding regime ($\Gamma > \omega_i$).

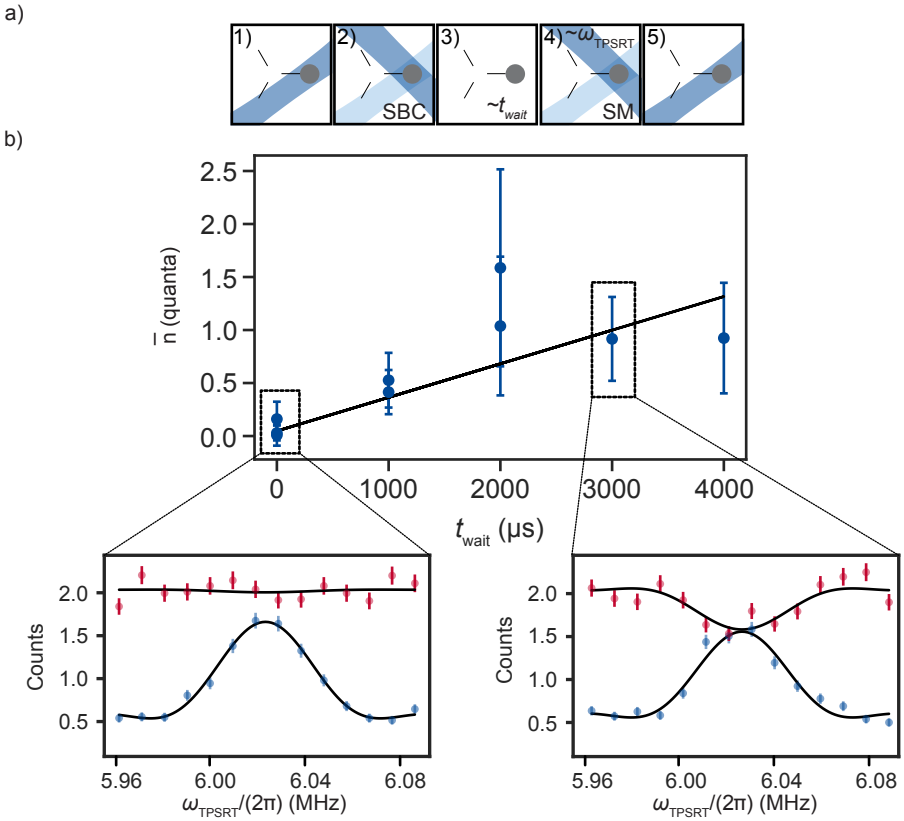

Figure 28: Heating rate measurement using sideband contrast thermometry. (a) Experimental sequence: 1) A single $^{25}Mg^{+}$ ion is initialized at the T_2 site at the thermal limit. 2) Dedicated Raman beams (B_1+R_2), with a Lamb-Dicke parameter $\eta \approx 0.1$, are aligned to address the motional mode ω_2, oriented primarily toward the center of the triangular array. Using resolved Raman sideband cooling, we cool the ion to near-ground state. 3) Following a variable wait duration, t_{wait}, we allow the oscillator to interact with environmental sources. 4) Using the same Raman beam configuration, we drive the red and blue sidebands, with relative detuning ω_{TPSRT} as a scan variable. 5) Finally, fluorescence is collected to estimate the mean motional population using sideband contrast thermometry (given in Eq. 3.25), based on the relative amplitudes of the red and blue sidebands. (b) The collected data show mean motional population as a function of t_{wait}. A linear model fit yields an estimated heating rate of approximately 0.3 quanta/ms. We highlight results for two values of t_{wait} (0 and 3 ms) to illustrate red and blue sideband scans and the corresponding amplitude differences over t_{wait}. For $t_{\text{wait}} = 0$, we estimate $\bar{n} \approx 0$ due to the near absence of red sideband. While for $t_{\text{wait}} = 3$ ms, we measure $\bar{n} \approx 1$ quanta.

In the strong-binding regime, we employ sideband thermometry, a method that compares the contrast or rates of red and blue sidebands to estimate the final mean motional state population, as defined by Eq. 3.25. Figure 28a shows the experimental sequence, and Fig. 28b shows an example measurement of the motional heating rate. For a selected motional mode ($\omega_2/2\pi \approx 6\,\text{MHz}$ at the T_2 site), we use a pair of Raman beams (B_1+R_2) with $\eta \approx 0.1$ to sideband cool the mode (sequence shown in Fig. 22a), followed by a variable waiting period, t_{wait}. We then measure the red and blue transitions as functions of ω_{TPSRT} for a precalibrated duration of t_{rsb}, as illustrated in Fig. 22b. Repeating this sequence for varied t_{wait} durations, we plot the estimated mean motional population, $\bar{n}$. We highlight analysis of individual t_{wait} for two cases: 0, and $3000\,\mu\text{s}$. With the fit of the Sinc model, we estimate the contrast of the red and blue sidebands. In the case of $t_{\text{wait}} = 0\,\mu\text{s}$, we estimate near motional ground-state $\bar{n} \approx 0$, due to near absence of red-side band. While in the case of $t_{\text{wait}} = 3000\,\mu\text{s}$, we estimate a gain of mean thermal population $\bar{n} \approx 1$ quanta. Figure 28b shows collected mean population as a function of t_{wait}. Using a linear model fit, we determine that the heating rate ($\dot{\bar{n}}$) of the motion mode ω_2 is approximately 0.3 quanta/ms.

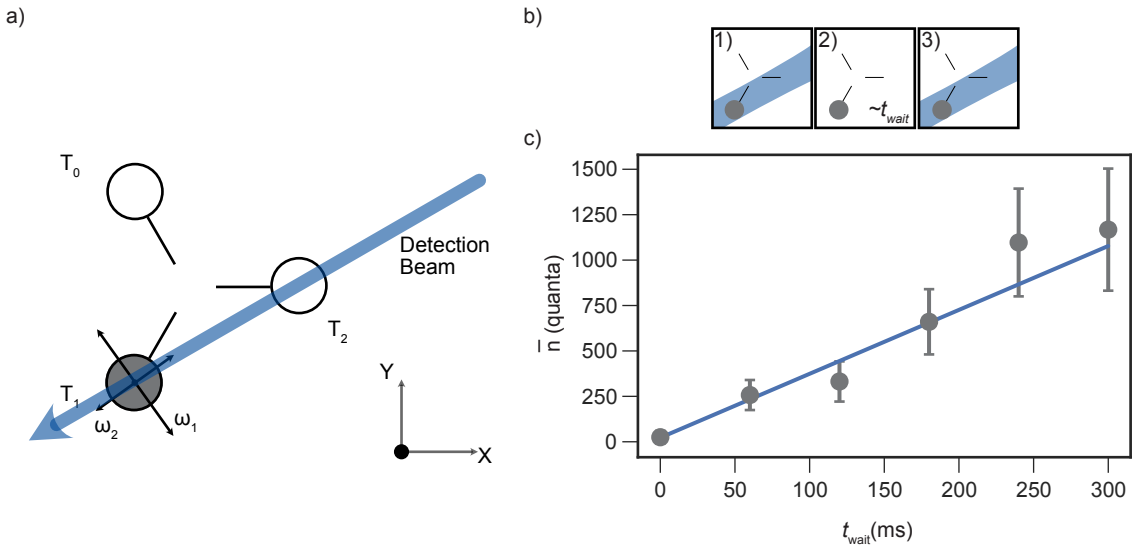

Figure 29: Estimation of motional mode heating rate using modulation of fluorescence spectra. (a) Schematic representation illustrating that the motional mode ω_2 of a single ion trapped at the T_1 site has its motional mode vector ($\vec{u}_2$) orientation overlaps with the Doppler beams, leading to appreciable $\eta \approx 0.1$. While the other motional mode vectors such as ($\vec{u}_1$ and $\vec{u}_3$) have negligible projection ($\eta \approx 0$) with the Doppler beams under the control potential configuration used in this measurement. (b) Experimental sequence: 1) A single ion is initialized at the T_1 site at the thermal equilibrium T_D. 2) Following a variable wait duration, t_{wait}, the oscillator interacts with the thermal environment. 3) Fluorescence is detected using a near-resonant Doppler beam (BDx) to analyze the mean motional population $\bar{n}$ via Eq. 3.26. (c) The estimated $\bar{n}$ is plotted as a function of t_{wait}. A linear model fit yields a heating rate of approximately 3 quanta/ms for the addressed mode, assuming negligible η contributions from other modes.

In the weak-binding regime, several methods are suggested for measuring motional mode heat-

ing, such as the Doppler re-cooling method [99, 100]. Alternatively, we used fluorescence modulation to estimate the mean motional population distribution. Although this technique is less sensitive than sideband thermometry, it has a wider dynamic range, allowing measurements of 100-5000 quanta. In our setup, Doppler beams are employed to cool (if possible) all motional modes to the Lamb-Dicke regime [1]. Unlike a coherent state, a thermal distribution is not spectrally resolved, and fluorescence modulation includes contributions from all motional modes. Due to scaling differences across orientations, we cannot resolve individual contributions from specific motional modes. Alternatively, we can adjust motional-mode orientations with curvature terms (see Eq. 3.2) to optimally address a single motional mode with Doppler beams, by ensuring maximal projection. As shown in Fig. 29, we select the T_1 site, where two of the three modes minimally contribute to fluorescence changes due to their low Lamb-Dicke parameters with Doppler beams. For the motional mode chosen at $\omega_2/2\pi \approx 6\,\text{MHz}$, we ensure the maximal projection of motional mode vector ($\vec{u}_2$) with the Doppler beams, by controlling the orientation via curvature terms. With Doppler beams, we prepare all the motional modes in thermal equilibrium (as shown in Tab. 2). Following a variable waiting duration t_{wait}, we measure the resulting fluorescence with the near-resonant detection beam (BDx). Using a linear model fit, we determine the heating rate to be approximately $\dot{\bar{n}} \approx 3\,\text{quanta/ms}$ for the motional mode ω_2 addressed at the T_1 site using the fluorescence modulation method. In cases of higher heating rates that lead to inefficient cooling with resolved sideband cooling, the fluorescence modulation method serves as an alternative, providing an extended range for estimating the heating rate.

[1] Modes below $2\pi \cdot 2$ MHz are not in the Lamb-Dicke regime

3.2 Advanced

In this chapter, we introduce specialized experimental methods developed to extend the existing tools for a trapped-ion array. We begin by describing a technique for measuring motional states within a regime inaccessible to conventional methods for quantifying low motional quanta (the quantum regime) or high populations using fluorescence (the classical regime) (Section 3.2.1). Next, we demonstrate intrasite coupling between motional modes, enabling coherent control of ion motion within a single site through laser-less local modulation capabilities (Section 3.2.2). To support these experiments, we also establish an automated loading system using a pulsed ablation laser, achieving high-efficiency single-ion trapping (Section 3.2.3). Furthermore, we outline the process for transporting ions between different sites in our array, allowing for stable and controlled positioning within our 3D potential landscape (Section 3.2.4). Finally, we investigate the noise sources that cause unwanted heating in the ion's motion, implementing solutions to mitigate these effects, including in situ surface cleaning (Section 3.2.5). Together, these methods significantly enhance the experimental capabilities and control over the trapped ion array.

3.2.1 Transient regime: Motional State Detection

In this subsection, we explore a transient regime in which the motional population distribution cannot be reliably detected using traditional methods. Specifically, the fluorescence method fails in the quantum regime, as shown in Fig. 23, while sideband thermometry proves insufficient in the classical regime, as illustrated in Fig. 28. For our Lamb-Dicke parameter ($\eta \approx 0.2$), this regime is defined as ($1 \leq \eta^2\bar{n} < 10$). To overcome these limitations, we employ a method referred to as the carrier method in the upcoming chapters. This method leverages the dynamics governed by generalized Laguerre polynomials to numerically extend the detection range and access the transient regime. By mapping the motional population through carrier transitions ($|n,\downarrow\rangle \Leftrightarrow |n,\uparrow\rangle$), we extend the detectable range to states with mean motional populations in the range of $\bar{n} = 20-60$, for η in the range of $0.1-0.3$. This approach bridges the sensitivity gap of conventional techniques, enabling the analysis of motional populations that were previously inaccessible, and provides a crucial tool for studying and manipulating motional states in this intermediate regime.

Unlike self-calibrated techniques, such as sideband thermometry, our carrier method requires prior information about the motional mode, such as the Lamb-Dicke parameter η. To illustrate this method with a simple one-dimensional model, we prepare the T_2 site and tune the motional mode parameters to enable a chosen set of Raman beams (B_3 and R_2) to address a single

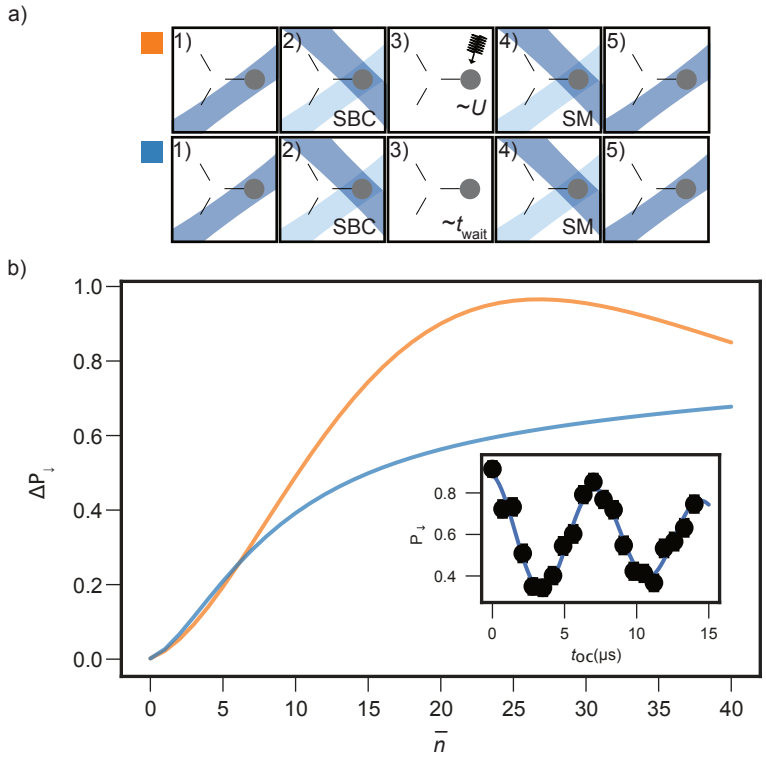

Figure 30: Spin-motion dynamics of coherent and thermal distributions at the carrier transition. (a) illustrates two experimental sequences proposed to detect coherent (orange) and thermal (blue) distributions in a single, ground-state-cooled motional mode. 1) A single trapped ion is initialized at the thermal limit. 2) The addressed mode is cooled near the ground state with dedicated Raman beams. 3) The mode is either coherently excited (orange) or allowed to interact with the environment for a fixed waiting duration (blue) to achieve thermal excitation. 4) Spin-motion coupling is performed using the same Raman beam configuration. 5) Photons detected with near-resonant Doppler beams are used for motional population analysis. (b) shows calculated traces of relative $P_{\downarrow}$ probability for coherent and thermal distributions up to $\bar{n} = 40$ for $\eta \approx 0.2$, using Eq. 3.24 with mean motional states as the only variable parameter. The inset displays experimental data for the spin-motion trace as a function of coupling duration (t_{oc}) with a two-photon stimulated Raman transition using laser beams to address the carrier transition, with an effective Lamb-Dicke parameter $\eta \approx 0.2$. A sinusoidal fit is applied to extract parameters such as the Rabi rate ($\Omega_{oc}/2\pi \approx 125\,\mathrm{kHz}$), the decoherence rate ($\Gamma_d/2\pi \approx 9\,\mathrm{kHz}$), and spin population infidelities, which are used as fixed parameters for calibration traces.

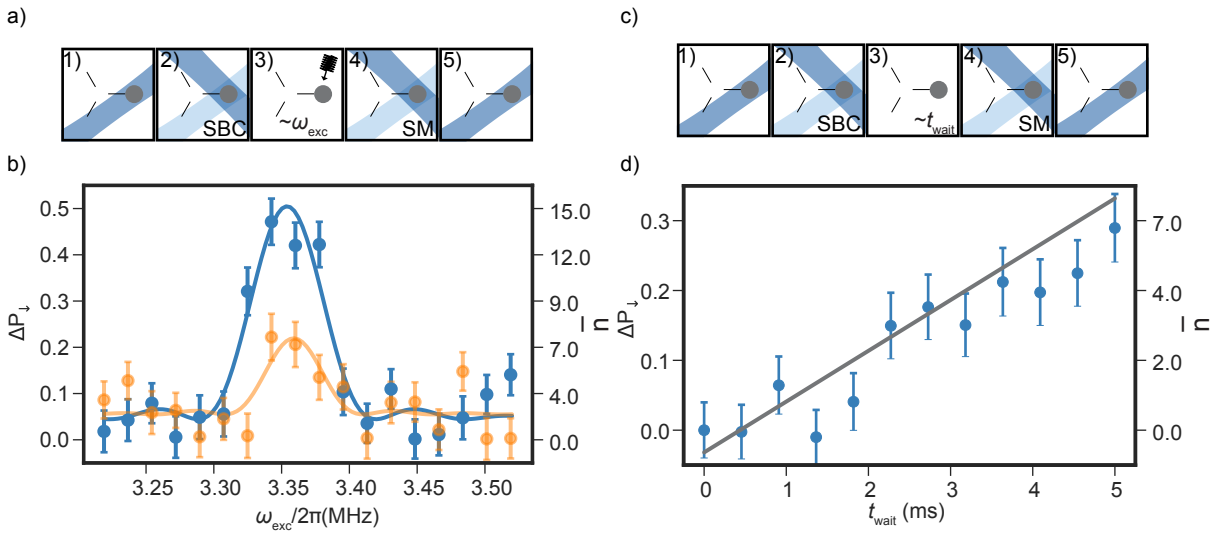

Figure 31: Coherent and thermal excitations estimated using the carrier method. (a) depicts the experimental sequence. 1) A trapped ion at the T_2 site is initialized at the thermal limit. 2) Sideband cooling (SBC) is applied to bring the addressed motional mode $\omega_1/2\pi \approx 3.36\,\text{MHz}$ near the ground state. 3) The lowest frequency mode is coherently excited with two potential amplitudes U_{exc}, 1 and 1.5 V. 4) Spin-motion coupling is performed with a pre-calibrated carrier pulse under near-ground-state conditions. 5) Fluorescence detection is used for motional population analysis. (b) shows the experimental data, with the left y-axis indicating the change in population and the right y-axis showing the estimated mean population, primarily due to coherent excitation. With a Sinc model fit, we estimate mean motional populations of approximately 7 and 15 quanta, respectively. (c) is similar to (a) but includes a wait period instead of coherent excitation, allowing for interaction with the environment, resulting in thermal excitations. (d) shows the experimental data, with the right y-axis attributing population changes to the mean thermal population. A linear fit yields a heating rate of approximately 1.2 quanta/ms.

motional mode ω_1 with $\eta_1 \approx 0.2$, while the other two modes have negligible projections, close to zero (η_2 and $\eta_3 \approx 0$). Figure 30a shows the experimental sequences and calibration curves proposed to detect motional populations. With a motional mode almost in the ground state, the experiment proceeds with motional state manipulation, fluorescence detection, and subsequent spin probability analysis. As a prerequisite calibration, we acquire a spin-motion trace (inset) of ω_1 near the ground state. Using a sinusoidal model fit, we extract the Rabi rate Ω_{oc}, the decoherence rate Γ_d, and the infidelities in the spin-state probabilities. We perform calculations for two cases: coherent states (orange), represented as a function of the applied oscillating signal amplitude U_{exc}, and thermal states (blue), where the motional mode interacts with the environment at varying times t_{wait}. Figure 30b shows the calculated curves of the relative spin population $\Delta \text{P}_{\downarrow}$ as a function of the mean motional states, representing coherent (orange) and thermal (blue) distributions. We use $\Delta \text{P}_{\downarrow}$ to account for the infidelities of state preparation, which, along with higher decoherence rates, reduce the sensitivity of the method. The calculations are based on Eq. 3.24, with a fixed duration determined by the carrier transition rate Ω_{oc}, and various Fock distributions precalculated using the Qutip package [92]. For our experiment, we used parameters extracted from precalibration while varying the mean coherent or thermal distribution of the Fock states, truncating calculations at Fock state 150. Given our Lamb-Dicke parameter, we observe that the spin population remains sensitive to mean coherent and thermal distributions up to $\bar{n} \approx 20$ with high confidence. For coherent states, we see multiple revivals in spin probability at higher motional states; to avoid ambiguity in the analysis, we limit the method to lower motional state detection. Despite its non-linear behavior, this method can distinguish different types of motional population dynamics. However, for cases with multiple motion modes (e.g., up to three for a single trapped ion) and estimating their thermal distributions, this method is less effective because of limited information on the distinct thermal dynamics (e.g. differences in heating rates) of each motional mode.

We demonstrate the method using a single ion at the T_2 site, initialized in both coherent and thermal states, as shown in Fig. 31. For simplicity, we initialize the control potential configuration Φ_c, with an effective $\eta_1 \approx 0.2$ for the lowest motional mode ω_1, using a pair of Raman beams (B_3 and R_2), where the other two modes are orthogonal to the Raman beam configuration (η_2 and $\eta_3 \approx 0$). Figure 31a illustrates the experimental sequence for coherent states. Starting with a single trapped ion initialized at the T_2 site near the thermal limit, we cool the addressed mode $\omega_1/2\pi \approx 3.35\,\text{MHz}$ close to the ground state using the resolved sideband cooling method. For different amplitudes U_{exc}, as a function of coherent excitation frequency ω_{exc}, we apply a rectangular oscillating pulse from one of the embedded electrodes (electrode 28 for ω_1, at T_2), using a single channel of an AWG for a fixed duration of $\text{t}_{exc} \approx 10\,\mu\text{s}$. This is followed by spin-motion coupling at the carrier transition and fluorescence collection. Figure 31b shows the experimental data. We analyze the histograms and plot the relative spin state probability $\Delta\,\text{P}_{\downarrow}$ (left axis), referencing the precalibration spin-motion trace. For coherent states, we estimate the corre-

sponding motional state population (right axis) based on acquired spin probabilities. Using a Sinc model fit on two curves corresponding to excitation amplitudes U_{exc} of 1 and 1.5 V, we extract the amplitudes of Fourier-limited resonances as $\bar{n} = 7(1)$ and $15(1)$ quanta, respectively. Figure 31c shows experimental sequences similar to those in a), with the third sequence modified to initiate thermal states through environmental interaction for a variable duration t_{wait}. Figure 31d displays the experimental data, with the analyzed spin probabilities $\Delta\,\mathrm{P}_{\downarrow}$ (left axis) and the mean motional population $\bar{n}$, considering the thermal distribution. As a function of the interaction duration up to 5 ms, we observe an increase in $\bar{n} \approx 7$. A linear model fit yields an estimated heating rate for the motional mode of $\dot{\bar{n}} \approx 1.2\,\text{quanta/ms}$.

In conclusion, our method efficiently detects motional population dynamics in the transient regime, which are otherwise challenging to access with established methods. Additionally, we can apply this method to displaced thermal states, provided that precalibration is done for a Doppler-cooled ion ($\bar{n} \approx 5$, for $\omega_i/2\pi \approx 4\,\text{MHz}$). In most other experiments, we used this method to spectrally resolve the motional mode and track relative changes in motional population.

3.2.2 Intra-Site Coupling

In this work, we implement a method to couple multiple modes at a single site of the triangular matrix by oscillating potentials [50, 51, 98, 101, 102]. This technique has previously been implemented in linear traps; here, we extend it to a triangular trap ion array, where the geometry provides unique advantages for coupling modes at individual sites. As illustrated in Fig. 32, a parametric drive at the difference frequency $\omega_{ij} \approx \omega_i - \omega_j$ of the normal modes, also considering avoided crossings $2\sqrt{g^2 + 4\Delta^2}$ [50], where Δ is the detuning, enables the coupling of two orthogonal modes of a single ion or multiple ions at a single site. With an oscillating potential $U_{ij} = U_{\text{mod}} \cos(\omega_{ij} t + \phi)$, we apply a Taylor expansion around a small displacement r from the origin, leading to Eq. 3.27. In this context, we assume that the curvature term H_{xy}, which depends on both directions of the orthogonal motional modes (say x and y) and dominates the coupling dynamics, is the primary factor, while other terms are neglected. To maintain selective coupling and avoid unwanted coherent excitation or parametric amplification, we ensure that the following condition is satisfied:

$$\omega_{ij} \neq n\omega_{\text{k}}, \quad \forall\, n \in \mathbb{N},\, k \in \{1, 2, 3\}.$$

This condition prevents resonances with integer multiples of other mode frequencies [103, 104].

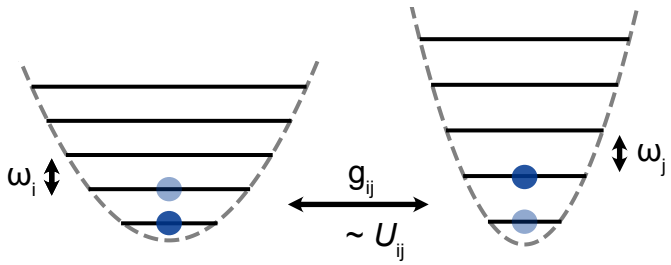

Figure 32: Two-mode coupling. Coupling of multiple motional modes at a single trapping site is achieved using an oscillating potential U_{mod}, driven at the frequency difference $\omega_{ij} \approx \omega_j - \omega_i$ between modes. The coupling rate g_{ij} is tunable via both the amplitude U_{12} of the potential and the frequencies of the two modes, ω_i and ω_j. When the phase of the interaction $\omega_{ij} t_{\text{mod}}$ reaches π, the coupling enables coherent transfer of phonons from one mode to another, known as the *swap* operation. At a phase of $\omega_{ij} t_{\text{mod}} = \pi/2$, the coupling results in two-mode entanglement, analogous to a beam splitter (BS) operation in photonic platforms.

$$\alpha = \left.\frac{\partial^2 U_{ij}}{\partial i \partial j}\right|_{r=r_0}, \quad \text{where } i \neq j \text{ and } i, j \in \{1, 2, 3\} \tag{3.27}$$

$$g_{ij} = \frac{Q_n \alpha}{4M\sqrt{\omega_i \omega_j}} \xi^{(i)} \xi^{(j)} \tag{3.28}$$

$$H_p = \hbar g_{ij} \left(e^{i\phi} \hat{a}_i^\dagger \hat{a}_j + e^{-i\phi} \hat{a}_i \hat{a}_j^\dagger \right) \tag{3.29}$$

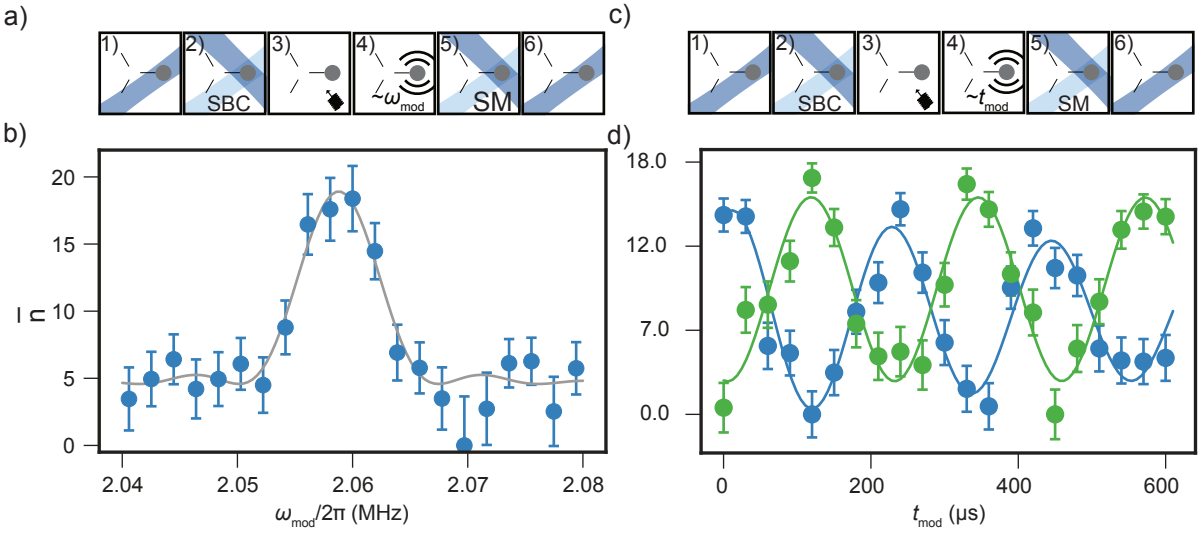

Figure 33: Intra-site coherent coupling of two orthogonal in-plane motional modes. Panels (a) and (c) depict the experimental sequences. (a) 1) A single trapped ion is initialized at the thermal limit at the T_2 site. 2) Two in-plane modes, ω_1 and ω_2, are cooled near the ground state using two corresponding Raman beam configurations. 3) A coherent state of approximately 20 quanta is generated in one of the normal modes, ω_1, using a control electrode, say electrode 28 (see Fig. 1). 4) Modulation with a fixed amplitude $U_{\text{mod}} = 2\,\text{V}$is applied as a function of frequency ω_{mod}, via electrode 24 or 28. 5) Spin-motion coupling is performed with corresponding Raman beams at the carrier frequency ω_{qubit}. 6) Fluorescence is collected with a PMT for motional population analysis. Panel (b) shows the exchange as a function of ω_{12} at a fixed modulation amplitude of $U_{\text{mod}} = 2\,\text{V}$. Using a Sinc model fit, we resolve the coupled resonance at $\omega_{12}/2\pi = 2.059(1)\,\text{MHz}$. Panel (c) follows a similar sequence to (a), but with the coupling duration t_{mod} as the scan variable at a fixed, calibrated frequency ω_{12}. Panel (d) shows coherent exchange between the two modes as a function of modulation duration t_{mod} for fixed U_{mod} and ω_{12}, resulting in a coupling rate $g_{12}/2\pi \approx 4.5\,\text{kHz}$, extracted using a sinusoidal fit.

As shown in Eq. 3.28, the coupling rate g_{ij} depends on various factors, such as modulation amplitude U_{mod}, motional mode frequencies (ω_i, ω_j), charge Q, ion mass M and normalized participation of modes $\xi^{(i)}\xi^{(j)}$ of a single ion at a single site. With the resulting interaction, the Hamiltonian in Eq. 3.29, and controllable parameters such as the coupling rate g_{ij} and duration/phase, we can tailor the interaction to achieve a coherent transfer of the motional state population between two chosen orthogonal modes. For example, starting with an initial motional state of $|0\rangle_i |1\rangle_j$, we can initiate the interaction for a duration t_π, equivalent to a phase of $\phi = \frac{\pi}{2}$. This results in an evolution to the state $|1\rangle_i |0\rangle_j$. At time $t_{\pi/2}$, equivalent to $\phi = \frac{\pi}{4}$, the state evolves

to $\frac{1}{\sqrt{2}}\left(|1\rangle_i|0\rangle_j + |0\rangle_i|1\rangle_j\right)$. We infer that these interactions are analogous to Hong-Ou-Mandel interference [101] in photonic platforms and apply to any bosonic system. Additionally, with arbitrary initial states $|\mathrm{N}\rangle_i|\mathrm{N}\rangle_j$, we can engineer NOON states such as $\frac{1}{\sqrt{2}}\left(|\mathrm{N}\rangle_i|0\rangle_j + |0\rangle_i|\mathrm{N}\rangle_j\right)$ for metrology applications and generate a two-mode entanglement with an appropriate choice of parameters.

We choose the T_2 trapping site for a proof-of-principle demonstration with a Mg^+ ion initialized at the thermal limit (at least in the two in-plane motional modes). With two in-plane modes, $\omega_1/2\pi \approx 3.7\,\mathrm{MHz}$ and $\omega_2/2\pi \approx 5.8\,\mathrm{MHz}$, we employ dedicated Raman beams configured for the appropriate geometry, resulting in Lamb-Dicke parameters of $\eta_1 \approx 0.2$ and $\eta_2 \approx 0$ with beams B_3 and R_2, and $\eta_2 \approx 0.1$ and $\eta_1 \approx 0$ with beams B_1 and R_2. Decoherence due to off-resonant scattering from beam R_2 is approximately 100 times lower than that from all other operations, ensuring minimal impact on spin-motion coupling. Figure 33a illustrates the experimental sequence used to spectrally resolve and calibrate the difference drive frequency ω_{12} for modulation. With the two modes cooled near the ground state, we create a coherent state with $\bar{\mathrm{n}} \leq 20$ using a laser-less method involving embedded control electrodes (see Fig. 1): electrode 28 for ω_1 and electrode 25 for ω_2. This is followed by an oscillating drive with $U_{\mathrm{mod}} = 2\,\mathrm{V}$, applied via electrode 24 or 27 for ω_{12} modulation and electrode 25 for ω_{13} modulation, as a function of ω_{mod} for a fixed duration $t_{12} = 100\,\mu\mathrm{s}$, leading to an exchange of motional state population between the two modes. We then perform spin-motion coupling at the carrier frequency ω_{qubit}, followed by fluorescence detection with a near-resonant Doppler beam. Using the carrier method, we plot the mapped mean motional population, as shown in Fig. 33b. With a Sinc model fit, we resolve the Fourier-limited resonance frequency at $\omega_{12}/2\pi = 2.059(1)\,\mathrm{MHz}$. Figure 33c shows a similar sequence to (a), but with t_{mod} as the scan variable. The oscillation drive is executed at a fixed ω_{12} as a function of modulation time t_{mod}. With dedicated spin-motion coupling on both modes (green and blue disks), we track the coherent exchange of motional population between the two modes, plotted in Fig. 33d. With a sinusoidal model fit, we extract the coupling rate $g_{12}/2\pi \approx 4.5\,\mathrm{kHz}$. We highlight suitable operational points, with the Beam-Splitter (BS) operation at $t_{12} = 55\,\mu\mathrm{s}$ and the *swap* operation at $t_{12} = 110\,\mu\mathrm{s}$. For calibration of ω_{12} and t_{12}, we suggest that mapping to motional population is unnecessary and easily resolvable in the spin probability basis. We observe coherent transfer of motional population from one mode to another at the *swap* duration, enabled by the negligible η_2 of the spectator mode ω_2 with beam configuration B_3 + R_2, and vice versa. By defining both modes as detectors, we can perform two BS operations, separated temporally in a Ramsey-like sequence, with a tunable relative phase $\Delta\phi$, to verify two-mode entanglement and the bosonic behavior of the motional population (phonons).

In Fig. 34, we demonstrate the dependence of the coupling rate g_{12} on the modulation amplitude U_{mod}. Panel (a) illustrates an experimental sequence similar to Fig. 33, with a single ion initial-

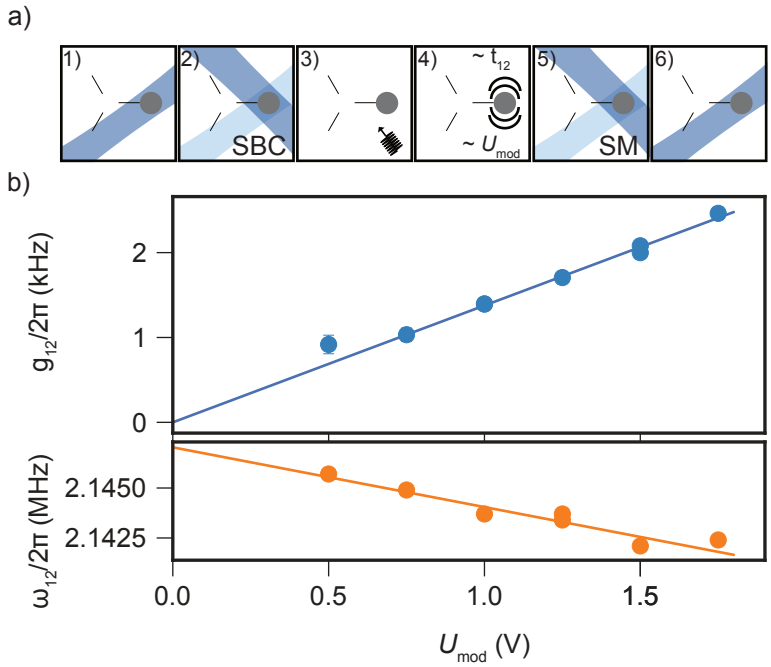

Figure 34: Tuning the coupling rate g_{12} with modulation amplitude $U_{\mathbf{mod}}$. (a) shows the experimental sequence, similar to the experiment in Fig. 33. 1) A single trapped ion is initialized at the thermal limit at trapping site T_2. 2) The two in-plane normal modes are cooled near the ground state using dedicated Raman beam configurations. 3) Coherent excitation is applied to produce a mean motional population of $\bar{n} \approx 20$ at ω_1. 4) Using dedicated calibration sequences, the resonance frequency ω_{12} and coupling rate g_{12} are determined for varied U_{mod}, with scan variables ω_{12} and t_{12}. 5) Spin-motion coupling is performed with the corresponding Raman beams. 6) Photons are collected for motional population analysis. (b) shows the extracted parameters, including the coupling rate g_{12} and the shift in resonance frequency ω_{12}. From linear model fits, we obtain $g_{12}/U_{\mathrm{mod}} = 2\pi \times 1.38(1)$ kHz/V and an avoided crossing shift of $-2\pi \times 1.49(1)$ kHz/V, with probable detuning Δ and higher-order contributions on the order of $\approx 2\pi \times 110$ Hz.

ized at T_2, resolution of motional modes ($\omega_1/2\pi = 3.726(1)$ MHz and $\omega_2/2\pi = 5.885(1)$ MHz), and the ability to scan two variables: U_{mod} and t_{12}. For each U_{mod}, measurements are taken to resolve the coupling frequency ω_{12} for a fixed t_{12}. Using these extracted parameters, a second measurement is performed with t_{mod} as the scan variable to determine the coupling rates g_{12}. Panel (b) presents the extracted coupling rates and coupled resonances as functions of U_{mod}. From linear fits to the data, we estimate $g_{12}/U_{\text{mod}}/2\pi = 1.38(1)$ kHz/V and a change in modulation frequency $\omega_{12}/2\pi = -1.49(1)$ kHz/V attributed to avoided crossings and additional contributions. From these measurements, we estimate the uncoupled difference frequency to be $\omega_{12}/2\pi = 2.147(1)$ MHz. The observed 110 Hz shift between the coupling rate and modulation frequency shift could arise from higher-order couplings, such as cross-Kerr effects [105, 106] due to anharmonic trap potentials, and off-resonant interactions caused by dropped terms in Eq. 3.27. Alternatively, the relationship between detuning information and avoided crossings can be further explored by resolving additional features in the two-photon spectrum during continuous modulation at the difference frequency $\omega_{12} \pm \Delta$.

In conclusion, we achieve coupling rates up to $g_{12}/2\pi \approx 10$ kHz by adjusting the modulation amplitude, although this is limited by voltage constraints. Shaping the modulation pulse to ensure an adiabatic change, rather than using a rectangular pulse, could help avoid unnecessary excitations [50, 51]. Additionally, by tuning motional mode parameters, such as mode frequencies and orientations, we can adjust the coupling strength. Ideally, we would modulate the curvature control potential vector H_{xy} (off-diagonal component of the Hessian matrix 3.2), where x and y correspond to the modes at the difference frequency, for efficient coupling while also ensuring a near-zero electric field to minimize additional effects leading to dephasing. However, because of current technical limitations in operating a group of electrodes to drive oscillating potentials with fixed phase relations, we chose to operate a single electrode with the most significant contribution to the curvature term. At higher potentials, this results in additional fields that cause dephasing in coherent exchange.

3.2.3 Multi-Site Control: Automated Loading

In larger arrays with multiple trapping sites, achieving deterministic loading within shorter timescales becomes crucial to reduce operational overhead and improve experimental efficiency. In previous work, regardless of whether the architecture involved the triangular array (Fig. 1) or the linear trap (Fig. 2), ions were typically loaded using a magnesium oven by resistive heating. Magnesium atoms were released through a slit (in the case of a linear trap) or a loading hole (in a triangular array) before being ionized. This process often takes up to a few minutes, especially for multiple ions, significantly increasing background gas pressures. The prolonged exposure to high-power ultraviolet (UV) beams near various in-vacuum components, such as electrodes, also leads to the generation of stray fields. These stray fields must be compensated for after ion loading, which further increases the operational overhead. Additionally, an increase in background gas pressure raises the likelihood of residual gas collisions, leading to ion loss from the trap, reducing ion storage durations and operational efficiency.

We introduce ablation loading [107, 108] using an infrared pulsed laser [2] operating at a wavelength of approximately 1030 nm and a repetition rate of 1.5 kHz. A magnesium wire, composed of 80% ^{24}Mg, 10% ^{25}Mg, and 10% ^{26}Mg, is wound around a pillar of the chipholder, as shown in Fig. 4, positioned approximately 10 mm from the trapping region [109]. The ablation laser is focused using a 150 mm lens mounted on a translation stage, producing a beam diameter of approximately $40\,\mu$m, ten times smaller than the diameter of the target wire of 0.4 mm. The preliminary tests by Nitzsche et al. [109] (2018) employed a 532 nm pulsed laser, which was later replaced by a 1030 nm laser for deeper absorption and increased volumetric heating [110, 111].

We employ an ancillary site, approximately $10\,\mu$m above the triangular array, for ion loading; this site is referred to as the hub throughout this thesis. During the trapping procedure, we use the control potential configuration, Φ_{HL}, optimized to provide a larger trapping volume with shallower confinement for efficient loading. While the Doppler beams remain active, the ablation and photo-ionization lasers are triggered for a brief duration of 10 ms, significantly reducing loading times compared to earlier methods that required several minutes. A pulse train consisting of 5–10 individual pulses, each with an energy of approximately $30\,\mu$J, and a pulse width of approximately 1 ns, is directed at the magnesium wire to release energetic atoms. These atoms are ionized via a two-photon process involving the photo-ionization laser and Doppler cooling beams, after which they are trapped at the hub site.

We optimize the pathways of the photo-ionization and ablation beams to establish a configu-

[2] Integrated Optics: Matchbox, pulsed IR laser, Part Number: 1030L-11C-NI-NT-NF

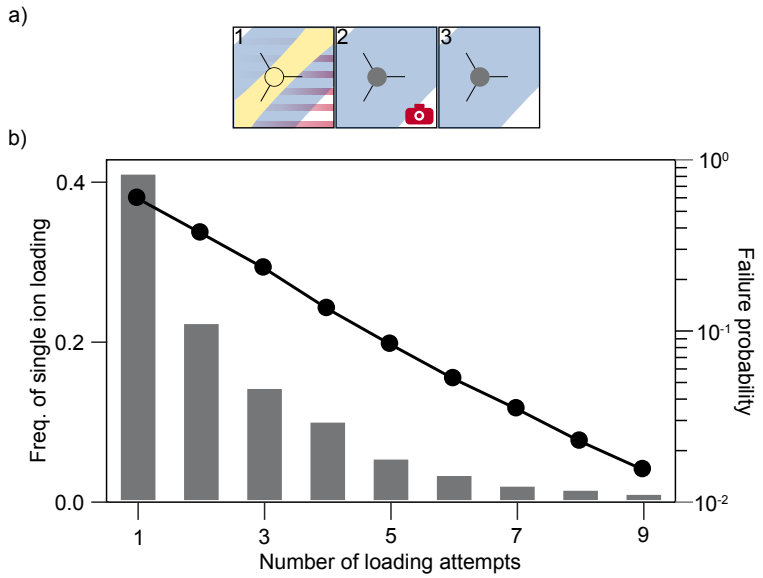

Figure 35: Automated loading statistics collected over 180 days. Adapted from our publication [49]. (a) illustrates the protocol for automated ion loading: (1) While the Doppler cooling lasers remain active, the photo-ionization and ablation lasers are initialized. Five to ten laser pulses, each with an energy of approximately 30 µJ, are directed at the magnesium wire, which is wound approximately 10 mm from the trap. Focusing optics ensure that the ablation laser beam remains smaller than the wire diameter and remains focused on the wire. (2) The EMCCD camera captures an image to confirm the presence of ions. (3) If ions are successfully trapped, they are prepared for subsequent experiments; otherwise, the protocol is repeated. Each repetition takes approximately 1.2 seconds. After 10 consecutive failed attempts, the automated loading process is paused for inspection. Manual optimization of the trapping laser alignment is performed no more than once per week. Overall, single-ion trapping is achieved within 6 seconds in more than 90% of attempts, with a success rate exceeding 40% on the first attempt.

ration that ensures deterministic loading of a single ion in the hub for each trapping attempt. Figure 35 presents statistics collected over 180 days using an automated loading routine interfaced with a database (see Sec. 2.3). During this period, we achieved a 40% success rate for single-loading attempts and a 90% success rate for trapping a single ion in six seconds. Notably, the pathways, power, and focal points of the ablation laser remained stable and did not require further optimization for nearly two years, demonstrating the robustness of the setup. Trapping failures were primarily caused by malfunctions in lasers or electronics, which were addressed through regular weekly maintenance as needed.The overall fluence and temperature of the atom ensemble are determined by the ablation pulse parameters. Although a higher pulse energy directly increases fluence, shorter individual pulses result in a hotter atom ensemble, which reduces the probability of successful trapping [112]. Since individual pulse widths cannot be adjusted, we tune the overall power and number of pulses to effectively balance fluence and trapping probability.

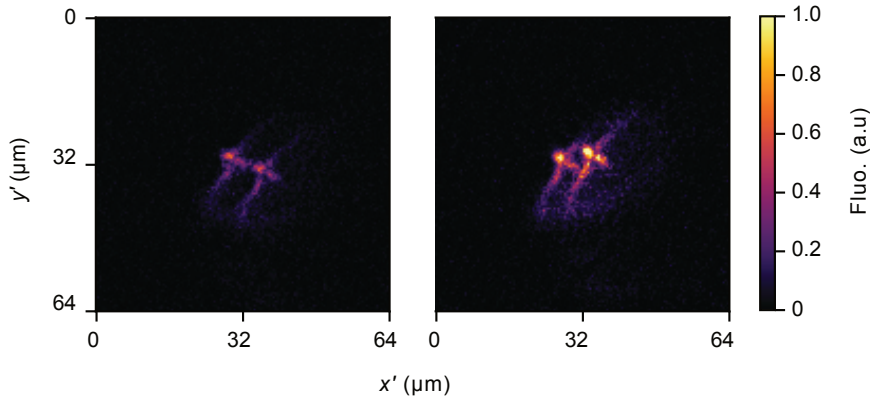

Figure 36: Control of the hub site via electric fields and curvature. This figure shows two images of ions at the hub site (T_H), each captured under a different control potential configuration with distinct in-plane curvatures: H_{xy} values of $0\,\mathrm{V/mm/100\,\mu m}$ and $0.5\,\mathrm{V/mm/100\,\mu m}$. These configurations result in a shift of the in-plane angle by approximately 20 degrees. Due to the tilt in the imaging optical pathway (see Fig. 13), the coordinates (x', y') are transformed, altering the perspective of the images.

In the triangular array, individual control of the eight degrees of freedom at each trapping site is a primary requirement. Therefore, the hub and three lower sites require a total of 32 electrodes (8 degrees × 4 sites) for ideal control, assuming harmonic confinement. However, the set-up currently includes only 30 electrodes. Using existing optimization methods [75], it was not possible to calculate fields and curvatures with minimal crosstalk between all trapping sites. Our approach to reducing crosstalk has limitations as the electrodes are positioned closer to the three lower sites than to the hub. Consequently, the control potential configuration (Φ_H) (see Appendix A) is calculated specifically for the hub site, independently of the other sites, to ensure effective control despite these challenges. As shown in Fig. 36, control over the fields and curvatures at the hub is demonstrated, with two ions aligned along the axis of weakest

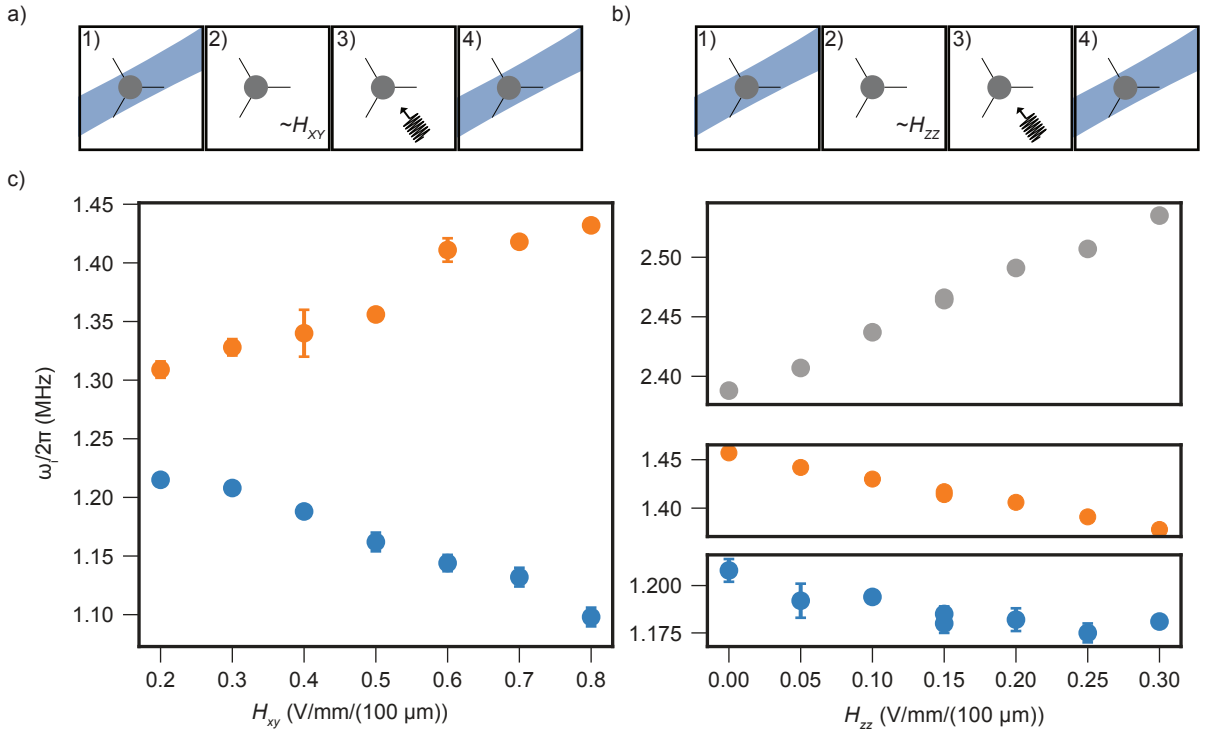

Figure 37: Control of the hub site with electric fields and curvatures. (a) and (b) illustrate experimental sequences. (a) 1) An ion is initialized at the hub site at the thermal limit. 2) The in-plane curvature H_{xy} is adjusted within a range of 0.2–$0.8\,\mathrm{V/mm/100\,\mu m}$. 3) The motional mode is excited, and the mode frequency is scanned to resolve both in-plane modes. 4) Fluorescence is recorded using a near-resonant Doppler beam for detection. Sequence (b) is similar to (a) but uses H_{zz} as the tuning variable instead of H_{xy}. (c) shows experimental data for the two in-plane modes as functions of curvature along the xy axis, with both modes tuned over 100 kHz. In the data on the right, the curvature along the zz axis is tuned, and the out-of-plane mode, which overlaps significantly with the detection beam, is observed. A radial deconfinement of approximately 5 kHz is identified. Across the entire tunable range, the overall change in confinement in all directions is negligible due to residual electric field changes.

confinement ($\omega_1/2\pi \approx 1.2$ MHz). This demonstration illustrates the control of the curvature H_{xy}, enabling precise tuning of the frequencies and orientations of the motional modes at the hub. The orientation of the motional modes can be adjusted by up to 20° as a function of H_{xy}, tuned by $\approx 0.5\,\mathrm{V/mm/100\ \mu m}$.

In conclusion, control over the hub site and the orientation of the mode vector is achieved. To enable multidimensional coupling via dipole-dipole interactions, the mode frequencies at the hub must be tuned with sufficient precision (within $\pm 5\%$) to match those of the ions at the three lower sites. Figure 37 shows the measured mode frequencies for all three modes as a function of the curvature along the xy and zz axes. Coherent excitation at trap frequencies, driven through dedicated control electrodes and followed by fluorescence detection in the weak-binding regime, reveals that both radial mode frequencies can be tuned up to $\omega_{1,2}/2\pi \approx 100\,\mathrm{kHz}$ as a function of H_{xy}, while the vertical mode is tuned approximately by $\omega_3/2\pi \approx 150\,\mathrm{kHz}$ as a function of H_{zz}. Residual displacement and deconfinement in other directions (for example, x and y) result in changes to the in-plane modes of approximately $\omega_{1,2}/2\pi \approx 25$–$50\,\mathrm{kHz}$. The general trace, defined as the sum of all on-diagonal elements $\sum_{i\in\{x,y,z\}}(\omega_i/2\pi)^2$ of the Hessian matrix (Eq. 3.2), remains consistent within $0.5\,\mathrm{MHz}^2$, demonstrating negligible positional changes due to residual electric fields throughout the tunable curvature range. Further details on the hub's properties compared to the lower-lying sites are provided in the supplementary material of [49].

3.2.4 Inter-Site Transport

In the triangular array, initializing one or more ions at specific trapping sites is a primary requirement to perform complex multiple-ion experiments. In previous work, techniques for ion initialization at designated sites were achieved by positioning the loading beams at the desired trapping sites for extended periods, combined with the repositioning of ions through probabilistic methods that were not deterministic. In this work, with the calibrated hub site situated at an elevated position of approximately $10\,\mu$m above the triangular array, we utilize it both as a storage site and as an intermediate site to allow deterministic transport across all sites that span the three-dimensional landscape (see Fig. 18). By implementing this method, we establish a robust and scalable tool for precise multi-ion initialization in a trapped-ion array platform.

In previously reported shuttling or transport experiments [26, 27, 113, 114], ion transport is primarily governed by DC fields that guide ions along well-defined one-dimensional pathways. Temporary confinement is established along the transport axis by minimizing the gradient or maintaining it near zero in the direction of motion. This confinement is dependent on time and position and is achieved through the precise control of potentials, allowing the transport of single or multiple ions along the pathway [114–116]. These techniques form the foundation for the implementation of the QCCD architecture. However, deviations or irregularities in the gradient along the transport path have been shown to induce heating in the motional modes of trapped ions [117].

In the triangular array, the multiple trapping sites, which are inherent to the pseudopotential landscape generated by the radio frequency (RF) drive (see Sec. 2.2.2), remain approximately constant on average over time. To transport a single trapped ion from an initial RF-confined site to a target RF-confined site, conditions must be created to overcome the pseudopotential barrier of $\leq 4\,$meV. This can be achieved by temporarily forming transport pathways or by adjusting the control potentials. With 30 control electrodes and the AWG capable of generating and playing back waveforms on demand and in real time, we actively switch between different control potential configurations (see Appendix A), Φ_c (e.g., transitioning from an initial configuration Φ_i to a final configuration Φ_t), to enable deterministic ion transport.

During the transition between two waveforms, the potentials applied to individual electrodes are ramped linearly in discrete finite steps (see Sec. 2.2.2) to reach the target configuration Φ_t. Although current control electronics can achieve slew rates on the order of several hundred volts per microsecond, the single-stage passive filtering components on the control electrodes attenuate high-frequency signals, with a cutoff frequency $f_c/2\pi \approx 10$ kHz, thus limiting rapid changes in electrode potentials. Furthermore, the over-voltage protection (OVP) of the trap [55]

enforces a maximum voltage limit of 10 V. This balance between the waveform execution rate and the admittance of technical noise imposes constraints on the operational parameters. Consequently, the execution durations of the waveform are chosen within the range of 0.1 to 1 ms, with potential changes restricted to between 0.1 and 5 V.

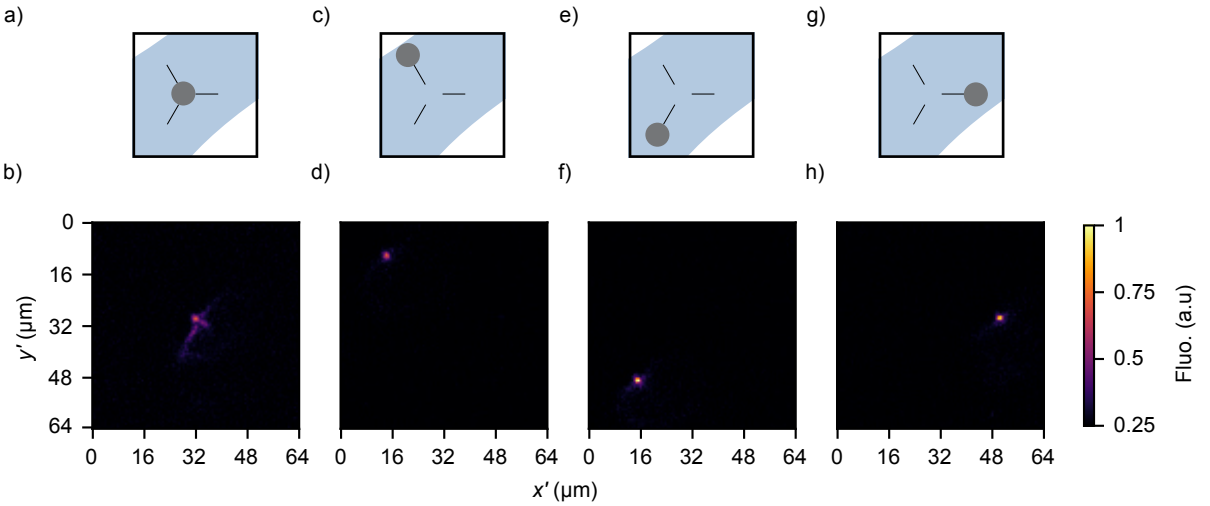

Figure 38: Preparation of deterministic single-ion transport. (a) and (b) show the control potential configuration $\Phi_c = \Phi_H$ and the corresponding fluorescence image of an ion at the hub site. (c) and (d) represent the repositioning of a single ion from the hub site to the T_0 site by switching Φ_c from Φ_H to Φ_0 within a playback time of 0.1–1 ms. Similarly, (e) and (f) represent the T_1 site and the corresponding fluorescence image of a single ion transported from T_H, and (g) and (h) represent the T_2 site with an ion transported from T_H. All control potential configurations are tabulated in the appendix. A.

We demonstrate the transport of a single ion across the pseudopotential landscape interconnecting the lower-lying triangular array and the hub site in real-time, compared to the pseudopotential approximation. Together, these sites form a pyramidal configuration, as illustrated in Fig. 38. To achieve deterministic transport, we introduce a coarsely tuned protocol that leverages assisted cooling from Doppler beams. For a transport event between two trapping sites (for example, T_H and T_2), we switch between the control potential configurations Φ_H and Φ_2 within a waveform playback duration t_{playback} of 0.1–1 ms, limited by filtering components. This process is performed in the presence of Doppler beams to mitigate motional excitation during transport, while ensuring that the total potential difference between the configurations remains $\leq 5\,\text{V}$. To resolve single ions at different trapping sites, we use imaging optics (see Fig. 13) with a magnification of 40x, a resolution of $0.32\,\mu\text{m/pixel}$, and an exposure time of 0.5 s. Similarly, the control potential configurations Φ_0 and Φ_1 are determined for the trapping sites T_0 and T_1, respectively, which allow transport to and from the hub site (T_H). To characterize the magnetic-field gradient within the set-up, we use the most magnetic-field-sensitive hyperfine transition ($F = 3, m_F = +3$ and $F = 2, m_F = +2$), labeled $|{\downarrow}\rangle$ and $|{\uparrow}\rangle$ (see Fig. 6). The shift in transition frequency across different trapping sites is measured using the experimental sequence shown

in Fig. 19. Taking into account the field sensitivity of approximately $-2\pi \times 21.76\,\mathrm{MHz/mT}$, we derive the magnetic field gradient relative to the hub site. As summarized in Tab. 5, the magnetic field gradient is determined to be $12(1)\,\mathrm{nT/\mu m}$.

Site	$\omega_{\text{qubit}}\ \lvert\downarrow\rangle - \lvert\uparrow\rangle$ (MHz)	Rel. Distance (μm)	Gradient (nT/μm)	Slew Rate (V/ms)
T_H	1541.070(1)	0	-	-
T_0	1541.0633(1)	≈ 25	≈ 12	<4
T_1	1541.064(2)	≈ 25	≈ 11	<3
T_2	1541.0628(2)	≈ 25	≈ 13	<3

Table 5: Magnetic field gradients and slew rates for the trapping sites, with respect to T_H site.

To utilize single-ion transport for initializing or preserving quantum states, ions must be transported in the absence of fields, such as Doppler lasers, to avoid coherence loss. Additionally, improving transport fidelity requires the execution of waveforms with minimal durations and low slew rates. Along with compensating for daily variations in stray fields, we tune individual control potential configurations to determine the minimal potential change required to enable high-fidelity ion transport between an initial site and a final site. For example, with fine-tuned configurations for shuttling ions between T_H and T_1, the minimum required change in potential is $|\Phi_H - \Phi_1| \leq 0.3\,\mathrm{V}$. Similarly, the control potential configurations Φ_0 and Φ_1 are tuned for T_0 and T_2, respectively. These control potential configurations for all four sites are summarized in the appendix A. With a minimal waveform execution duration $t_{\text{playback}} \approx 0.1\,\mathrm{ms}$, we transport single ions between T_H and other sites with slew rates $\leq 4\,\mathrm{V/ms}$, as shown in Fig. 38 and tabulated in Tab. 5. The transport execution speed of $0.25\,\mathrm{m/s}$ is three orders of magnitude lower than the velocities associated with motional mode frequencies, ensuring adiabatic transport conditions. For intraregional transport, such as from T_1 to T_{1a} (see Fig. 15), the absolute potential change required is $|\Phi_1 - \Phi_{1a}| \leq 0.2\,\mathrm{V}$.

Figure 39 presents an experimental demonstration of transport using the fine-tuned method, characterized by minimal slew rates and optimized waveform durations. This approach highlights the ability to adiabatically transport ions without requiring assistance from Doppler cooling. Figure 39a illustrates the transport sequence between T_H and T_1 with a single trapped ion. In both directions, reversible transport is performed between the two sites, followed by fluorescence detection. To avoid false positives, we position the detection beam (BDx) and use mean photon counts to create three distinguishable conditions. When the BDx beam is aligned with T_1, we observe a photon count of approximately $\bar{N} \approx 6$ during a duration of fluorescence collection of $200\,\mu\mathrm{s}$. For an ion stationary at T_H, we measure $\bar{N} \approx 2$, corresponding to a cross-talk of about 30%. The loss of ions is identified by $\bar{N} \approx 0.4$. Figure 39b shows fluorescence histograms collected over 100,000 repetitions, with ions initialized with Doppler cooling before each repetition. Reference measurements were performed with stationary ions at the corresponding

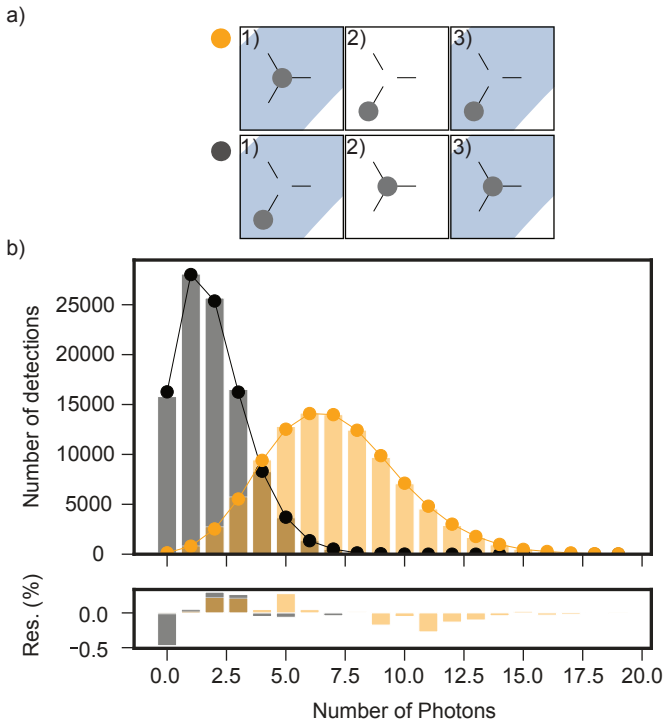

Figure 39: Transport of a single ion over 100,000 times. (a) illustrates two experimental sequences. Transport from T_H to T_1 (yellow): 1) A single trapped ion is initialized at T_H with control potential configuration Φ_H. 2) The ion is transported to T_1 in the absence of fields that cause decoherence of electronic degrees of freedom, such as Doppler lasers, by switching to the fine-tuned control potential configuration Φ_1. 3) Fluorescence is collected with a PMT. Similarly, transport from T_1 to T_H (gray) is performed by switching from Φ_1 to Φ_H. The detection beam is positioned to produce three distinguishable results, with mean photon counts of $\bar{N} = 0.4$, 2, and 6, corresponding to ion loss, the ion at T_H (gray), and the ion at T_1 (yellow), respectively. (b) shows histograms of fluorescence collected over 100,000 consecutive transports. The two distinct histograms (gray and yellow) highlight the successful execution of 100,000 transports between the initial and final sites, with minimal impact on the motional degrees of freedom. The residual plot shows approximately 2% reduction in fluorescence compared to a reference measurement taken with stationary ions. This protocol is used to estimate motional mode heating as given in Eq. 3.26.

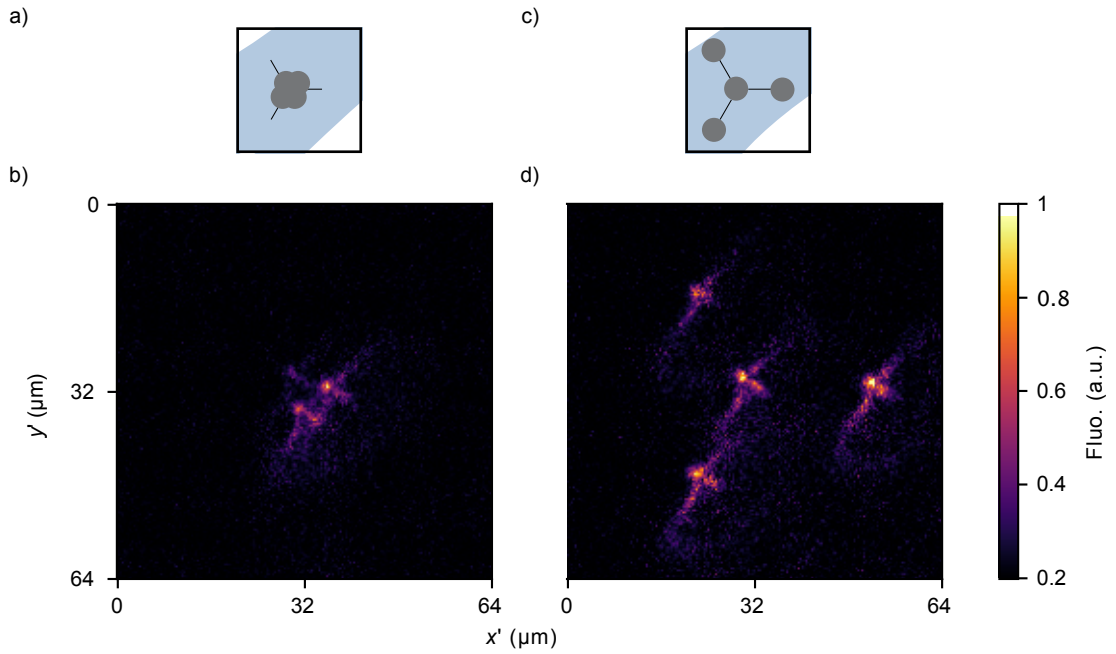

Figure 40: Preparation of ions at all four sites. (a) The control potential configuration Φ_{HL} used for loading ions at the hub site. (b) The corresponding fluorescence image showing four ions loaded at the hub site, acquired after repeated loading attempts (typically $N_{\mathrm{attempts}} \leq 10$) until the desired number of ions is achieved. (c) The target control potential configuration Φ_{pyramid}, optimized to create transport channels for redistributing and storing ions at all four sites, including the hub. (d) The corresponding fluorescence image showing each site occupied by a single Mg ion, achieving the initialization of a 2D+ pyramidal configuration.

sites. Compared to the reference histograms, we observe an overall reduction in fluorescence of approximately 2%. Using this protocol, we demonstrate single-ion transport from T_H to any triangular site more than 100,000 times, with limitations arising only from background ion loss due to residual gas collisions.

In conclusion, we demonstrate deterministic redistribution protocols for multiple ions from a single site to multiple sites, leveraging mutual Coulomb repulsion (inter-site Coulomb blockade) with efficiencies exceeding 50%. Figure 40 illustrates the redistribution of four ions from T_H to T_0, T_1, and T_2 using an adiabatic waveform transition from Φ_{HL} to $\Phi_{pyramid}$, with an overall potential difference of 2 V. Despite the presence of considerable cross-talk between sites, ion storage is ensured by iteratively tuning the electric fields calculated for the hub site to achieve stable trapping conditions. Furthermore, we demonstrate the ability to trap multiple ions and redistribute or reorder them to achieve the desired trapping configuration within a few seconds, representing a significant improvement over the several minutes required by conventional methods.

3.2.5 Motional Heating: Identifying Noise Mechanisms

In this subsection, we discuss potential noise sources that contribute to motional decoherence. These sources are broadly classified into two categories: technical noise and anomalous noise. Following the terminology used by Sedlaeck et al. [118], technical noise refers to well-understood noise mechanisms originating from active and passive components near the ion. Examples include noise from Radio-Frequency peripherals, control electrodes, and stray photons from insufficiently isolated laser sources. In contrast, anomalous noise, as described by Turchette et al. [119], refers to less well-understood mechanisms, predominantly originating from the surface of the chip trap, due to contaminants [120]. Understanding and mitigating these noise sources is critical for reducing motional heating rates, which is a significant challenge in maintaining motional coherence in an ambient-temperature surface trap architectures. In the triangular array platform, lowering the motional heating rate below the inter-site coupling rate is essential to enable and study interactions at the single-quanta level across different trapping sites, forming the basis of a 2D quantum simulation [42, 44, 45].

Experimentally, the heating rate of the motional mode is measured as the rate of excitation resulting from interactions with either injected signals or environmental noise. This rate depends on parameters such as the ion-electrode distance d, motional frequency ω_i, and temperature T, as described by the empirical relation, with their corresponding scaling factors α , β , and γ, given in Eq. 3.30.

$$\dot{\bar{n}} \propto d^{-\alpha}\omega_i^{-\beta}T^{+\gamma} \tag{3.30}$$

The heating rates are expressed in terms of the spectral density of electric field noise $S_{\mathrm{E}}(\omega_i)$, normalized by the motional frequency ω_i and the mass of the trapped ion m, given by Eq. 3.31.

$$\dot{\bar{n}} = \frac{e^2}{4m\hbar\omega_i} S_{\mathrm{E}}(\omega_i) \tag{3.31}$$

Using motional heating rate measurements ($\dot{\bar{n}}$) and the corresponding spectral density of electric field noise ($S_{\mathrm{E}}(\omega_i)$), we quantify the noise mechanisms present in our platform. These results are compared with other surface trap platforms to evaluate relative performance and identify shared or unique noise characteristics.

Technical Noise: Control Electronics

When operating active optical elements such as AOMs (see Fig. 8), we ensure a high extinction ratio of approximately 60 dB using RF switches. However, in practice, the presence of residual photons near the resonant transition impacts the electronic degrees of freedom, as shown in Fig. 25. For motional degrees of freedom, spontaneous transitions induced by residual photons, coupled with an appreciable Lamb-Dicke parameter ($\eta \approx 0.2$), lead to incoherent motional excitations. Using the formalism of Eq. 3.9, we quantify the motional excitations caused by all available beams in the Sec. 4.3.

For technical noise from electronic components related to the trap architecture (shown in Fig. 10), both active and passive, we estimate the electric-field noise near the resonance frequency of the motional mode. In most cases, technical noise can be modeled as thermal noise (Johnson-Nyquist) originating from various components of the lumped circuit [121]. We calculate technical noise with respect to the RF minimum and the distance d from the relevant components. This vicinity is defined in terms of a characteristic distance, $d^{\alpha} = D^{\alpha}_{\text{eff}}$, calculated as the ratio of the noise potential U_{el} to the resulting noise field E_{el} measured at the RF minimum. The characteristic distances of all control electrodes with respect to the T_2 site are provided in the appendix 12. Consequently, the electric field noise resulting from a noise potential at an electrode typically scales by a factor of $\alpha = 2$ [118, 122].

Figure 41 shows two equivalent circuits connected to the RF electrode (oscillating) and the control electrodes (mainly static), along with their active and passive components, derived from the actual setup shown in Fig. 10. Brownnutt et al. [121] provide a detailed description to estimate the equivalent resistance in such circuits to calculate the overall technical noise. In this work, we make conservative noise estimations following these descriptions.

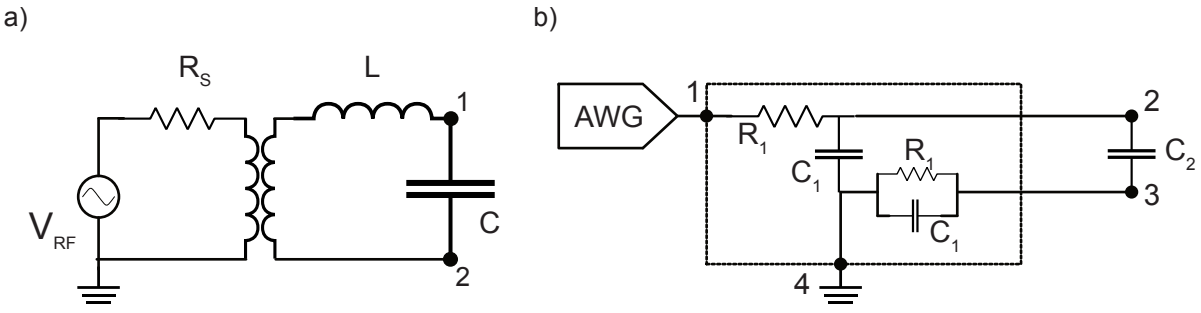

Figure 41: Equivalent circuits describing RF and control electrodes. (a) RF circuit showing resistance R_{s}, inductance L, and capacitance C, representing stray wire resistances, the helical resonator, and the electrode, respectively. In the vicinity of the trapped ion (indicated with terminals 1 and 2), the equivalent series resistance is estimated for thermal noise calculation. (b) Similarly, a typical single channel of a control electrode is shown. Solving for terminals 2 and 3 allows estimation of both thermal and technical noise pickup.

For the RF electrode case shown in Fig. 41a, the definition of D_{eff} depends on minimizing the RF gradient (see Sec. 3.1). In practice, for an applied voltage of $\leq 200\,\text{V}_{\text{zp}}$, the electric field experienced by the trapped ion approaches zero, causing D_{eff} to approach infinity. Blakestad et al. [113] provide an analysis of increased noise due to displacement from the RF minimum, as shown in Eq. 3.32. Using this formalism, we estimate $\dot{\bar{n}}$ caused by ion displacement Δx from the pseudopotential minimum to evaluate S_{V} or determine changes in D_{eff}, accounting for the quadrupole field ($\Phi''_{\text{RF}} = V_{\text{RF}}/D_{\text{eff}}$) and higher-order contributions from micromotion q_x.

$$\dot{\bar{n}}_{\text{RF}} \approx 4\frac{e^2}{4m\hbar\omega_i}\left(\frac{q_x}{4}\right)^2(\Phi''_{\text{RF}})^2 S_{\text{V}}(\Omega_{\text{RF}} \pm \omega_i)\frac{(\Delta x)^2}{V_{\text{RF}}^2} \tag{3.32}$$

For technical noise from active components, the measured level is below -100 dBc, assuming a carrier signal power of 26 dBm, for a characteristic resistance of 50 ohms using the setup shown in Fig. 10, which agrees with the manufacturer's specifications. To estimate thermal noise, we calculate the equivalent series resistance (ESR) for individual components across the two defined terminals (1 and 2) in Fig. 41, using Eq. 3.33. Assuming a quality factor $Q \approx 50$, an RF frequency of $\Omega_{\text{RF}}/2\pi \approx 60\,\text{MHz}$, inductance $L = 1\text{–}10\,\mu\text{H}$, and capacitance $C = 1\text{–}10\,\text{pF}$, we estimate an equivalent resistance of $\leq 20\,\Omega$, assuming low dielectric loss θ, and residual resistance R_{wires}. In practice, we focus on noise near $\pm\omega_i$, leading to an equivalent resistance estimate of approximately $2\,\text{k}\Omega$ with the modified formalism in Eq. 3.34. Based on this resistance, we calculate the electric potential noise spectral density S_{V} to be approximately $10^{-17}\,\text{V}^2/\text{Hz}$. For a typical motional mode frequency of $\omega_i/2\pi \approx 4\,\text{MHz}$, the current heating rate is approximately 1 quanta/ms, corresponding to an electric field noise spectral density S_{E} of $10^{-11}\,(\text{V/m})^2/\text{Hz}$. Increasing the characteristic distance D_{eff} through RF gradient minimization is necessary to reduce motional mode heating caused by RF components. To experimentally determine the technical limit, we measure the excitation rate of the motional mode by applying controlled excitations via the RF electrode, as discussed in Sec. 4.3.

$$R_{12} \approx \frac{\Omega_{\text{RF}}L}{Q} + R_{\text{wires}} + \frac{\theta}{\Omega_{\text{RF}}C} \tag{3.33}$$

$$R_{12}(\Delta\omega_i) \approx \frac{2\Omega_{\text{RF}}L/Q + \theta/\Omega_{\text{RF}}C + \theta\Omega_{\text{RF}}L}{4\Delta\omega_i^2/\Omega_{\text{RF}}^2 + 2\,(2/Q+\theta)\,(1/Q+\theta)} \tag{3.34}$$

In Fig. 41b, for a single site (e.g., T_2) in the triangular array, we determine the minimum D_{eff} by calculating the resultant electric fields at the trapping site position when biasing individual electrodes [123], as shown in appendix 12. To calculate the level of technical noise be-

tween terminals 1 and 2, we consider D_{eff} values ranging from approximately $1\,\text{mm}$ to $20\,\text{mm}$. Technical noise from active components, such as the AWG with a noise level of approximately $120\,\text{nV/Hz}$ [124], is attenuated by $50\,\text{dB}$ due to the RC filtering [125]. Based on these parameters, we estimate a maximum electric field noise spectral density S_{E} of approximately $10^{-13}\,(\text{V/m})^2/\text{Hz}$, which is two orders of magnitude lower than our current measured levels.For the thermal noise estimation, we consider only the equivalent resistance of the onboard capacitor $C \approx 820\,\text{pF}$, which is expected to be a few ohms. Using Eq. 3.35, where k_B is Boltzmann's constant, T is the temperature of the passive component, and R is its equivalent series resistance, we estimate the electric potential noise spectral density as $S_{\text{V}} \approx 10^{-21}\,(\text{V}^2/\text{Hz})$. This corresponds to an electric field noise spectral density $S_{\text{E}} \approx 10^{-15}\,(\text{V/m})^2/\text{Hz}$ in our setup.

$$S_{\text{V}} = 4k_B T R \tag{3.35}$$

In conclusion, given the current gradient minimization and filtering components, we estimate that noise contributions from both the RF components and control electrodes remain well below the measured ambient noise levels S_{E}. Dedicated experiments to estimate the current technical noise levels are discussed in Sec. 4.3.

Anamalous Noise: Surface Contaminants

In the ion trapping community, elevated noise levels in ambient-temperature surface trap architectures have been prevalent for decades, with mechanisms that are not well understood; this phenomenon is often referred to as anomalous heating [15, 16, 119]. By suppressing all thermal noise sources in cryogenic environments, researchers have reported heating rates of only a few quanta per second, consistent with their estimated thermal noise limits [126]. Here, we list some probable sources of this thermally activated noise:

1. Adsorbed contaminants such as carbon and oxygen on the gold surface due to exposure to the ambient atmosphere [120].

2. Exposed dielectric regions near the trapped ion [127].

3. Adsorbed or residual alkaline metals on the surface related to the loading process.

4. Diffusion of atoms within composite thin multi-metal layers.

All the above contributions are considered to lead to fluctuating patch potentials, acting as ther-

mally activated noise sources in the vicinity of the trapped ion and adding to the existing noise, as described in Eq. 3.36. Martinetz et al. [128] provide detailed descriptions of possible noise models, including fluctuating monopole and dipole models. Researchers have suggested different scaling factors with ion-to-electrode distances, such as $\alpha' \approx 6$ for the diffused adatom model [129], and various correlations with the motional mode frequency ω_i scaling factor β as a function of temperature [130]. However, in general, noise behavior often shows a monotonic relationship with $\alpha' \approx 4$ [120, 131]. To suppress and mitigate surface noise, various cleaning techniques have been successful, including laser cleaning (improvement by a factor of 2) [59], plasma cleaning (improvement by a factor of 4) [132], and chemical cleaning, which has shown improvements by orders of magnitude. A technique repeatedly shown to be effective is to treat the surface with accelerated ion beams, either in situ or ex situ [120, 133, 134].

$$S_{\mathrm{E}}(\omega_i^{\beta}) = \frac{S_{V,\text{technical}}}{D_{eff}^{\alpha}} + \frac{S_{V,\text{anomalous}}}{D_{\text{eff}}^{\alpha'}} + \dots \tag{3.36}$$

We modified our chamber [62] to accommodate a backfill-type sputtering gun[3], enabling an in-situ cleaning with argon ions sputtered on the surface trap chip. As shown in Fig. 42, the sputtering gun is mounted at an angle of 30° to the surface normal, while the imaging objective is tilted approximately 16°. Additional features were incorporated into the mask: one aperture to guide argon ions to the surface and another to collect fluorescence light. The sputter gun controller[4] is used to set parameters such as the acceleration voltage $(500-2000\,\mathrm{V})$, filament current (approximately $1.8\,\mathrm{A}$), resulting in a beam current of approximately $1\,\mu\mathrm{A}$. The beam is focused to a diameter of $5-6\,\mathrm{mm}$ at the position of the mask. We monitor the ion beam current using an in-built feature of the controller. Alternatively, we measure the current with a shunt resistor placed across the mask and ground to integrate and estimate the energy dosage E_{dosage} using Eq. 3.37, where V, J, and t represent the acceleration voltage, current density, and sputtering duration, respectively. The source gas for ion beam is a high-purity argon (99.9999%), leaked into the main chamber through a precision valve[5], which regulates the overall pressure and, consequently, the ion flux on the surface. An additional pump stand and pressure gauge are used to maintain a cleaner trapping environment by providing an ancillary volume for dosing argon gas into the main chamber.

$$E_{\text{dosage}} = V\,J\,t \tag{3.37}$$

[3]RBD Instruments 04-165, 2 kV
[4]Controller RBD 32-165
[5]Pfeiffer UDV 040/140

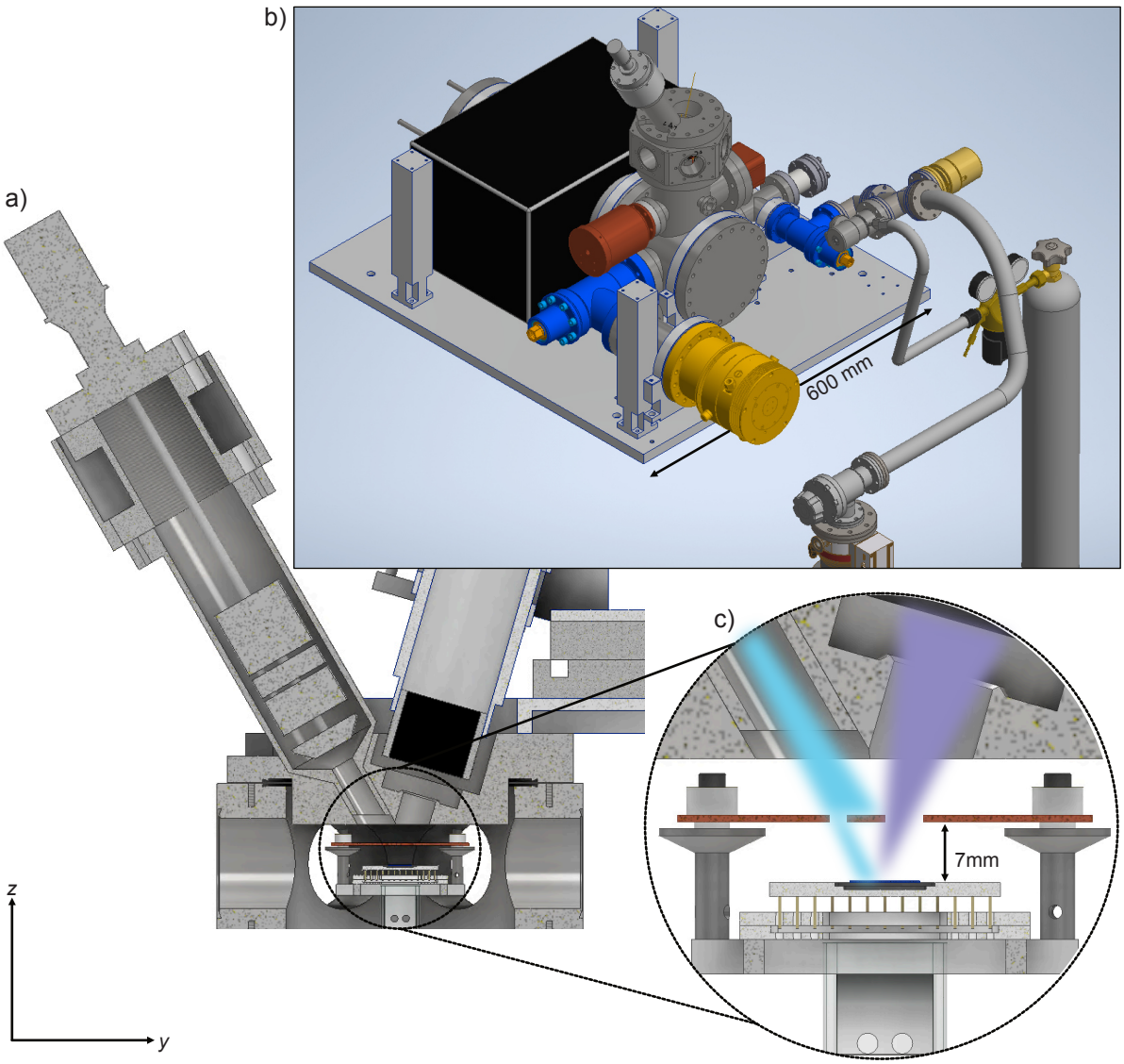

Figure 42: Custom UHV setup with in-vaccum sputtering capabilities. (a) Lateral cross-sectional rendering of the UHV chamber shows the unconventional top flange, which hosts the sputtering gun at a 30° angle to the surface normal, along with an imaging objective for collecting fluorescence light from atoms, positioned at an angle of approximately 16°. (b) The entire setup is shown, including the additional inlet section valve, precision valve, and an argon bottle (99.9999% purity). The presence of an IGP (black) with large pumping capacity enables hot-swapping without requiring a full bake-out between chip changes. (c) A zoomed section displays the modified top metal plate, approximately 7 mm from the trap-chip surface, which serves as both a shield and an off-surface electrode for applying global potential. It includes two apertures: one for imaging (blue cone) and another for directing argon ions onto the surface. False-color highlights (cyan) indicate the spatial extent of the argon-ion beam's impact on the metal plate, with a portion reaching the surface underneath. The blue cone represents the reduced collection efficiency due to the restricted imaging aperture.

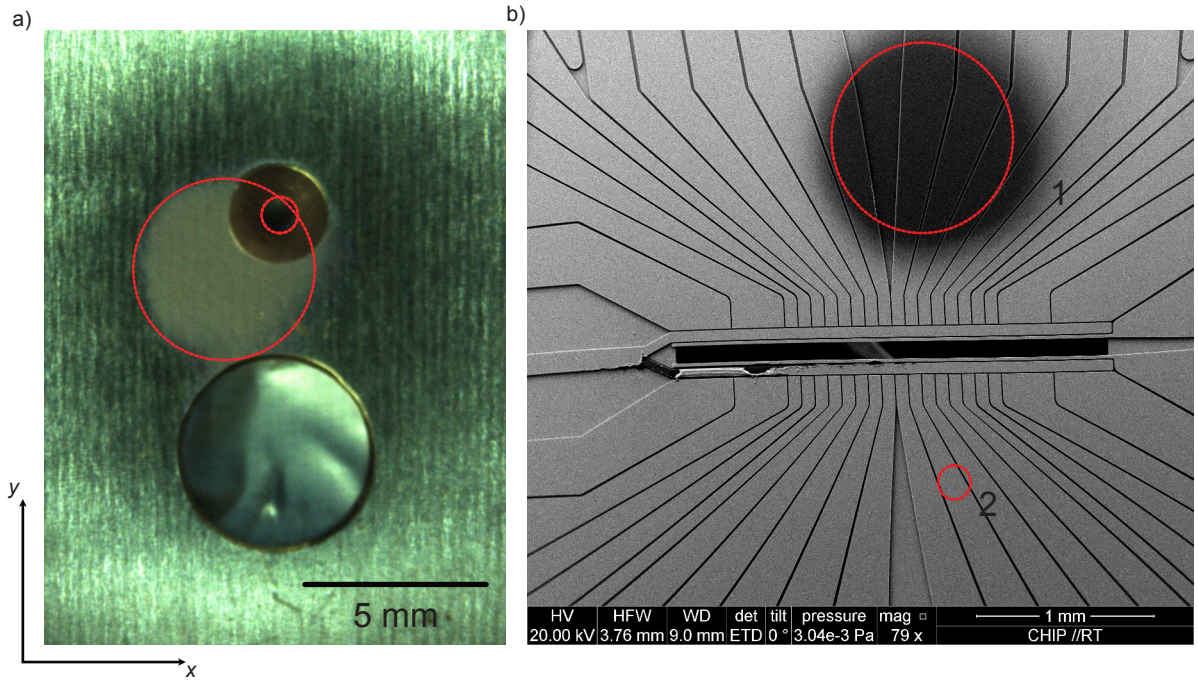

Figure 43: Impact of argon-ion sputtering on the linear trap. (a) The top metal plate channels argon ions to the trap surface. After an accumulated enegry dosage of $600\,\mathrm{J/cm^2}$, approximately a micrometer of gilded gold is removed. (b) The trap surface shows a region (black disk) where the directed argon-ion beam impact led to the removal of approximately $150\,\mu\mathrm{m}$ of gold, platinum, and titanium. The SEM image and EDX quantification indicate the presence of the underlying aluminum layer in this black region. A mismatch in the tolerances of the in-vacuum components resulted in a displacement of the ion-beam position relative to the trap center.

Work	**Kim et al.**	**Hite et al.**	**Our Work**	**Our Work**
Year	2017	2021	2021	2023/24
Gold Thickness	$\sim 150\,\mu\mathrm{m}$	$\sim 150\,\mu\mathrm{m}$	$\sim 70\,\mathrm{nm}$	$\sim 50\,\mathrm{nm}$
Beam Voltage (kV)	0.5	2.0	2.0	0.5
Current Density ($\mu\mathrm{A/cm^2}$)	$\sim 0.2 - 0.5$	~ 0.5	~ 5	$\sim 0.3 - 0.4$
Ion-Surface Distance (μm)	~ 63	~ 63	~ 80	~ 40
Dosage ($\mathrm{J/cm^2}$)	~ 1.5	~ 2.0	~ 600	~ 2.0

Table 6: Comparison of argon-ion-based surface cleaning attempts on different traps [120, 133, 134].

Element	**Au**	**Ti**	**Pt**	**Al**	**Cu**	**Si**	**O**	**C**
Area 1	NA	1.3(1)	NA	92.7(8)	0.3(1)	0.5(1)	1.5(3)	3.7(8)
Area 2	49.4(6)	2.4(1)	13.1(5)	30.7(4)	NA	NA	NA	4.3(6)

Table 7: EDX measurement results and weight percentages.

Table 6 summarizes similar works that successfully suppressed noise from surface contaminants and irregularities by factors of 10 to 100, focusing on comparisons involving in-situ cleaning. Figure 43 highlights one of our efforts to suppress surface noise. Using a linear surface electrode trap with an ion-to-electrode distance of $80\,\mu$m, we measured a normalized electric field noise spectral density of $S_{\mathrm{E}} \approx 10^{-11}\,(\mathrm{V/m})^2/\mathrm{Hz}$. An argon beam with a current density of $5\,\mu\mathrm{A/cm}^2$ was directed onto the trap chip surface through a 1 mm guiding hole. After each sputtering iteration, we measured electrode resistances using a multimeter and documented changes in trapping control potential configurations and harmonic oscillator mode parameters. Resistances between $0.1\,\mathrm{M}\Omega$ and $1.0\,\mathrm{M}\Omega$ were successfully cleared or "burned" at a success rate below 50% by passing current through the electrode relative to the RF ground. However, resistances below $100\,\mathrm{k}\Omega$ required higher currents to clear and were therefore directly connected to the RF ground, excluding them from control potential configuration calculations. These finite resistances likely result from the multiple residual materials deposited between the electrode and the RF ground layer, making complete removal less probable.

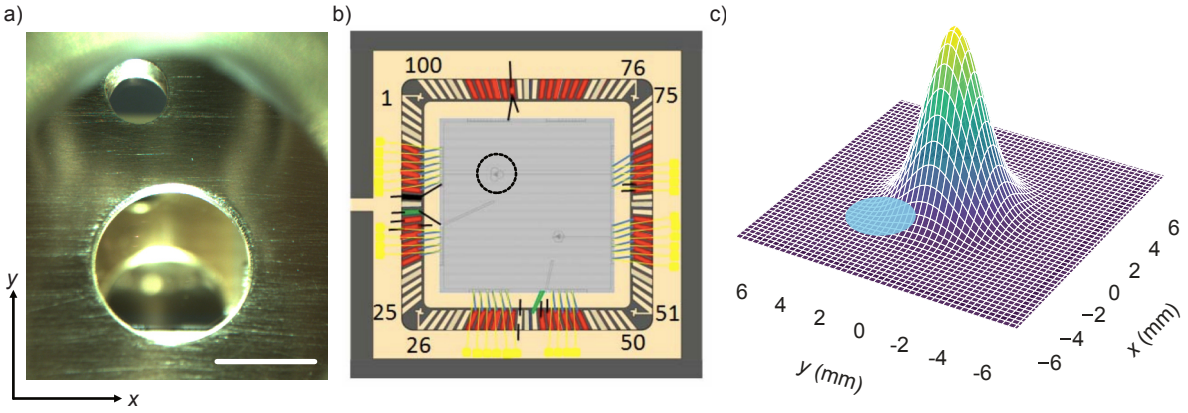

Figure 44: Mask design. A new mask with an off-centered hole was designed to channel the argon-ion beam towards the off-centered $40\,\mu$m array. (a) The top surface of the mask, installed in vacuum approximately 7 mm above the trap chip. (b) An illustration of the chip area $10\,\mathrm{mm} \times 10\,\mathrm{mm}$ showing the unused $80\,\mu$m array and the $40\,\mu$m array (black circle) offset from the chip center by $3.4\,$mm. (c) A 3D simulation of a possible Gaussian argon-ion beam. The solid disk (blue) represents the fraction of argon ions channeled through the hole, while the shaded region indicates the maximal ion beam incident on the mask.

We found that a mismatch in design tolerances led to a misalignment of the argon beam by approximately 1 mm. Over nearly 1000 minutes of argon-ion treatment, with an accumulated energy dosage of approximately $600\,\mathrm{J/cm}^2$, at least 150 nm of metal layers were removed, as shown in Fig. 43. Post-treatment examination under SEM[6] revealed the elemental composition in two preselected areas, as detailed in Table 7. In area 1, the absence or negligible presence of gold and a high concentration of aluminum indicated the removal of composite metal layers, exposing the thick aluminum layer fabricated above the silicon substrate. The detection of cop-

[6]Performed by Dr. Ralf Thomann

per likely resulted from sputtering-induced deposition of material from the mask onto the trap surface. Copper's high diffusion rate and its tendency to alloy with gold make it a problematic contaminant near the trap, as it can degrade performance by altering electrical and thermal properties.

Figure 44 illustrates the new mask design for in situ treatment of a triangular array, which addresses the challenges observed in previous iterations. Based on insights from earlier work, we designed a mask with thick gold electroplating to accommodate the off-centered trap array. The larger channeling hole compensates for lower current density and minimizes systematic misalignment. Additionally, the remaining mask area functions as a pseudo-Faraday cup, enabling ion current estimation during argon-ion treatments. The off-centered design significantly reduces the current density, making the setup suitable for less invasive iterations using the lowest possible acceleration voltages.

4 Results

This chapter presents experimental results that advance the development of our trapped-ion array platform toward small-scale building blocks for quantum networks. Building on the advanced methods described earlier, these results focus on demonstrating intra- and inter-site control mechanisms essential for reliable quantum state manipulation and transport across multi-dimensional arrays. Using enhanced local modulation capabilities, we achieve multi-mode coupling at a single site across all normal modes, enabling dynamic control over phonon directionality (Section 4.1.1). Additionally, a novel laser-free phonon coupling technique allows for indirect cooling of motional modes without direct laser access (Section 4.1.2). Inter-site transport techniques (see Sec. 3.2.4) are applied to explore their impact on motional and electronic states, with fluorescence-based motional mode analysis (see Fig. 29) revealing motional mode heating and identifying technical limitations (Section 4.2.1). Ramsey spectroscopy confirms that the transport process preserves electronic state coherence, underscoring the robustness of our approach (Section 4.2.2). To address noise sources contributing to motional-mode heating, we implement in-situ argon-ion sputtering to mitigate surface contamination. While this method has shown significant noise reduction in similar setups, constraints in our current trap chip design limit its effectiveness (Section 4.3.2). Together, these findings extend the capabilities of trapped-ion arrays by introducing techniques for deterministic state transfer, robust control, and noise mitigation, paving the way for an extendable quantum architecture with interconnected distributed nodes.

4.1 Intra-site: Multi-mode Coupling

To implement multi-mode coupling of all normal modes of a single ion at a single site, we need access to all corresponding curvature terms, such as H_{xy}, H_{xz}, H_{yz}, which address all dimensions using laser-less manipulation of fields via embedded control electrodes(see Eq. 3.2). We have demonstrated dynamic control over these curvature terms using laser-less manipulation via embedded control electrodes (see Sec. 3.2.2). However, our current control is limited to single-electrode modulation. To verify changes in motional population, we rely on laser interactions, which require an appreciable Lamb-Dicke parameter for accurate estimation(see Sec. 3.2.1). Considering these constraints, we present two key applications of our intra-site coupling method:

1. As a proof of principle, we demonstrate coupling of all normal modes of a single ion

with tunable coherent population transfer via sequential parametric drive, addressing all required curvatures.

2. We implement indirect cooling of a motional mode that is weakly coupled to our current laser configurations. This provides an alternative method to alter motional mode parameters, enabling the orientation of any normal mode to be changed for direct cooling via laser fields.

4.1.1 3D Coherent Control

To couple any two normal modes of a single ion at a single site and coherently transfer the motional population between them, we require at least two calibrated parametric drive frequencies, ω_{12} and ω_{13}. Using the two-mode coupling protocol (see Sec. 3.2.2), we resolve and calibrate the modulation frequency ω_{12} and the swap duration t_{12}. Subsequently, we employ a modified sequence, similar to the two-mode coupling protocol shown in Fig. 33. This sequence couples the motional mode ω_3, which typically has a mode vector perpendicular to the trap surface, to an in-plane normal mode ω_1. The motional mode ω_1 has direct laser access. To resolve the motional mode ω_3, we coherently excite it via a control electrode (electrode21) (see Fig. 1). Following modulation at the difference frequency ($\omega_{13} \approx \omega_3 - \omega_1$), and subsequent detection with the carrier method (see Sec. 3.2.1). Through dedicated measurements, we calibrate the duration of the swap t_{13} to ensure efficient population transfer. For a precise metrology of ω_3, it is necessary to account for avoided crossings, additional contributions from the dropped terms in Eq. 3.27, and higher-order coupling effects arising from anharmonicities. This approach enables an accurate determination of ω_3's properties under uncoupled conditions.

Figure 45a illustrates the experimental sequence used to access and coherently couple all three motional modes at a single trapping site. A single trapped ion is initialized at the T_2 site with all three modes cooled to the thermal limit T_D, with motional mode frequencies $(\omega_1, \omega_2, \omega_3)/2\pi \approx (3.70, 5.83, 5.22)$ MHz, each having a mean thermal population of fewer than 6 quanta. First, ω_3 is coherently excited using an oscillating uniform electric field to reach a mean coherent state population of $\bar{n} \approx 20$. Then a parametric drive with an amplitude $U_{13} \approx 2.5\,\mathrm{V}$ at the difference frequency $\omega_{13} \approx \omega_3 - \omega_1$ is applied for a fixed swap duration $t_{13} \approx 50\,\mu\mathrm{s}$, resulting in a coherent transfer of the motional population from ω_3 to ω_1. This is followed by another parametric drive with an amplitude $U_{12} \approx 1.5\,\mathrm{V}$ at frequency ω_{12}, where coherent transfers between the two modes in the plane are detected as a function of the modulation duration t_mod. Figure 45b shows the experimental data, where a sinusoidal model fit yields a swap duration $t_\mathrm{swap} \approx 260\,\mu\mathrm{s}$. Both in-plane modes are coupled to the spin using their dedicated Raman laser configurations, fol-

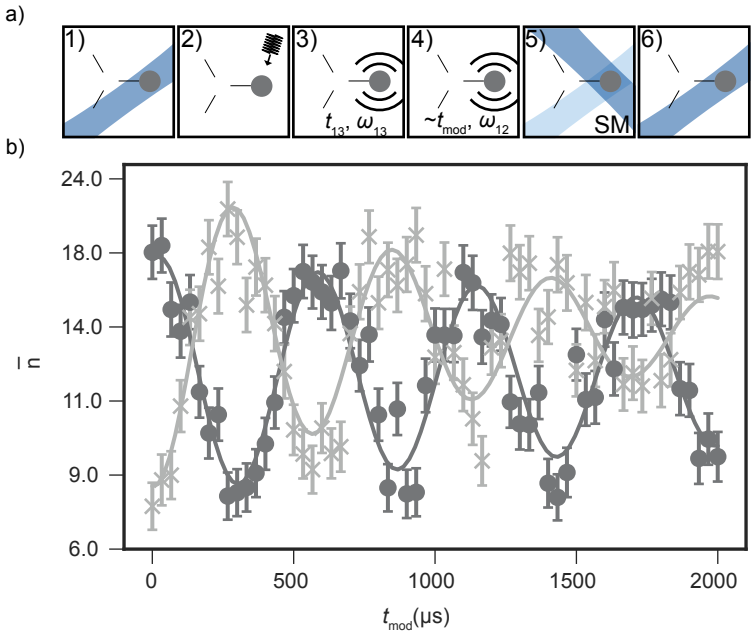

Figure 45: Coherent coupling of all motional modes. (a) Depicts the experimental sequence. (1) With the control potential configuration for T_2 enabled, a single ion is trapped and initialized at T_2. We resolve all three normal modes $(\omega_1, \omega_2, \omega_3)/2\pi \approx (3.70, 5.83, 5.22)$ MHz of the ion at the T_2 site. (2) With all modes cooled to the thermal limit T_D, we generate coherent states with a mean $\bar{n} \approx 20$ at ω_3. (3) This is followed by a complete swap from ω_3 to ω_1 at a modulation frequency of $\omega_{13}/2\pi = 1.51$ MHz, with $U_{13} \approx 2.5$ V for a duration $t_{13} \approx 50$ µs. (4) Next, we apply continuous modulation (t_{mod}) at $\omega_{12}/2\pi \approx 2.14$ MHz with $U_{12} \approx 1.25$ V. (5) This is followed by spin-motion coupling using two dedicated Raman beam configurations to address two in-plane modes (ω_1 and ω_2). (6) Finally, we record fluorescence after spin-motion coupling for motional mode analysis. (b) The plot shows the mapped motional state population of both in-plane modes ω_1 (disks) and ω_2 (crosses) from spin-state analysis as a function of t_{mod}.

lowed by fluorescence detection. Spin-state population analysis is used to determine $P_{\downarrow}$, and the corresponding mean motional population is estimated using the carrier method (see Sec. 3.2.1). For motional population estimation, calibration experiments are performed, such as carrier-method-based spin-motion mapping on a near-ground-state-cooled motional mode (e.g. ω_1), followed by coherent excitation using a control electrode (e.g. electrode 28).

Interestingly, the observed duration of coherent coupling exceeds the expected limitations of motional mode stability (see Sec. 3.1.3) by at least a factor of two, allowing for resolvable signals beyond 2 ms. We hypothesize that the coupling of motional oscillators reduces dephasing or mitigates common-mode noise [135]. These hypotheses require further verification through dedicated experiments and numerical analysis, such as measuring coherence times under varying coupling conditions. In conclusion, the implementation of parametric drives for different coupling combinations enables coherent access to arbitrary motional modes at a single trapping site within $100\,\mu$s. This positions a single trapping site as a reconfigurable node within a modular trapped-ion array, significantly enhancing its role as a component of an extendable quantum network. The ability to dynamically and flexibly steer phonons in arbitrary directions [45] is a critical feature for routing quantum information across such a network. By controlling phonon-mediated interactions at the intra-site level, we establish a foundational mechanism for achieving modular connectivity in trapped-ion arrays. Moreover, enabling parametric drives for all possible combinations (ω_{12}, ω_{13}, ω_{21}) simultaneously opens the possibility to observe interference effects among the three motional modes [44].

4.1.2 Indirect Cooling

In our work, the term "indirect cooling" refers to the ability to cool a motional mode to a near-ground state without requiring direct laser access [51, 136, 137]. Here, we demonstrate the cooling of the motional mode ω_3, whose mode vector ($\vec{u}_3$) is approximately perpendicular to the trap surface under the current control potential configuration, making it inaccessible to the existing laser setup. To achieve this, we couple ω_3 to an in-plane radial mode ω_1 using the intra-site coupling technique (see Sec. 3.2.2). In the present configuration, ω_1 has direct access to dedicated Raman beams for near-ground state cooling, due to its appreciable Lamb-Dicke parameter ($\eta \approx 0.2$). By leveraging this indirect cooling method, we significantly reduce the need for additional resources, such as laser fields, and minimize operational overhead, including the tuning of motional-mode parameters to tune the orientation of the motional modes.

Figure 46 demonstrates the indirect cooling of ω_3 via ω_1 using discrete coupling pulses. Through dedicated calibration measurements, we determine the difference frequency (ω_{13}) and coupling

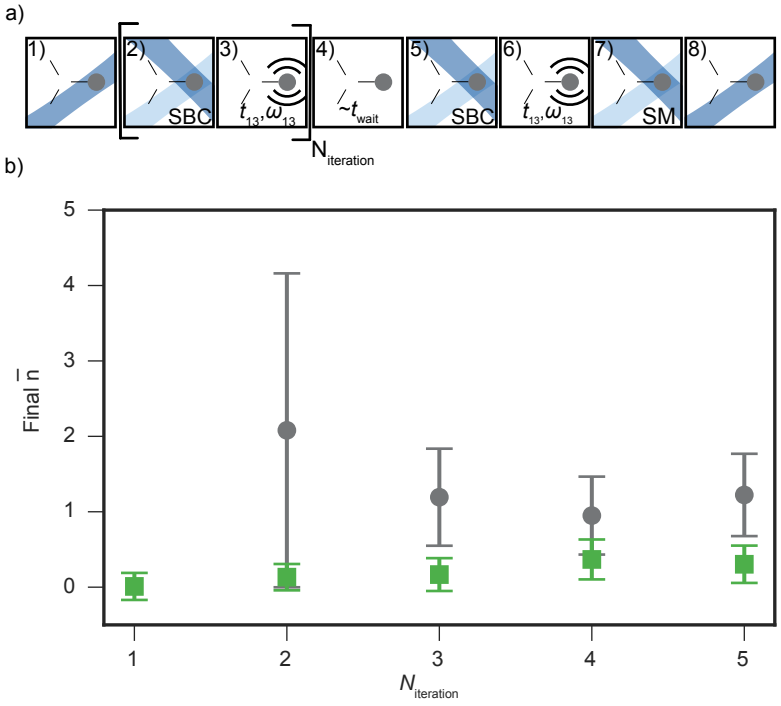

Figure 46: Indirect cooling of a normal mode (ω_3) via a laser-less technique. (a) Depicts the experimental sequence. (1) We initialize a single trapped ion at the T_2 site at the Doppler limit. (2) This is followed by near-ground-state cooling of the in-plane mode ω_1 with about 20 sideband cycles. (3) Subsequently, a swap pulse is applied at the difference frequency of $\omega_3 - \omega_1$. (4) Next, an optional wait duration t_{wait} is introduced. (5) Additionally, we near-ground-state cool the in-plane mode ω_1. (6) An additional swap pulse transfers the residual motional population from ω_3. (7) Finally, we perform red and blue sideband pulses. (8) We estimate $\bar{n}$ using collected fluorescence with the sideband contrast method. (b) Shows experimental data of average quanta $\bar{n}$ as a function of the number of iterations $N_{\text{iteration}}$ for the target motional mode ω_3 (disks), and the in-plane mode ω_1 (squares). Within 4 iterations, we reach a near-ground state of about $1.0(5)$ quanta at the motional mode ω_3.

rate (g_{13}) for a fixed modulation voltage (U_{13}). Figure 46a illustrates the experimental sequence. A trapped ion is initialized at the Doppler limit in all motional modes. The mode ω_1, which points away from the center of the trap, is cooled to the near-ground state using approximately 20 discrete sequential sideband cycles (see Sec. 28). Following this, a swap pulse is applied by driving an oscillating sinusoidal signal at the difference frequency $\omega_{13} \approx \omega_3 - \omega_1$ for a duration $t_{13} \approx 50\,\mu\text{s}$. This facilitates the transfer of the motional population between ω_3 and ω_1. Since a single swap pulse transfers only a fraction of the residual population [50], the sequence, including resolved sideband cooling on ω_1 and the swap pulse, is repeated multiple times ($N_{\text{iteration}}$). After cooling and swapping iterations, an optional tunable delay is introduced to measure the heating rate. The residual population is detected using spin-motion coupling with the sideband thermometry method. Figure 46b shows the experimental data for the residual population as a function of the number of swap iterations. For $N_{\text{iteration}} = 0$ and 1, the residual population remains above 3 quanta. By $N_{\text{iteration}} \approx 4$, the system consistently reaches the near-ground state with approximately 1 quantum. An unavoidable systematic delay occurs during sideband cooling of ω_1, introducing an additional delay $600\,\mu\text{s}$ before thermometry on ω_3. By tuning the waiting duration (t_{wait}), we measure the heating rate of ω_3 to be approximately 2 quanta/ms, while the heating rate of ω_1 is $0.5(1)$ quanta/ms.

With additional interleaved sequences that utilize dedicated Raman beams for the other radial mode (ω_2), we achieve a 3D near motional ground-state cooled ion. We can determine the heating rate of the inaccessible mode even with single-swap operations, since we are only interested in the relative motional population as a function of the waiting duration. Moreover, the ω_3 mode with its mode vector ($\vec{u_3}$) approximately parallel to the surface normal of the trap chip may be a more suitable probe for the observation of surface abnormalities leading to changes in the spectral density of electric field noise S_{E}. With sufficient resources to implement a parametric drive for continuous coupling of all three motional modes, we propose to cool all modes with significantly fewer resources, which can be helpful for handling larger arrays. Altogether, we gain access to initialize all motional modes to the near-ground state, a prerequisite for quantum information processing and metrology applications.

4.2 Inter-Site: Single-Ion Transport

In this section, we assess the effects of transport on both the electronic and motional degrees of freedom. We examine transport-induced motional mode heating and discuss potential causes. Using $^{25}Mg^{+}$ ions, we evaluated the stability of the electronic degrees of freedom between multiple transports and explored possibilities for coherent manipulations.

4.2.1 Motional State: Mode Heating

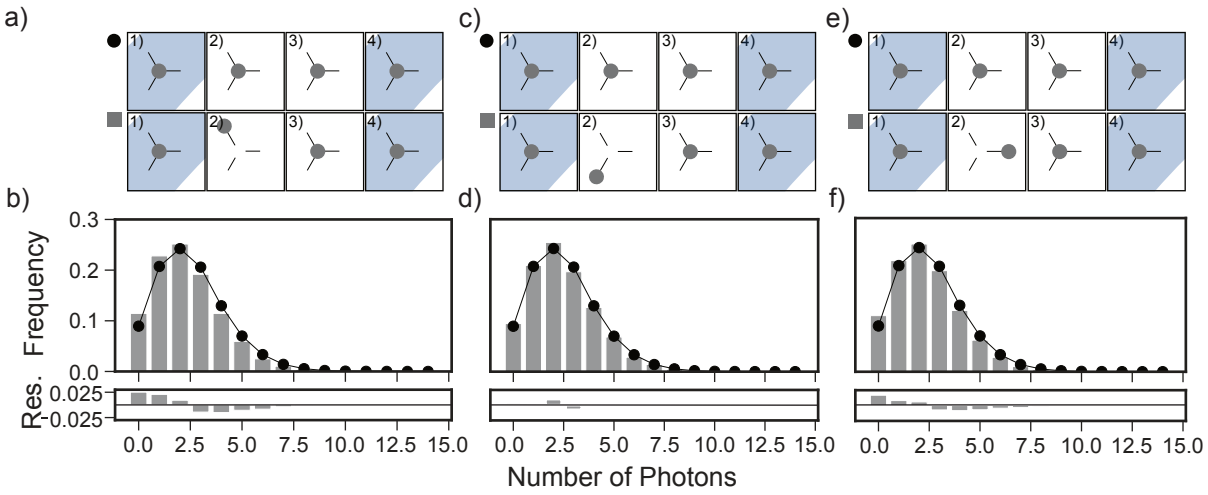

Figure 47: Motional mode heating due to ion transport. Figure adapted from [49]. Panels (a), (c), and (e) show identical experimental sequences involving round-trip transport to individual trapping sites (T_0, T_1, T_2) using control potential configurations Φ_c, where $c \in \{0, 1, 2\}$, executed within $2t_{\text{playback}} = 0.2$ ms. For reference measurements (indicated by disks), the control potential configuration is fixed at the T_H. The sequence is as follows: 1) A single ion is initialized at the T_H at the Doppler limit. 2) A waveform is executed to transport the ion to the target site within a duration of 0.1 ms. 3) Another waveform is then executed to transport the ion back to the T_H. 4) Finally, photons are collected with a PMT to estimate fluorescence changes relative to reference measurements. Plots (b), (d), and (f) display collected fluorescence over 11,000 repetitions (gray plots), compared with reference measurements (black curve). We estimate the average change in fluorescence and the corresponding thermal excitation for the motional mode at $\omega_1/2\pi \approx 1$ MHz, with results tabulated in Table 8.

To assess the impact of transport on motional modes, we employ a single $^{24}Mg^{+}$ ion and execute the transport waveform at minimal duration, using finely tuned control potential configurations (see Appendix A). Figure 47a illustrates the experimental sequence. In each sequence, we initialize a single ion at T_H at the Doppler limit. This is followed by round-trip transport to one of the triangular sites T_i, where $i \in \{0, 1, 2\}$, using the corresponding control potential configuration Φ_c, where $c \in \{0, 1, 2\}$, with a total duration of transport $2t_{\text{playback}} \approx 0.2$ ms.

With the detection beam placed at T_H, fluorescence is collected for a duration of $100\,\mu s$ over 11,000 repetitions for statistical analysis. As a reference, we store the ion in T_H for a duration of $0.2\,ms$ without transport. Figure 47b shows the histograms collected for round-trip transport to the three trapping sites. By comparing the mean photon counts of these histograms with the reference measurement, we estimate the average reduction in fluorescence due to round-trip transport, documented in Table 8. Because the transport duration is relatively short compared to the motional-mode frequency, we attribute the observed fluorescence loss to motional-mode heating. Using Eq. 3.26, we calculate the mean thermal distribution, considering the lowest frequency of the motional modes of $\omega_1/2\pi \approx 1\,MHz$.

Visited Site	**Fluorescence Change**	**Mode Heating (quanta/roundtrip)**	**Slew Rate (V/ms)**
T_0	-8.7(6)%	$\lesssim$287	< 4
T_1	-2.1(6)%	$\lesssim$84	< 3
T_2	-5.9(6)%	$\lesssim$197	< 3

Table 8: Change of fluorescence due to round-trip transport from T_H to all sites, following protocols illustrated in Figure 47. The table lists fluorescence changes, upper bound estimates of mode heating per roundtrip, and maximal slew rates required for waveform playback.

In conclusion, we identify several technical limitations in our transport protocol, specifically related to:

1. **Waveform Design:** The current transport waveform is limited to linear execution, which does not account for the non-uniform and asymmetric gradient along the transport path due to the height difference between T_H and the lower-lying sites.

2. **DAC Performance:** Our current DAC, with a noise floor of $< 120\,nV/\sqrt{Hz}$, requires discrete updates at a rate of $< 500\,kHz$ [124]. Additionally, the DAC's system clock is shared among channels, resulting in an asynchronous update routine between configurations, likely introducing sampling noise.

3. **Speed Constraints:** The passive filtering (cutoff frequency $f_c \approx 7\,kHz$) restricts waveform execution to durations $\leq 0.1\,ms$.

4. **RF Noise:** During transport, the ion remains for extended periods in transient regions of the pseudopotential landscape (potential depth $< 3\,meV$), corresponding to the noise levels of $-60(20)$ dBc (overall noise floor ≤ -100 dBc). Limited knowledge of the evolution of motional modes during transport and induced micromotion further increases the probability of RF noise-induced heating, estimated at $\dot{\bar{n}} \approx 1000$ quanta/ms for $\omega_i/2\pi \approx 4\,MHz$.

These conditions increase the likelihood of motional heating induced by RF noise.

To improve our transport routine, we can fine-tune control potential configurations and implement nonlinear waveforms that accommodate asymmetric gradients. Upgrading to faster DACs [53] with improved interpolation, reduced harmonic distortion, a lower noise floor, and synchronous update capabilities could reduce sampling noise. Employing higher-bandwidth passive filters to shorten the duration of the transport could also enable diabatic transport. Additionally, by synchronizing the RF drive amplitude with waveform execution, we can modify the pseudopotential to maintain a more uniform gradient between sites.

4.2.2 Electronic State: Coherent Manipulation

To benchmark the impact of transport on the electronic degrees of freedom of single trapped ions, we employ a modified Ramsey spectroscopy technique with interleaved transport [49, 138–142]. For this assessment, we used fine-tuned control potential configurations (see Appendix A) optimized for a minimal transport duration of $t_{\text{playback}} \approx 0.1\,\text{ms}$, verified by spatially resolved fluorescence image of the ions (see Fig. 40). In the Ramsey spectroscopy experiment, we utilize the field-insensitive transition ($F = 3, m_F = +1 \rightarrow F = 2, m_F = 0$), defined as $|\downarrow\rangle_c$ and $|\uparrow\rangle_c$, due to its longer coherence time, approximately three orders of magnitude longer than a single transport duration (see Sec. 3.1.3).

Figure 48 shows the resulting population $\text{P}_\downarrow$ in the Ramsey spectroscopy experiment with interleave transport, initialized from T_H to all lower-lying sites. Figure 48a shows identical experimental sequences, where a single $^{25}\text{Mg}^+$ ion is initialized and detected at the initial site (hub). As part of Ramsey spectroscopy, a superposition of the $|\downarrow\rangle_c - |\uparrow\rangle_c$ transition is then prepared using composite MW pulses (shown in Fig. 19), with interleaved round-trip transport to the chosen site, taking approximately $2t_{\text{playback}} = 0.2\,\text{ms}$. Finally, the ion is shelved back to the state $F = 3, m_F = +3$ for detection as a function of the analysis phase $\Delta\phi$. From sinusoidal model fits, we compare the extracted coherence amplitudes and phase information with reference measurements where the ion remains stationary at the T_H. We observe overall phase fluctuations within $\approx \pm 20^\circ$ for all cases, consistent with interleaved reference measurements. The coherence amplitudes align with background infidelities, approximately $82(3)\%$.

Additionally, we benchmark multiple sequential transports to all trapping sites using a similar experimental procedure. Figure 49 shows the experimental sequence: An ion is initialized in a superposition of the states $|\downarrow\rangle_c - |\uparrow\rangle_c$ in T_H, and at the end, the population $\text{P}_\downarrow$ is detected as a function of the analysis phase with interleaved transport to all sites via T_H, with a total transport

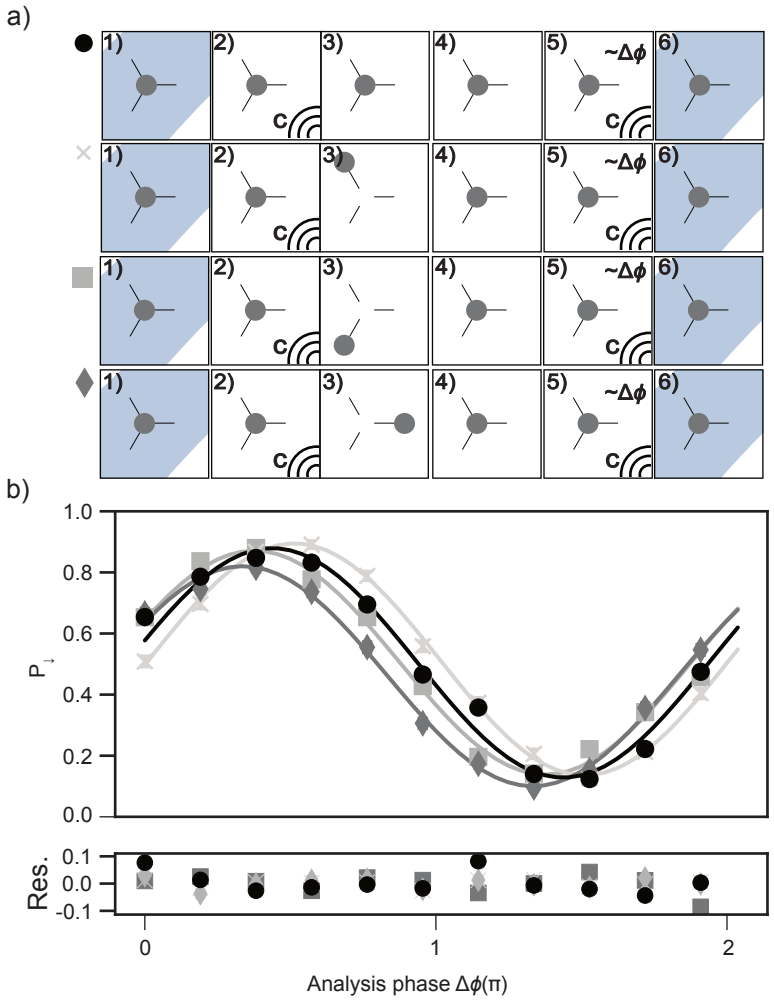

Figure 48: Individual transport round-trips to all three sites (T_0, T_1, T_2) from T_H. Adapted from our publication [49]. (a) The experimental sequence for Ramsey spectroscopy with interleaved round-trip transport to each of the three sites from T_H is illustrated. 1) A Doppler-cooled $^{25}Mg^+$ ion is initialized at T_H. 2) The superposition state $|\downarrow\rangle_c - |\uparrow\rangle_c$ is prepared using a composite MW pulse sequence. 3) and 4) A round-trip transport is executed via waveform playback within $t_{\text{playback}} \approx 0.2\,\text{ms}$. 5) Coherence is probed with an MW analysis pulse, with the phase $\Delta\phi$ used as a scan variable. 6) Fluorescence is collected at T_H for spin population analysis. (b) The resulting $P_\downarrow$ for all sequences is compared as a function of the analysis phase $\Delta\phi$. From sinusoidal fits, coherence amplitudes of 82(3)% and phase fluctuations ($\approx \pm 20°$) are extracted. By comparing these values with the reference measurement (disk), where the ion remains stationary at T_H throughout the sequence, we conclude that the extracted values are consistent with background effects and independent of ion transport.

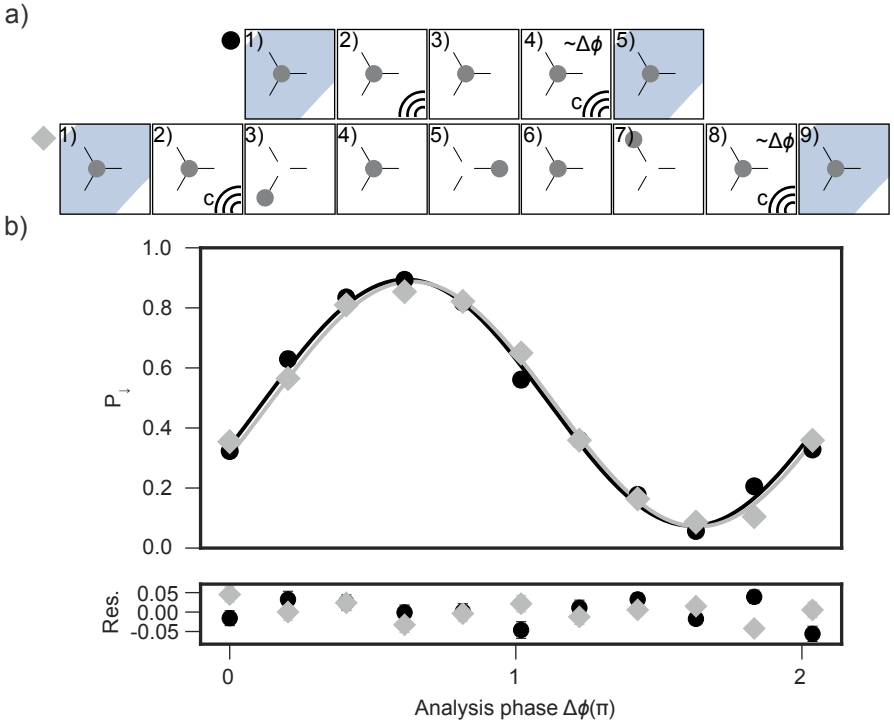

Figure 49: Multiple sequential relocations to all triangular sites from T_H. Adapted from our publication [49]. (a) Two experimental sequences are depicted. 1) A single $^{25}Mg^+$ ion is initialized at the Doppler limit at T_H. 2) Using composite MW pulses, the ion is prepared in an electronic superposition state $(|\downarrow\rangle - |\uparrow\rangle)$. 3) For the reference measurement (disk), the ion remains stationary at T_H. In the transport case (diamond), panels (3–7) illustrate the sequence where the ion undergoes sequential round-trip transport from T_H to each triangular site within approximately 0.6 ms. In both sequences, the final two panels show the probing of interference effects using an analysis MW pulse with phase $\Delta\phi$ as a scan variable, followed by fluorescence detection for spin state population analysis. (b) $P_\downarrow$ is shown as a function of $\Delta\phi$ for both sequences. From sinusoidal model fits, coherence amplitudes of 83(1)% (reference) and 82(3)% (transport) are extracted, with phase information of $4(4)^\circ$. The results confirm that the observed effects are consistent with the reference measurement, negligible, and independent of the transport protocol.

duration of $6t_{\text{playback}} \approx 0.6\,\text{ms}$. Using sinusoidal model fits, we extract coherence amplitudes of approximately $82(3)\%$, consistent with reference measurements. Despite a general fluorescence loss of $\leq 10\%$, the spin population analysis remains unaffected. Similarly, we observe that the extracted phase information is consistent with the reference measurement, with a deviation of about $4(4)\%$.

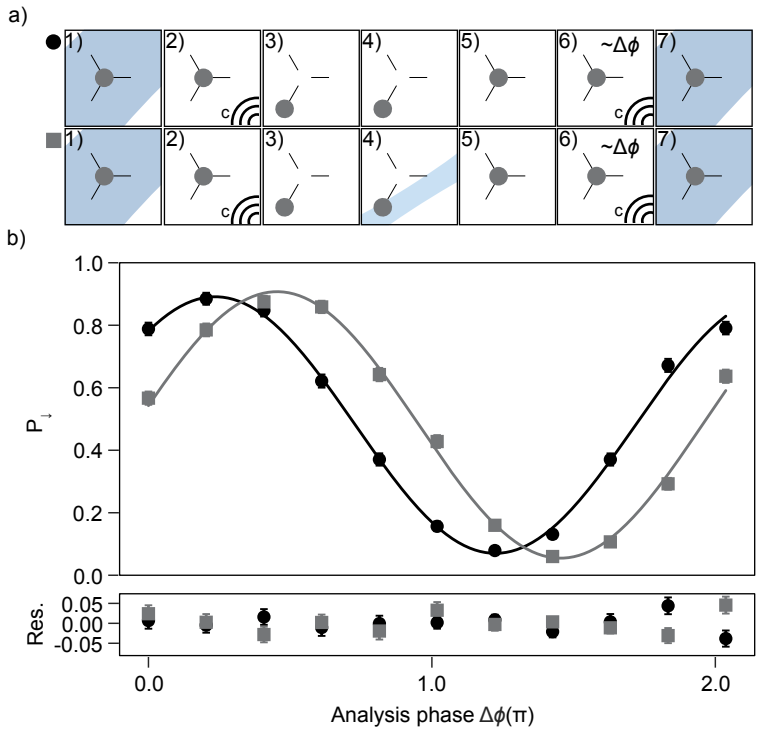

Figure 50: Local qubit manipulation with a focused beam. (a) illustrates two similar experimental sequences using Ramsey spectroscopy with interleaved transport to the T_1 site under two distinct conditions. In both cases: 1) A single $^{25}Mg^+$ ion is initialized at T_H at the Doppler limit. 2) Using composite MW pulses, the electronic superposition state $(|\downarrow\rangle - |\uparrow\rangle)$ is prepared. Panels (3–5) in both cases show the execution of round-trip transport of the ion to the T_1 site. In the second case (square), panel (4) shows the presence of a far-detuned focused beam incident on the ion. The final two panels (6–7) in both cases show interference detection with an analysis MW pulse, using phase $\Delta\phi$ as a scan variable, followed by photon detection for spin state analysis. (b) shows experimental data of $P_\downarrow$ as a function of analysis phase $\Delta\phi$ for the reference and in the presence of the beam for $t_{\text{beam}} \approx 50\,\mu\text{s}$. From sinusoidal model fits, we extract coherence amplitude and phase information, measuring a $2\pi \times 2.21(6)$ kHz AC Stark shift on the $|\downarrow\rangle - |\uparrow\rangle$ transition due to the far-detuned $(\approx 1000\Gamma)$ focused beam.

The ability to perform simple qubit operations interleaved with transport represents a prototype demonstration of the QCCD architecture. We demonstrate local manipulation of a trapped-ion qubit using a focused far-detuned laser beam, with crosstalks of $< 10\%$ at other trapping sites, as shown in Fig. 50. By placing the focused far-detuned beam near the T_1 site, we transport a single ion, prepared in a superposition state of $|\downarrow\rangle_c - |\uparrow\rangle_c$, to the T_1 site under two conditions: with and without the presence of the laser beam, for a duration of $50\,\mu\text{s}$. For detection, the ion

is transported back to T_H, followed by detection of $P_\downarrow$ as a function of the analysis phase $\Delta\phi$, as shown in Fig. 50b. From the plot, using a sinusoidal model fit, we extract phase information to determine a relative shift of $44(3)^\circ$. Due to local magnetic field gradients, we estimate an AC Stark shift of $2\pi \times 2.21(6)$ kHz.

In conclusion, we demonstrate the preservation of coherence in the electronic superposition state during transport, a critical capability for quantum information protocols. Leveraging tools such as local manipulation, detection capabilities, and the ability to redistribute and reorder multiple ions, we can enable experiments involving interleaved transport and light-matter interactions over extended durations. These experiments are primarily limited by the overall dephasing time of the electronic state, which is at least 100 times longer than the duration of individual transports, underscoring the robustness of this approach. The preservation of quantum coherence during transport establishes a foundational feature for modular trapped-ion networks, where ions can act as carriers of quantum information between the sites. However, the coherence of the motional state during transport is constrained by background noise and transport-induced heating, which also impacts electronic state detection through significant fluorescence loss observed after multiple successive transports. Addressing these limitations will be critical for extending the trapped-ion array into a flexible quantum network, enabling dynamic routing of quantum information and enhancing connectivity across multiple sites.

4.3 Motional heating: Mitigation efforts

In this section, we characterize potential factors that contribute to motional decoherence (heating) within our platform. We report on the noise characteristics of adjustable components, including the lasers, RF signals, control electrodes, and their associated peripherals, all of which interact with the motional degrees of freedom. Furthermore, we used an argon-ion bombardment technique to incrementally clean surface contaminants *in-situ* and probe the parameters of the motional mode, assessing any resulting surface modifications. All results presented here were obtained using the triangular array platform with a single trapped ion at the T_2 site.

4.3.1 Technical Noise

In experiments involving interacting laser beams, we actively control parameters such as frequency, amplitude, phase, and interaction duration using multiple electronic controls (see Fig. 12). Variations in these parameters can introduce operational infidelities in the manipulation of motional and electronic degrees of freedom. However, most fluctuations result in dephasing effects on the electronic degrees of freedom without altering the energy of the motional degree of freedom. The execution of multiple interacting sources, primarily in discrete sequences with high timing precision, necessitates a high extinction ratio for optical elements. Without adequate optical isolation, on- and off-resonant scattering events may occur, leading to decoherence in both internal and motional degrees of freedom. Upstream of the trapped ion, an AOM, which is the final controllable optical element, achieves an extinction ratio of $\geq$ 40 dB in a single-pass configuration (see Fig. 8). Using RF switches between frequency sources and AOM, we maintain and ensure RF signal isolation of $\geq$ 60 dB. When isolation is insufficient, stray photons, whether on- or off-resonant, can induce loss of coherence. For ions confined near the motional ground state, the scattering dynamics described by Leibfried *et al.* [16] suggests two potential outcomes: one involving elastic scattering via the carrier, which causes decoherence of internal states without affecting the motional degree of freedom, and the other involving the blue sideband, leading to incoherent excitation that is suppressed by approximately η^2 compared to the carrier (see Eq. 3.9).

We verify the isolation of each laser beam using the experimental sequence shown in Fig. 51a. A single ion is initialized at the T_2 site, with a motional mode near the ground state at $\omega_2/2\pi \approx 3.35\,\text{MHz}$. We use different beams on demand for a variable duration t_{beam}, followed by spin-motion coupling on the carrier and motional state detection via fluorescence collection on the carrier (see Sec. 3.2.1). Two distinct experimental conditions are defined: (1) the ion is prepared in the near-ground state $F = 3, m_F = +3$ state, defined as $|\downarrow\rangle$, during interaction; (2)

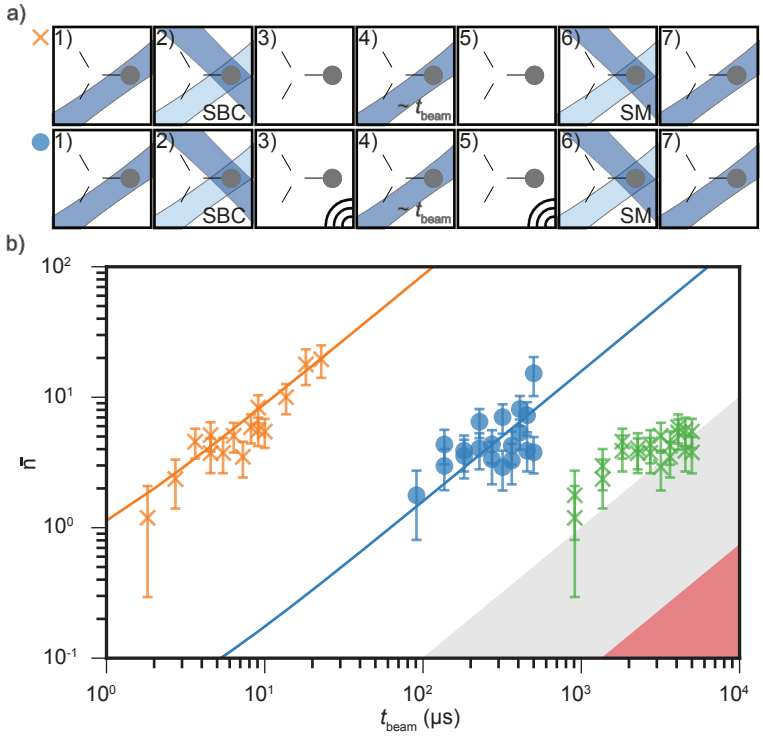

Figure 51: Induced motional excitation due to interaction with laser beams. (a) illustrates two similar experimental sequences: (1) In both experiments, a single $^{25}Mg^{+}$ ion is initialized at the T_2 site at the Doppler limit. (2) A motional mode, $\omega_2/2\pi \approx 3.35\,\text{MHz}$ with $\eta \approx 0.2$ for all individual beams, is near-ground-state cooled using a dedicated Raman beam configuration (B1+R2). (3) In the first sequence (cross marker), the ion is optically pumped to the $F = 3, m_F = +3$ state ($|\downarrow\rangle$). In the second sequence (disk marker), the ion is shelved in the $F = 2, m_F = +2$ state ($|\uparrow\rangle$), detuned by $2\pi \times 1.541\,\text{GHz}$. (4) The ion is then exposed to near-resonant beams (BD, BDx) as well as off-resonant beams for a variable duration, t_{beam}. (5) In both cases, the ion is returned to the $F = 3, m_F = +3$ state if it is not already there. (6) Using the same Raman beam configuration, we couple the motional information to the internal state via spin-motion coupling. (7) Finally, photons are collected to analyze motional population using the carrier method. (b) shows the detected mean thermal population as a function of t_{beam}. High excitation rates are observed with BD and BDx (orange), measuring $850(80)$ and $560(80)$ quanta/ms, respectively, when the ion is in the $|\downarrow\rangle$ state. A reduction of approximately $20\,\text{dB}$ (blue) is observed when the ion is in the $|\uparrow\rangle$ state. Excitation rates for other beams (RD, RP, and Raman; green) remain consistent with the reference heating rate (gray shaded region). We estimate the extinction ratio of the AOMs to be $\geq 30\,\text{dB}$. Given the manufacturer-rated extinction of $\approx 40\,\text{dB}$, the heating rate is expected to be ≤ 0.050 quanta/ms (red shaded region).

Beams	$\Delta/(2\pi)$ (MHz)	I (I_{sat})	$\dot{\bar{n}}$ at $\|\downarrow\rangle$ (/ms)	$\dot{\bar{n}}$ at $\|\uparrow\rangle$ (/ms)	Num. at $\|\downarrow\rangle$ (/ms)	Num. at $\|\uparrow\rangle$(/ms)
BDx	0(1)	≈0.5	850(80)	16(4)	946	0.3
BD	20	≈0.5	560(80)	8(2)	651	0.3
Raman	20×10^3	≈300	1.0(2)	1.0(2)	≈0	≈0

Table 9: Numerical and Experimental excitation rates due to incoherent interaction with different beams configurations.

the ion is shelved in the $F = 2, m_F = +2$ state, $|\uparrow\rangle$, detuned from the $S_{1/2} - P_{3/2}$ transition by 1.541067(1) GHz during interaction, then returned to $|\downarrow\rangle$ for detection. With $\eta \approx 0.2$ for all the beams that interact, we plot the mean motional population as a function of the interaction duration for all the beams in Fig. 51b. In the first condition, we observe that on- and near-resonant beams, such as BD and BDx, lead to an increased excitation rate (orange) when the ion is in the $|\downarrow\rangle$ state. In the second condition ($|\uparrow\rangle$), both BD and BDx (blue) show a reduction in the excitation rate of approximately 20 dB. For other beams (RD, RP, and Raman beams), we observe that the excitation rate remains consistent with the reference heating rate of approximately 1 quanta/ms, regardless of the experimental condition. In the case of the BDD beam, we observe relatively higher decoherence during spin-motion coupling, requiring further investigation regarding decay to other hyperfine manifolds. For the repumper beams (RD and RP), detuned by THz from the addressed two-level system, we observe that excitation rates due to individual beams are consistent with the reference or ambient heating rate. Using Eq. 3.10 and the chosen beam parameters in our platform, we calculate the expected excitation rate for different conditions, as shown in Table 9. From the table, we infer that optical isolation must be ≥ 30 dB for all individual beams, limited by the reference excitation rate. Due to non-optimal polarization of the Doppler beam and infidelities in state preparation, we observe increased excitation rates with BD and BDx beams when the ion is shelved in the $|\uparrow\rangle$ state. Based on manufacturer specifications for the extinction ratio, we infer that the excitation rate should be ≤ 0.050 quanta/ms, assuming a motional mode $\omega_i/2\pi \approx 5$ MHz, which corresponds to an electric field noise spectral density $S_{\mathrm{E}} \approx 10^{-13}\,(\mathrm{V/m})^2/\mathrm{Hz}$. However, our current noise level is approximately $10^{-11}\,(\mathrm{V/m})^2/\mathrm{Hz}$. In addition, we use motional mode information to calculate the collection efficiency of our imaging optics system. Using the calculated scattering events due to the BDx laser beam via numerical methods and collected photon counts, we estimate the detection efficiency to be 0.00045(5). We attribute this efficiency loss to modifications in the top flange, which significantly reduce the solid angle of detection (see Fig. 42).

For noise contributions from the RF electrode, we consider noise at frequencies $\pm\omega_i$ around the RF drive frequency (Ω_{RF}). We estimate voltage noise using a lumped element model (given in Eq. 3.36) to be $< 10^{-17}\,\mathrm{V}^2/\mathrm{Hz}$. Ideally, a trapped ion at the RF minimum is insensitive to modulation at the trap frequency. However, displacement from the RF minimum due to stray

fields increases the probability of incoherent excitation via RF noise. To verify excitation from the RF electrode, we inject a coherent signal or broadband noise modulated via the RF electrode, generated by a single AWG channel, and use a trapped ion as a sensor to estimate excitation rates for a single motional mode. Figure 52 shows the calibration of the injected signal relative to the power of the RF drive carrier. Using the configuration shown in Fig. 10, we modulate the input RF drive at the motional mode frequency (ω_i) via a single channel of an AWG or an external voltage source, as a function of modulation amplitude A_{mod}. A spectrum analyzer is used to monitor the pickup signal, allowing us to estimate the strength of the signal injected at the sideband frequency ($\Omega_{\text{RF}} \pm \omega_i$) relative to the carrier RF signal, represented in dBc.

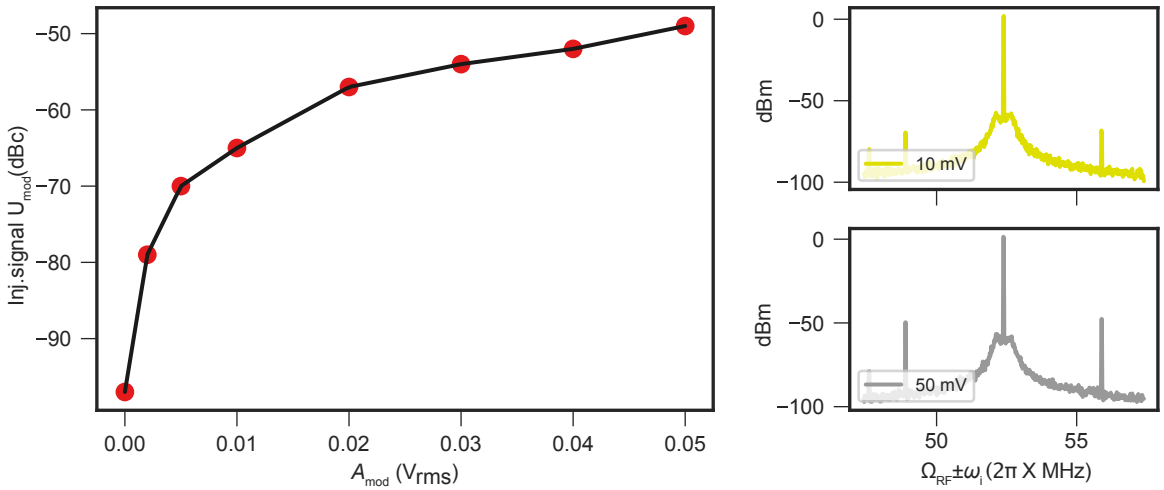

Figure 52: Calibration of modulation amplitude at the RF electrode. The left plot shows the sideband amplitude (injected signal strength) in dBc as a function of external modulation amplitude. By applying external modulation from 0 to 50 mV_{rms}, we estimate a maximum amplitude of approximately -50 dBc at the RF electrode, measured via pickup signal detected with a spectrum analyzer. The left plot displays the sideband amplitude at the RF electrode ($\Omega_{\text{RF}} \pm \omega_i$) as a result of the external modulation voltage. With the calibration data, a simple lookup table is prepared to directly map the corresponding modulation amplitude with injected signal strength. The right plots show examples of the sideband response with 10 mV and 50 mV external modulation, respectively.

Figure 53a shows the experimental sequence with a single trapped ion initialized at the T_2 site, with $\bar{n} \approx 0$ in the motional mode $\omega_1/2\pi \approx 3.7$ MHz. We modulate the RF signal for a fixed duration of 10 µs. For low excitation levels below 3 quanta, we use sideband thermometry to estimate motional population (cross markers). For higher excitation levels, up to 20-30 quanta, we use the carrier method (dot markers). We collect fluorescence to analyze spin-state probability and map it to the motional population. Figure 53b shows the estimated excitation rate as a function of the modulation amplitude in dBc. With a measured noise floor (green shaded area) at -100 dBc, we applied modulation amplitudes up to -45 dBc. We detect excitation from -70 dBc onward with sideband thermometry and from -50 dBc with the carrier method. Fitting a quadratic model with and without offset, we estimate a gradient of $7.8(5) \times 10^3$ quanta/ms/dBc^2, which

is proportional to the pseudopotential gradient $\frac{\partial}{\partial_i}\Phi^2$ along the motional mode vector i. We observe discrepancies between the two methods for estimating the motional population, which we attribute to anharmonicity, resulting in lower than expected excitation above approximately 10 quanta. For optimal noise limit determination, we rely on the carrier method analysis. For lower excitation experiments analyzed with sideband thermometry, we estimate a conservative upper-bound noise level of approximately 0.01 quanta/ms. Based on the extracted offset, we conclude that the technical noise level is below -70 dBc, with the reference heating rate marked at approximately 1 quanta/ms (red dashed line). With the current micro-motion minimization routine, the noise limit approaches approximately 0.001 quanta/ms (green dashed line), disregarding the anomalous heating constraint. Since $\dot{\bar{n}} \propto \left(\frac{\partial}{\partial_i}\Phi^2\right)^2$ [121], minimizing the gradient, if constrained, could further reduce the noise limit to the Johnson-Nyquist limit. Alternatively, this method, which is sensitive to single quanta, could be reverse-engineered to minimize the gradient with higher precision. We conclude that technical noise in the RF electrode, even with the current micro-motion minimization routine, is three orders of magnitude lower than the anomalous heating reference measurement.

Similarly, we estimate the technical noise level on the control electrodes using the experimental sequence shown in Fig. 54. First, we assume that the noise in all the electrodes is uncorrelated. Furthermore, we calculate the effective distances D_{eff} of all electrodes from the single ion position at T_2 (see Table A). The effective distances range approximately from 1 mm up to 20 mm. From technical noise estimation, for effective distances around 1 mm, we find the spectral density of electric field noise to be lower than $10^{-14}\,(\text{V/m})^2/\text{Hz}$. To verify the excitation rate, we chose one of the electrodes with a low effective distance (say electrode 28) and an applied field nearly parallel to the motional mode ($\vec{E}_i \parallel \vec{u}_i$). This electrode drives oscillations at the motional mode frequency $\omega_i/2\pi \approx 3.5\,\text{MHz}$ for a fixed duration of $10\,\mu\text{s}$ via a single AWG channel. We perform the experiment with a variable amplitude U of the oscillating field at the trap frequency and employ two different passive filtering options. Both passive filters are single-stage RC filters with resistor values R_1 of $26\,\text{k}\Omega$ (labeled typical) and $0.5\,\text{M}\Omega$ (labeled aggressive), to ensure absolute filtering of 50 and 80 dB, respectively (simulated with the SPICE model) at $\omega_i/2\pi \approx 5\,\text{MHz}$ [125]. We detect the motional population using the carrier method with collected fluorescence.

Figure 54b shows the experimental data of the measured excitation as a function of the signal amplitude U for typical (blue) and aggressive (orange) filters. We include a reference heating rate measurement without applied oscillating voltage at the noise floor value of the AWG channel, which is 120 nV. Using a fit of a composite model of a quadratic function with an offset, we extract gradients that suggest at least 20 dB of filtering of the oscillating signal at the motional mode frequency ω_i. A quadratic fit without offset indicates a probable noise limit for the control electrodes approaching 0.001 quanta/ms, corresponding to an approximate noise spectral

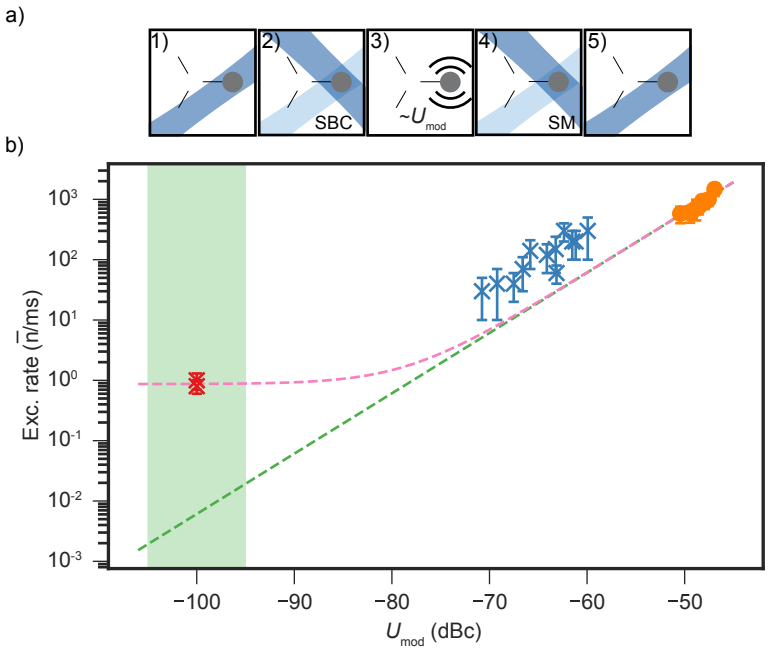

Figure 53: Induced excitations by modulating the RF signal at the trap frequency. (a) shows the experimental sequence: (1) We initialize a single $^{25}Mg^{+}$ ion at the Doppler limit at the T_2 site. (2) Using a Raman beam configuration (B3+R2), we near-ground-state cool the motional mode at $\omega_1/2\pi \approx 3.7\,\mathrm{MHz}$. (3) We modulate the RF electrode at ω_1 with a variable signal amplitude U_{mod} for a fixed duration of approximately $10\,\mu\mathrm{s}$. (4) For lower excitations, we use sideband contrast thermometry, and for higher excitations, we utilize the carrier method. (5) Finally, we collect fluorescence for motional population analysis. (b) shows the estimated excitation rates as a function of U_{mod}, using both methods. With a quadratic fit (excluding and including offset), we determine a technical noise limit approaching 0.001 quanta/ms (green dashed line), currently limited by the gradient minimization limit, and an offset representing an anomalous heating rate of approximately 1 quanta/ms (red dashed line).

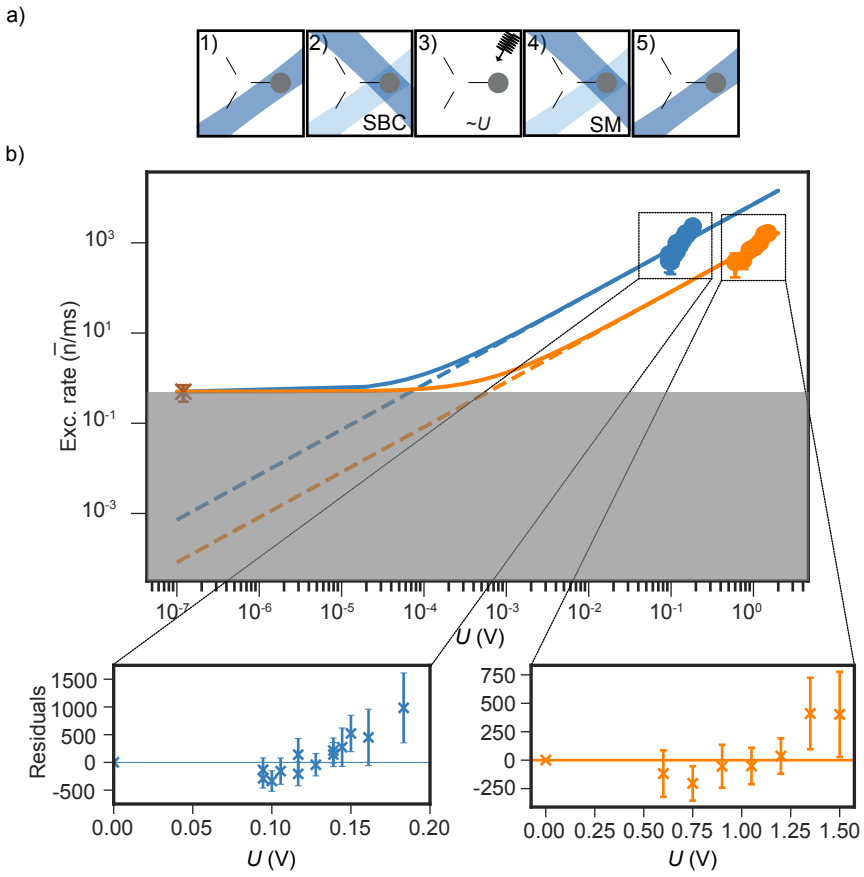

Figure 54: Aggressive filtering and technical noise estimation on control electrodes. (a) illustrates the experimental sequence: (1) We initialize a single $^{25}Mg^{+}$ ion at the T_2 site. (2) The motional mode $\omega_1/2\pi \approx 3.5\,\text{MHz}$ is near-ground-state cooled using dedicated Raman beams (B_3 and R_2) with an effective Lamb-Dicke parameter $\eta \approx 0.2$. (3) Coherent excitation is applied via a single electrode (electrode 28), driven by a single AWG channel with two different filtering options: Typical (blue) and Aggressive (orange), with the signal amplitude U as a scan variable. (4) Finally, motional state population is detected using the carrier method with collected photons.(b) shows the experimental data of estimated mean motional quanta for both filters, along with the reference measurement (ambient heating rate) marked at 120 nV and the noise floor indicated (gray). Using a quadratic model fit (with and without offset), we extract excitation rates and limits for the two different filters. We observe approximately $20\,\text{dBv}$ relative suppression of the oscillating signal with the aggressive filter, and the Johnson-Nyquist limit for both filters approaches at least three orders of magnitude lower ($\approx 0.001\,\text{quanta/ms}$) than the reference heating rate. Zoomed residual plots highlight increasing uncertainties as a function of higher quanta due to systematic effects in the estimation method, such as spin-state infidelities and anharmonicity, which lead to motional mode instabilities.

density S_{E} of $10^{-14}\,(\mathrm{V/m})^2/\mathrm{Hz}$ for the typical filter and an order of magnitude lower for the aggressive filter. The residuals highlight increased uncertainties in estimating the motional population at higher excitations because of the systematic limitations of the carrier method. These residuals show deviations from the expected quadratic fit at higher motional populations, likely due to spin-state infidelities and motional mode instabilities caused by anharmonicities.

Using Eq. 3.23, we determine the electric field $\vec{E}_i$ at the ion's position along mode u_i with the typical filter being approximately $1.7\,\mathrm{mV/m/V}$, normalized to the applied potential. Assuming $\vec{E}_i \parallel \vec{u}_i$, we verify the attenuation of our typical filter to be approximately $55\,\mathrm{dBm}$, while the aggressive filter provides about $75\,\mathrm{dBm}$, both agreeing within $5\,\mathrm{dBm}$ of the SPICE model. We cannot fully account for the current reference noise level, even with noise estimations from all electrodes. Thus, we conclude that technical noise from both the RF and control electrodes is not a dominant factor contributing to anomalous heating. Considering other on-demand, real-time manipulation of motional modes and transport requirements, we suggest that the aggressive filtering option may not be necessary. Additionally, we estimate thermal noise near the ion by considering only the equivalent series resistance (ESR) of the onboard capacitor; using such high resistances in passive filtering elements also contributes to the overall Johnson-Nyquist noise.

Other technical noise sources, such as electromagnetic pickup from urban wiring and blackbody radiation, are expected to contribute significantly less than the mechanisms listed above. In similar trap architectures, these sources typically remain below $10^{-17}\,(\mathrm{V/m})^2/\mathrm{Hz}$ [121]. We ensure proper grounding of all active elements and use optical isolators to decouple specific functional components. Potential mechanisms contributing to the excess heating rate may include lossy dielectrics near the trapped ion, such as the loading hole, which can increase the contribution from blackbody radiation. Additional sources may involve anomalous heating due to surface contaminants and fluctuating patch potentials arising from diffused atoms [15, 95].

4.3.2 Anomalous Noise

With a modified setup (shown in Fig. 42) designed to accommodate a sputtering gun, we aim to suppress the suspected causes of additional unaccounted for electric field noise near the ion, similar to the experiments conducted at NIST [120]. The goal of the sputtering procedure is to remove adsorbed contaminants from the pristine gold surface. By removing these contaminants, we target: (1) a reduction in faster oscillating sources near trap frequencies, leading to lower electric field noise and decreased motional-mode heating; and (2) a reduction in slower oscillating sources, resulting in improved motional-mode stability and lower dephasing rates.

We select sputtering gun parameters (see Fig. 58 in the appendix) with a beam voltage set to 500 V and an argon beam flux current of less than $1\,\mu$A. The diameter of the argon beam in the mask is approximately 5-6 mm, resulting in current densities in the range of $0.3 - 0.4\,\mu\text{A/cm}^2$, likely reaching the trap area. The duration of sputtering is set between 5 and 15 minutes. In Fig. 55, we compile the relevant parameters of the motional mode as a function of the iteration of the treatment. The top plot shows the estimated energy dosage in J/cm^2, calculated from the measured current during sputtering, for an overall duration of 270 minutes. This yields approximately 3 J/cm^2. We highlight two reference lines (orange) [134] and (yellow) [133], with approximate values of 1.5 and 2 J/cm^2, respectively. These reference values indicate similar work on surface trap architectures [143] that achieved significant noise reduction by removing a few carbon monolayers. After each argon sputtering iteration, we verify motional mode variations with a single trapped ion at the T_2 site. We adjust the control potential configuration to match the motional modes and plot the absolute electric field variation (the second plot is green). Within the first five iterations, we observed an overall variation of 1 V/mm, possibly due to the removal of adsorbed magnesium atoms on the surface from previous failed ion-loading attempts. No similar extreme changes were observed during the next 200 minutes. We measure the resistance of all in-plane electrodes relative to ground (RF) after each iteration and plot the average resistance for electrodes with finite values (typically between 1-7 electrodes) as a function of the duration of treatment (pink plot). A clear trend shows decreasing resistance as a result of sputtering, likely caused by material re-deposition near electrode gaps. Additionally, we measure parameters of two in-plane modes, such as motional bandwidth and dephasing rates, after each iteration. We observe a fivefold improvement in motional mode coherence for both modes and note a correlation between accumulated resistance and decreasing coherence times, indicating a probable decline in surface quality due to the sputtering process.

We measure heating rates in both in-plane modes at the T_2 site after each iteration, with the motional mode frequency tuned via control potentials to match within 100 kHz. We plot the normalized electric field noise spectral density, S_{E}, of both in-plane modes ($\omega_1/2\pi = 3.7(1)\,\text{MHz}$

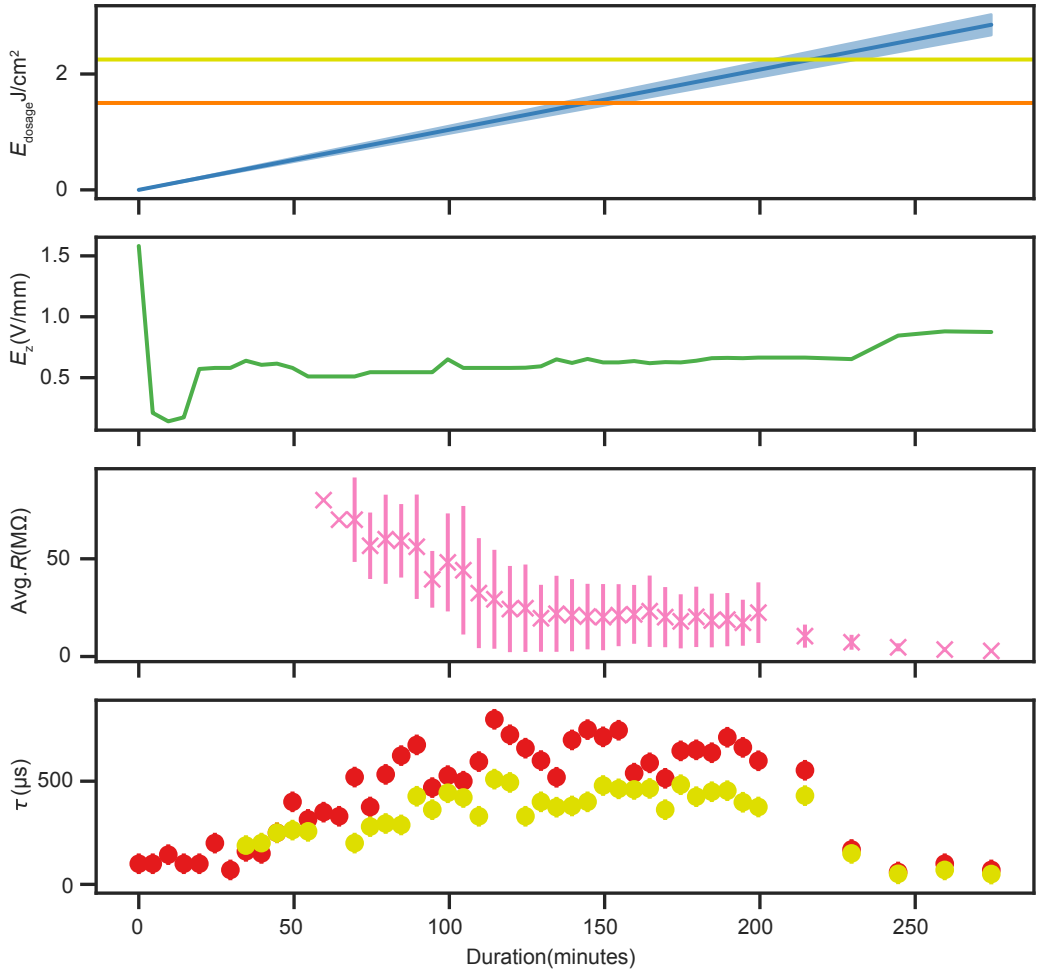

Figure 55: Collection of parameters to monitor surface treatment effects as a function of treatment duration. From top: (1) The first plot shows the accumulated energy dosage calculated with Eq. 3.37, based on collected current at each treatment in the range of $0.3 - 0.4\,\mu\mathrm{A/cm}^2$. Two reference lines at $1.5\,\mathrm{J/cm}^2$ (orange) [133] and $2.2\,\mathrm{J/cm}^2$ (yellow) [134] depict the work of Kim and Hite et al., which achieved a tenfold reduction in heating rate in a different architecture [143]. (2) The second plot shows changes in the compensation field along the z-direction to ensure consistent confinement in all directions. In the first few treatments, we observe $\Delta E_Z \approx 1\,\mathrm{V/mm}$, with a change of about $0.25\,\mathrm{V/mm}$ towards the end. (3) The third plot shows the average finite resistance measured across up to 7 different electrodes relative to ground. (4) The fourth plot shows measured motional dephasing on both in-plane radial modes. We observe a non-monotonic behavior in the measured motional dephasing times, which correlates with decreasing resistances toward the end of the treatment.

and $\omega_2/2\pi = 5.9(1)\,\mathrm{MHz}$) as a function of treatment duration to compare with other similar platforms. Consistent with other studies, we observe nonmonotonic behavior in the heating rates with respect to the treatment iteration, which is typically associated with the removal of adsorbed contaminants. Due to the lack of additional probing instruments for surface analysis, we have no information on the amount of carbon coverage or the presence of regions with varying work functions on our surface. We also observe a change in frequency scaling between the two in-plane modes, particularly for the motional mode ω_1, which is parallel to the projection plane of the sputtering gun. For a few iterations, we encountered difficulty cooling the lowest frequency mode, ω_1, to the near-ground state, estimating an upper bound of approximately 100 quanta/ms using the carrier contrast method. In the last few iterations, we observed a downward trend in overall noise, though it did not improve beyond the ambient noise levels measured prior to treatment attempts. Interestingly, the low-frequency motional mode has the lowest heating rate, resulting in a change in the frequency scaling factor β. Furthermore, the motional mode $\omega_3/2\pi \approx 5\,\mathrm{MHz}$, which undergoes indirect cooling, exhibits a heating rate four times higher than that of ω_1. However, we observe a factor of two discrepancies in the heating rates compared to other trapping sites, such as T_1. This discrepancy suggests that finite resistances at neighboring electrodes may play a role, requiring dedicated measurements and numerical analysis to accurately estimate changes in technical noise admittance and Johnson noise levels.

In conclusion, we investigated multiple factors that contributed to increased electric field noise near the trapped ion and evaluated their potential mitigation. Stray light levels, the micromotion minimization routine, and typical filtering components were found to be insufficient to fully account for the observed noise levels. Efforts to remove surface contaminants, such as carbon and diffused atoms, using argon-ion sputtering demonstrated effective targeting of the triangular array by the sputtering beam. However, despite systematic sputtering iterations, we did not reproduce the reduced noise levels reported in NIST experiments utilizing micrometer thick gold layers [120]. The 50 nm thin gold layers and composite metal structures in our traps may introduce additional factors that contribute to these discrepancies. Furthermore, the electric field noise behavior as a function of sputtering raises questions regarding surface modifications and the influence of nearby dielectric materials. Future investigations incorporating advanced techniques such as SEM imaging or Kelvin probe measurements [133] could provide valuable information on surface composition and charge dynamics, helping to develop improved noise mitigation strategies.

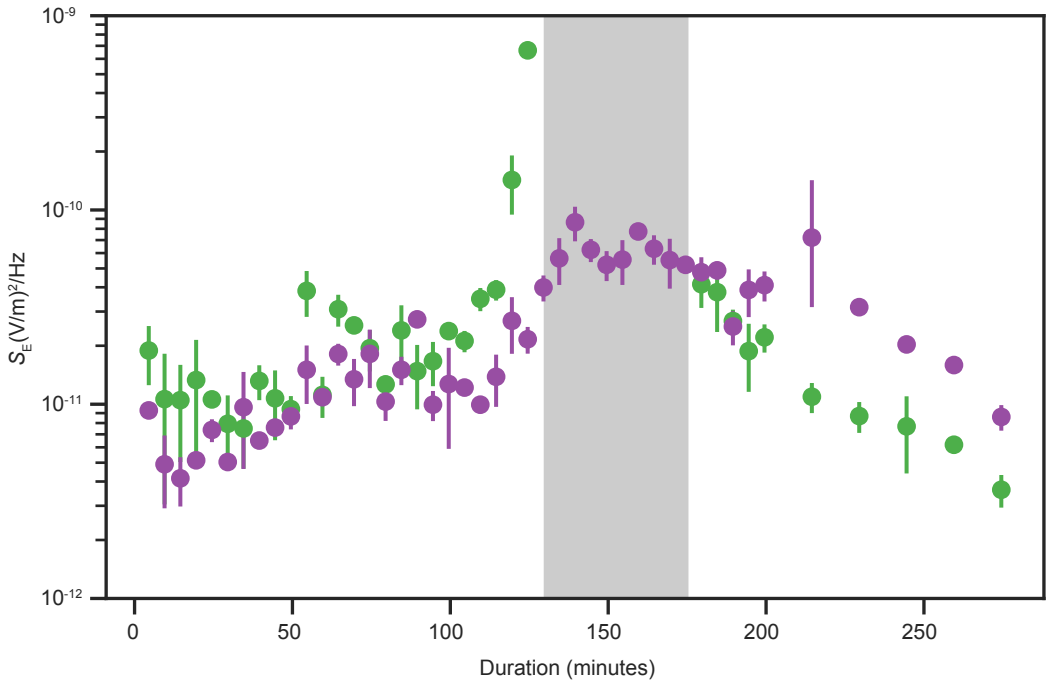

Figure 56: Electric field noise spectral density of two in-plane modes at T_2 (ω_1(Green) and ω_2(Purple)) with respect to treatment duration. After every treatment iteration, we tune in-plane motional modes to $\omega_1/2\pi = 3.7(1)$ and $\omega_2/2\pi = 5.9(1)$ MHz to ensure comparable configuration for measuring heating rates. Plot shows non-monotonic behaviour similar to Hite et al [133, 134] as a function of treatment duration. For about 9 iterations(Gray shaded), we had difficulties in near-ground-state cooling, of the lowest frequency mode. We observe no further improvement, except changed frequency scaling β, where ω_1 has lowest heating rate of all motional modes.

5 Discussion

Hakelberg [44], Kiefer [45], Kalis [43], and Mielenz [42] et al. laid the foundation for the 2D trapped-ion array toolbox, enabling individual control of microsites, 2D inter-site coupling via dipole-dipole interactions, and control over the direction of phonons in a 2D array. Building on this foundation, we extend the trapped-ion array platform toward a modular and extendable quantum network architecture. This intra-site coupling capability, a key requirement for scalable quantum networks, allows precise control over phonon-mediated interactions at the node level, enabling dynamic and reconfigurable information transfer. By introducing intra-site coupling using individual control techniques, we achieve coupling across all motional degrees of freedom at a single site, with maximum rates of approximately 10 kHz. Additionally, we provide access to a motional mode with weak direct coupling to the current laser beam configuration. This advancement introduces dynamic control over the directionality of the phonons: instead of adiabatically tuning the motional parameters [44, 45], we prepare motional modes (within 100 μs) to precisely steer the phonons in the desired direction. This method enables indirect cooling, achieving the 3D motional ground state in approximately 5 ms. Beyond enhancing control within single site, intra-site coupling lays the groundwork for flexible phonon-mediated information routing within a quantum network. Using this technique, we can generate multimode squeezing within a single site, which can significantly enhance sensitivity in metrology applications [98, 102, 144]. This technique not only complements inter-site dipole-dipole interactions but also facilitates photonic analogies, such as exploring the bosonic characteristics of phonons [101, 145] and extending them across multiple sites, analogous to a photonic chip [146]. These developments position trapped-ion arrays as flexible quantum network prototypes with modular intra- and inter-site connectivity.

Using the three triangular sites in the lowest layer and the hub approximately 10 μm above in the second layer, we demonstrate inter-site transport across this 2D+ array. Using control electronics, we achieve adiabatic transport with waveform execution durations ranging from 0.1 to 1 ms, resulting in a transport speed of $0.25\,\mathrm{m/s}$. With our protocol, we achieve a transport success rate of 0.99999 between trapping sites, limited primarily by background gas collisions. During transport, we observe the preservation of electronic fiducial states, verified through Ramsey spectroscopy, with decoherence attributed mainly to background effects. This capability introduces a crucial and flexible feature to the concept of a quantum network, where ions serve as nodes interconnected by deterministic state transfer. The ability to transport ions with negligible disturbance to their quantum states highlights the robustness, scalability, and suitability of the platform for distributed quantum information processing. For motional states, we estimate motional mode heating of less than 150 quanta per transport execution. We characterize

probable causes, including the ion transport speed, RF noise due to nonuniform gradients, and sampling noise. Using current state-of-the-art electronics [53] and optimized control potential configurations, we propose to enable diabatic transport in a trapped-ion array [114], significantly increasing the speed of transport while maintaining state fidelity. Together, intra-site phonon control, inter-site transport, and previously demonstrated inter-site phonon interactions demonstrate the versatility of trapped-ion arrays as modular quantum network prototypes capable of supporting both local and long-range quantum information transfer.

Additionally, we demonstrate multiple-ion transport capabilities, including redistribution and reordering, enabling the rapid initialization of desired trapped-ion array configurations within a few seconds, utilizing ablation loading techniques [49]. One such configuration, a pyramidal arrangement, can serve as a foundation for enabling multi-dimensional inter-site coupling. By leveraging individual trapping sites as close as 15 μm, we can engineer coupling rates at least five times higher than current decoherence levels, facilitating inter-site interactions near the single-constituent level. This performance is comparable to the triangular array at NIST, which operates at inter-site distances of 30 μm in a cryogenic environment to explore quantum-level physics [147]. In contrast, other similar works with larger inter-site distances exceeding 50 μm [148–151] rely on cryogenic conditions to mitigate motional heating and compensate for lower interaction strengths. Moreover, alternative approaches, such as the micro-Penning trap array [28] and modular platforms that address transport capabilities [141], require a significantly larger footprint for scaling. In our platform, the combination of close inter-site spacing and precise individual control enables the realization of a smaller loop area with three closely spaced trapping sites. This unique feature provides a promising framework for verifying Aharonov-Bohm physics under synthetic gauge fields [152]. These results extend the utility of trapped-ion arrays as versatile platforms for exploring quantum phenomena and implementing modular quantum networks.

The realization of our trapped-ion array-based quantum network architecture relies on robust quantum state engineering, interaction, and transfer, all of which are critically impacted by motional heating. The current ambient motional decoherence rate, approximately $1\,\text{quanta/ms}$ ($S_\text{E} \approx 10^{-11}\,\text{V/m}^2/\text{Hz}$), limits single-phonon interactions due to its comparability with the inter-site coupling rate ($\approx 1\,\text{kHz}$). Through dedicated experiments on accessible control elements, we estimate the most conservative levels of electric field noise. Our current optical isolation suggests that the upper bound of stray light-induced motional decoherence is two orders of magnitude below ambient decoherence rates. Noise near the secular frequency, caused by control elements accessing RF and control electrodes, is estimated to be three orders of magnitude lower than the ambient heating rate. In the case of RF noise-induced decoherence, we are currently limited by our gradient minimization routine. With coherent excitation via modulation of RF electrodes, we can minimize gradients with single motional quanta precision. Using squeez-

ing operations (modulating at twice the secular frequency) instead of coherent excitation, we can amplify the signal for improved gradient minimization [103, 153, 154]. To mitigate motional decoherence due to surface abnormalities, we utilized an in situ argon-ion treatment technique with a modified UHV chamber. With iterative energy dosages of $\approx 0.07\,\mathrm{J/cm^2}$, we track the relevant motional mode parameters and the heating rates of two in-plane modes of a trapping site. As evidence of changes in the local electrode surface, we observe non-monotonous behavior in heating rates and changes in frequency scaling, similar to the findings of Hite et al. [133]. However, we observe discrepancies in the heating rate at different trapping sites, with variations of up to a factor of 2 to 4, without further improvement. We hypothesize that these discrepancies arise due to the 50 nm thin top layer of gold and the multi-material fabrication process, which increases the likelihood of diffusion of elements such as aluminum into the trapping surface during the argon-ion treatment. Notably, this treatment has so far not been successful in traps with gold thicknesses below a micrometer, because thinner layers appear to be more susceptible to ion-induced damage and diffusion effects. Additionally, we measure the build-up of finite resistance between control electrodes and ground, likely due to sputtering and re-deposition of material. After an accumulated energy dosage of $\approx 3\,\mathrm{J/cm^2}$, we observe a higher rate of motional dephasing, indicating probable changes in the RF electrode. To conclude, we need to perform ex situ analysis under SEM/EDX to confirm the characteristic impact of the argon treatment, such as the formation of periodic structures due to the impact of ions and the presence of diffuse elements [133]. Alternatively, we could bypass all thermally activated noise sources using a cryogenic environment, which also ensures lower background gas pressure (currently $\approx 10^{-9}\,\mathrm{Pa}$), leading to extended ion storage times, from days to months. In a similar triangular array operated in a cryogenic environment, the electric field noise spectral density has been measured to be as low as $10^{-13}\,(\mathrm{V/m})^2/\mathrm{Hz}$ [147]. Such conditions could enable single-quanta-level inter-site interactions to study phonon-mediated spin-spin interactions [155] or utilize motional modes for quantum information processing [147]. To further investigate noise caused by different surface processes, we could employ optically trapped ions [156–159], which would avoid any micro-motion induced by RF.

The trapped-ion array demonstrated in this work represents a versatile and extendable platform for quantum networks, combining high-fidelity, multi-dimensional connectivity, and precise control over quantum degrees of freedom. By leveraging multidimensional trapped-ion configurations with access to all motional modes at individual sites, we can achieve multidimensional coupling, a key step toward realizing distributed nodes for quantum processing and secure quantum communication. These capabilities enable the exploration of quantum simulation experiments addressing multidimensional condensed matter physics, such as the simulation of bilayered materials [34]. While challenges remain, such as further reducing motional heating and ensuring robust entanglement distribution, this work establishes essential building blocks for extendable quantum networks. The demonstrated techniques offer a pathway

to integrate trapped-ion systems into larger-scale architectures, including future applications like quantum repeater nodes for long-distance communication and hybrid systems that combine ions with photonic [23] or superconducting platforms [47]. Looking ahead, this prototype trapped-ion quantum network, supported by current advancements in trapped-ion technology, lays the groundwork for a fully functional multidimensional quantum system. Combining tools such as assisted ion loading with precooled sources [160, 161], stabilized control fields [48, 97, 98, 162], integrated laser-less manipulation [163–166], broadband cooling across the array [82, 167], and integrated detection systems [117, 168], this platform provides a comprehensive toolbox for exploring high-dimensional quantum phenomena and simulating complex many-body physics [36, 169]. Altogether, this work positions trapped-ion arrays as a cornerstone technology for scalable, multi-dimensional quantum networks, advancing the field toward fully operational, large-scale quantum systems.

A Triangular array details

Current PDQ status(Valid until 08.2024)

PDQ Ch	Electrode	PAD	D-SUB feedthru(AnlageH)
00	1	81	X1-14
01	2	82	X1-16
02	3	83	X1-15
03	4	84	X1-3
04	5	85	X1-2
05	6	86	X1-1
06	7	92	X2-16
30	8	93	X2-2
07	9	94	X2-3
08	A	95	X2-1
10	11	6	X2-4
11	12	7	X2-17
12	13	8	X2-5
13	14	9	X2-19
14	15	10	X2-18
15	16	11	X2-6
16	17	17	X2-20
31	18	18	X2-9
17	19	19	X2-22
18	1A	20	X2-10
20	21	31	X2-13
21	22	32	X2-11
22	23	33	X2-12
23	24	34	X2-23
24	25	35	X2-24
25	26	36	X2-25
26	27	42	X1-11
32	28	43	X1-24
27	29	44	X1-23
28	2A	45	X1-25
	RF	89	
	RFGnd	87	X1-7
37	Mask		X2-7

Table 10: Triangle in AnlageH. This table gives an overview of DC and RF electrodes connections to the chip-carrier and all the way through feedthrough D-sub connections, adapter boards to AWG used as DDS, transport and DAC purposes since early 2022.

Inter-site transport

Table.11 gives all six used control potential configurations for ion loading at the hub, transport to other three trapping site, and for pyramidal configuration.

Table 11: Voltages (V) applied to electrodes for dedicated Φ_C. Our AWG has a discretization limit at 3×10^{-4} V (for each channel), and provides voltages in the range of [-10,10] V.

Electrodes	Φ_0	Φ_1	Φ_2	Φ_H	Φ_{HL}	$\Phi_{Pyramid}$
el1	0.0959	0.0959	0.0959	0.0959	-0.0038	0.0959
el2	-0.1676	-0.1676	-0.1676	-0.1676	0.1484	-0.1676
el3	-0.2760	-0.2760	-0.2760	-0.2760	-0.1484	-0.2760
el4	0.2328	0.2328	0.2328	0.2328	0.1484	0.2328
el5	-0.1246	-0.1246	-0.1246	-0.0246	0.0870	-0.1246
el6	0.1520	0.1520	0.1520	0.1520	-0.1484	0.1520
el7	-0.5683	-0.5683	-0.5683	-0.5683	-0.1484	-0.5683
el8	0.3005	0.3005	0.3005	0.3005	-0.0094	0.3005
el9	-0.4945	-0.4945	-0.4945	-0.4945	-0.1484	-0.4945
el10	-0.4502	-0.4502	-0.4502	-0.4502	-0.0641	-0.4502
el11	0.7980	0.7980	0.7980	0.7980	0.1484	0.7980
el12	0.1130	0.1130	0.1130	0.1130	0.1484	0.1130
el13	0.0327	0.0327	0.0327	0.0327	0.1484	0.0327
el14	-0.1239	-0.3239	-0.1239	-0.1239	0.1484	-0.3239
el15	0.0007	0.0007	0.0007	0.0007	-0.0387	0.0007
el16	0.6000	0.6000	0.6000	0.6000	-0.1484	0.6000
el17	0.0064	0.0064	0.0064	0.0064	-0.1484	0.0064
el18	-0.6718	-0.6718	-0.6718	-0.6718	-0.1484	-0.6718
el19	-0.3833	-0.3833	-0.3833	-0.3833	-0.1484	-0.3833
el20	-0.0137	-0.0137	-0.0137	-0.0137	-0.1484	-0.0137
el21	0.1892	-0.1108	-0.1108	-0.1108	-0.1484	0.1892
el22	-0.1364	-0.1364	-0.1364	-0.1364	0.0671	-0.1364
el23	0.5604	0.5604	0.2604	0.5604	0.1484	0.2604
el24	-0.1949	-0.1949	-0.1949	-0.1949	-0.1111	-0.1949
el25	0.4670	0.4670	0.4670	0.4670	-0.1484	0.4670
el26	-0.4358	-0.4358	-0.4358	-0.4358	0.0103	-0.4358
el27	0.1844	0.1844	0.1844	0.1844	0.1484	0.1844
el28	0.3901	0.3901	0.3901	0.3901	0.1484	0.3901
el29	-0.6760	-0.6760	-0.6760	-0.6760	-0.1484	-0.6760
el30	-0.6392	-0.6392	-0.6392	-0.6392	-0.1484	-0.6392
Metal sheet	-3.5000	-3.5000	-3.5000	-3.5000	-2.7000	-3.5000

Characteristic distances of embedded electrodes

To estimate characteristic distance, we use electrode package[123], to estimate resultant electric field at pseudo-potential minima, as a function of biasing each control electrode. Table.12 gives characteristic distances of all control electrodes(in units of mm) from calculated position of T_2, along X.Y.Z directions. During estimation of electric field noise spectral density S_E, we consider uncorrelated noise in all these electrodes.

Table 12: Calculated characteristic distances of electrodes w.r.t T_2 trapped site

Electrodes	**X**	**Y**	**Z**
1	5.7	14.9	5.8
2	6.2	6.6	4.9
3	22.3	2.0	6.6
4	8.4	3.0	24.4
5	5.2	4.2	29.8
6	4.9	6.7	21.7
7	5.5	13.5	15.9
8	4.9	37.0	7.8
9	6.5	45.7	16.3
10	5.9	32.0	8.5
11	5.9	32.6	8.5
12	6.5	46.4	16.2
13	4.9	37.2	7.8
14	5.5	13.5	15.9
15	4.9	6.7	21.7
16	5.2	4.1	30.1
17	8.4	3.0	24.6
18	22.2	2.0	6.6
19	6.2	6.6	4.9
20	5.7	15.1	5.8
21	6.1	23.6	3.0
22	7.8	6.2	2.7
23	3.5	1.7	8.3
24	1.7	1.8	4.1
25	1.1	3.6	1.7
26	1.1	3.6	1.7
27	1.8	1.8	4.1
28	3.5	1.7	8.3
29	7.8	6.2	2.7
30	6.1	23.0	3.0

B Argon-ion Sputtering

We calibrate all required components for performing argon-ion sputtering on a surface electrode trap using a dummy target with large segmented pieces of oxygen-free copper glued on to the chip-carrier, as shown in Fig.57. To perform benchmark sputtering-gun, we connect those glued metal plate to D-sub feed-through via chip-carrier pads with conductive glue. By measuring current pickup from the metal plates Fig.57 a) and b), we plot measured current as a function of filament current setting, and compare with anode monitor(in-built circuitry, part of the controller). Fig.57 b) shows the Mask(Top metal) plate with two apertures: Larger(for imaging optics) and smaller(for guiding Argon ion beam) to the trap. We observe a visible change in color, due to removal of about 1 μm of Gold as a result of Argon sputtering. Fig.58 shows four plots corresponding to using Filament 1 and 2 of the sputter gun. Top plots represents current measurements using shunt resistor (1 MOhm) connected in parallel to the dummy target, and Mask. Whereas, bottom plots shows anode monitor readings. We utilize these measurements as a look-up table while iterative treatements on surface-electrode traps.

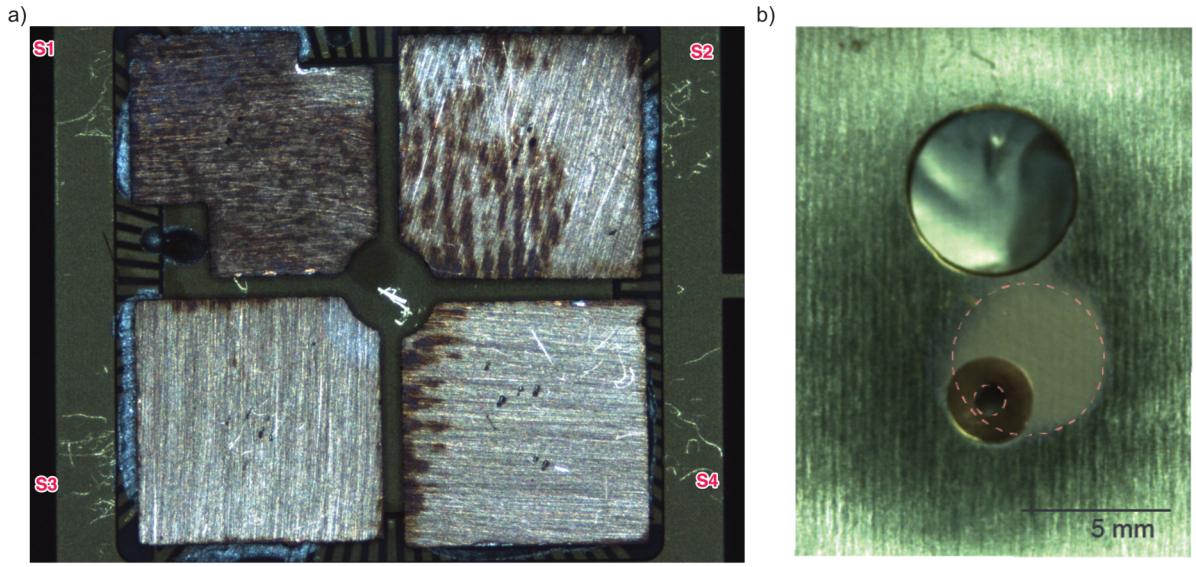

Figure 57: Calibration of Argon-gun parameters with segmented metal plates on the chip-socket and mask. 4 segmented metal plates were glued onto the chip-carrier with insulation from the bottom gold layer with peek spacers. These 4 segments were connected to dedicated pads of the chip carrier with conducting glue. All exposed metal parts are connected to data acquisition systems for monitoring currents in different parts of the dummy trap.

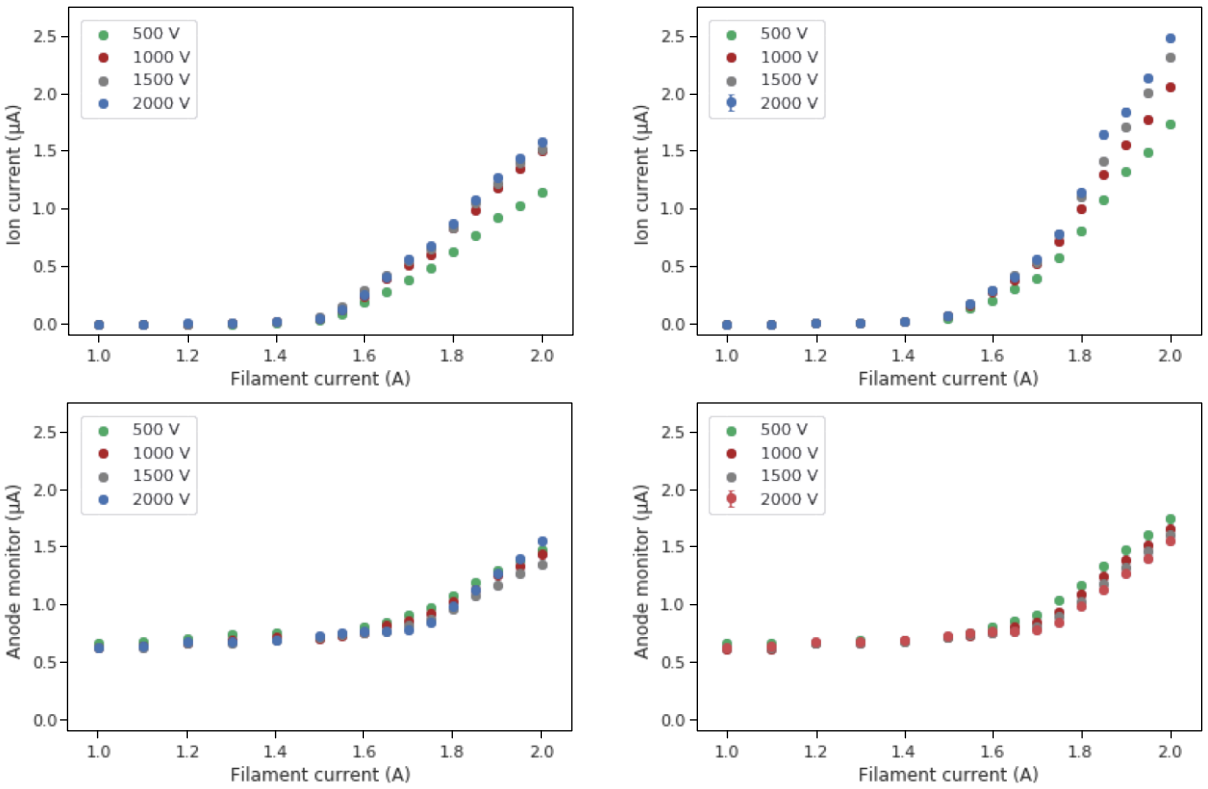

Figure 58: Sputtering gun calibration. Top Left plot shows ion current from Filament 1, measured by a cover plane at a working distance connected with a shunt resistor for different acceleration voltages(500-2 kV) for a fixed focus voltage (einzel lens) of 80%, similarly Top Right plot shows Filament 2 ion current. We observe it to be about 20% higher than Filament 1. And bottom left and right plots are corresponding anode monitors, which are integrated circuit (part of the controller) to measure ion current output. We observe a noise floor of about 0.6 μA.

C ARTIQ: Enhanced experimental control framework

Our current real-time control architecture is outdated and not widely used across the community, despite our hardware being capable of handling real-time control experiments. The scalability and on-demand interfacing of newer hardware are labor-intensive, requiring significant effort to integrate and manage. This presents a challenge for the group as advancements in hardware continue to outpace the development of compatible control systems, hindering progress and innovation.

Figure 59: UniFreiburg-Bermuda Variant. From left, I) Kasli, II) Urukul v1.3, III) Urukul v1.5, IV) DIO - TTL 4 inputs, 4 outputs, V),VI) DIO - TTL all outputs, VII) ADC - Sampler, VIII) DAC - Fastino.

The proposed UniFreiburg ARTIQ offers a hardware-agnostic layer that enables clients and users to interface with new hardware, devices, or services on-demand with minimal programming effort. The proposed data management system can benefit experts across various fields by allowing them to access and analyze data for multiple purposes, as highlighted by Bourdeauducq (2016)[53]. This layer can help visualize various parameters over demanded timeframes with less effort, aiding in the quick restructuring and analysis of data. Additionally, new clients may be able to understand and get started much faster, facilitating smoother integration and faster adoption of new technologies.

For example, upcoming trap-chips such as HOA[52], with nealy 100 control electrodes, and options for transporting requires real-time control electronics. With proposed upgrade, we currently equipped our experimental control with sinara hardware controlled via ARTIQ over

our pulse sequencer. By interfacing services such as Camera handler, Database and so-on, we can semi-automate multiple services such as automated reloading, and typical calibration sequences. So far interfaced components of this new experimental control includes:

1. Kasli V1.2(replacing Pulse sequencer).
2. Urukul v1.3 (Utilizing two EEMS, Clk from Kasli + Synced channels).
3. Urukul v1.5 (single EEM interfaced).
4. DIO (3x) (4 inputs + 20 outputs).
5. Sampler (8 Channel ADC, Single EEM interfaced)
6. Fastino (32 Channel, can be updated simultaneously)
7. 72 Channel AWG(PDQ)
8. InflxuDB
9. EMCCD Camera
10. Wavemeter services

For details, please visit group wiki pages to gain access to corresponding device related programs.

Acknowledgement

I thank Prof. Dr. Tobias Schaetz, for giving me the opportunity to do Doctoral thesis in Atomic, Molecular, and optical physics lab at the institute of Physics, University of Freiburg, and for scientific guidance.
I thank Dr. Ulrich Warring for supporting with everything related to surface-electrode trap, atomic physics, lab and numerical analysis.
I thank Joern Denter, for Laser support, lab and safety support.
I thank Helga Mueller, for taking care of paperwork, and dealing with Rektorat.
I thank Dr. Philip Kiefer for support during Argon-ion treatments, execution of experiment, maintenance of doubling cavity, and VECSEL design.
I thank Dr. Leon Karpa, for providing an opportunity to work in EIT project.
I thank Dr. Frederick Boeckling(Hakelberg), for UHV support.
I thank Dr. Matthias Wittemer for PDQ support.
I thank Jan-Philipp Schroeder for programming support.
I thank Florian Hasse, for lab maintenance, giving valuable experimental inputs, and for unwavering support during whole PhD program.
I thank Lennart Guth, for VECSEL commissioning, and unwavering support.
I thank Robin Thomm for programming, numerical analysis discussions, and ARTIQ related discussions.
I thank Fabian Thielemann for scientific, and experimental control related discussions.
I thank Dr. Daniel von Schoefeld, for PID lock server, and many helpful electronics-related discussions.
I thank Dr. Thomas Walker, and Dr. Amir Mohammadi, for experiment and many physics related discussions.
I thank Wei Wu, Apurba Das, and Joachim Siemund for cheerful discussion unrelated to ions, mostly about neutral atoms, NV centers, or databases etc.
I thank Ole Pikkemat, and Sara Schell for new experimental design works, and bench-marking experiments.
I thank Leon Goepert, for Argon-treatment support, and for bench-marking experiments.
I thank Lucas Eisenhart for preparation towards HOA trap commissioning.
I thank Fredrike Dorr, Andreas Weber, and Igor Z. for taking care of loose-ends.
I thank Dr. Pascal Weckesser, Dr. Julian Schmidt, and Dr. Markus Debatin for many helpful discussion during early research days.
I thank Sebastian Schnell, and Yannick Minet, for many helpful discussions during early research days.
I thank Dr. Manuel Mielenz, Dr. Henning Kalis, Leonard Nitzsche, and Valentin vierhub-

lorenz for recording all valuable experimental information via their documents.
I thank Dr. Ralf Thomann, for SEM/EDX support.
I thank Dr. Dustin Hite for Argon-treatment related valuable information.
I thank Dr. Dietrich Leibfried for many valuable discussions.
I thank Prof.Dr. Hartmud Haeffner, for sharing the dataset of heating rate measurements, and valuable discussion related to Argon-ion treatments.
I thank Dr. Kambiz Mahboubi, and team for Electronic workshop support.
I thank Grossman, and team for Mechanical workshop support.
Last but not least, I thank my family(mom, dad, and my wife) for unwavering support throughout the journey.
I thank my friends in India, Germany, UK and other parts of the world, for unwavering support during this journey.

Bibliography

[1] Richard P. Feynman. "Simulating physics with computers". In: *International Journal of Theoretical Physics* 21 (6-7 June 1982), pp. 467–488. ISSN: 0020-7748. DOI: 10.1007/BF02650179.

[2] H. J. Kimble. "The quantum internet". In: *Nature* 453 (2008), pp. 1023–1030. DOI: 10.1038/nature07127. URL: https://www.nature.com/articles/nature07127.

[3] David P. DiVincenzo. "The Physical Implementation of Quantum Computation". In: *Fortschritte der Physik* 48 (9-11 Sept. 2000), pp. 771–783. ISSN: 00158208. DOI: 10.1002/1521-3978(200009)48:9/11<771::AID-PROP771>3.0.CO;2-E.

[4] J. Ignacio Cirac and Peter Zoller. "Goals and opportunities in quantum simulation". In: *Nature Physics* 8 (4 Apr. 2012), pp. 264–266. ISSN: 1745-2473. DOI: 10.1038/nphys2275.

[5] I.M. Georgescu, S. Ashhab, and Franco Nori. "Quantum simulation". In: *Reviews of Modern Physics* 86 (1 Mar. 2014), pp. 153–185. ISSN: 0034-6861. DOI: 10.1103/RevModPhys.86.153.

[6] Pieter Kok et al. "Linear optical quantum computing with photonic qubits". In: *Rev. Mod. Phys.* 79 (1 Jan. 2007), pp. 135–174. DOI: 10.1103/RevModPhys.79.135. URL: https://link.aps.org/doi/10.1103/RevModPhys.79.135.

[7] Pai Peng, Clemens Matthiesen, and Hartmut Häffner. "Spin readout of trapped electron qubits". In: *Phys. Rev. A* 95 (1 Jan. 2017), p. 012312. DOI: 10.1103/PhysRevA.95.012312. URL: https://link.aps.org/doi/10.1103/PhysRevA.95.012312.

[8] Alexandre Blais et al. "Circuit quantum electrodynamics". In: *Rev. Mod. Phys.* 93 (2 May 2021), p. 025005. DOI: 10.1103/RevModPhys.93.025005. URL: https://link.aps.org/doi/10.1103/RevModPhys.93.025005.

[9] Justyna P. Zwolak and Jacob M. Taylor. "Colloquium: Advances in automation of quantum dot devices control". In: *Rev. Mod. Phys.* 95 (1 Feb. 2023), p. 011006. DOI: 10.1103/RevModPhys.95.011006. URL: https://link.aps.org/doi/10.1103/RevModPhys.95.011006.

[10] Daniel Barredo et al. "Synthetic three-dimensional atomic structures assembled atom by atom". In: *Nature* 561 (7721 Sept. 2018), pp. 79–82. ISSN: 0028-0836. DOI: 10.1038/s41586-018-0450-2.

[11] Tobias Bothwell et al. "Resolving the gravitational redshift across a millimetre-scale atomic sample". In: *Nature* 602.7897 (2022), pp. 420–424. DOI: 10.1038/s41586-021-04349-7. URL: https://doi.org/10.1038/s41586-021-04349-7.

[12] A. González-Tudela and J. I. Cirac. "Cold atoms in twisted-bilayer optical potentials". In: *Phys. Rev. A* 100 (5 Nov. 2019), p. 053604. DOI: 10.1103/PhysRevA.100.053604. URL: https://link.aps.org/doi/10.1103/PhysRevA.100.053604.

[13] Zengming Meng et al. "Atomic Bose–Einstein condensate in twisted-bilayer optical lattices". In: *Nature* 615.7951 (2023), pp. 231–236. DOI: 10.1038/s41586-023-05695-4. URL: https://doi.org/10.1038/s41586-023-05695-4.

[14] S. M. Brewer et al. "$^{27}Al^{+}$ Quantum-Logic Clock with a Systematic Uncertainty below 10^{-18}". In: *Phys. Rev. Lett.* 123 (3 July 2019), p. 033201. DOI: 10.1103/PhysRevLett.123.033201. URL: https://link.aps.org/doi/10.1103/PhysRevLett.123.033201.

[15] David J Wineland et al. “Experimental Issues in Coherent Quantum-State Manipulation of Trapped Atomic Ions”. In: *J. Res. Natl. Inst. Stand. Tech.* 103 (1998), p. 259.

[16] D. Leibfried et al. “Quantum Dynamics of Single Trapped Ions”. In: *Rev. Mod. Phys.* 75.1 (Mar. 2003), pp. 281–324. DOI: 10.1103/RevModPhys.75.281.

[17] Fabian Wolf et al. “Motional Fock states for quantum-enhanced amplitude and phase measurements with trapped ions”. In: *Nature Communications* 10 (1 July 2019), p. 2929. ISSN: 2041-1723. DOI: 10.1038/s41467-019-10576-4.

[18] Alessandra Colla and Heinz-Peter Breuer. “Open-system approach to nonequilibrium quantum thermodynamics at arbitrary coupling”. In: *Phys. Rev. A* 105 (5 May 2022), p. 052216. DOI: 10.1103/PhysRevA.105.052216. URL: https://link.aps.org/doi/10.1103/PhysRevA.105.052216.

[19] Yu Liu et al. “Quantum state tracking and control of a single molecular ion in a thermal environment”. In: *Science* 385 (6710 Aug. 2024), pp. 790–795. ISSN: 0036-8075. DOI: 10.1126/science.ado1001.

[20] C. Will et al. “Image-Current Mediated Sympathetic Laser Cooling of a Single Proton in a Penning Trap Down to 170 mK Axial Temperature”. In: *Phys. Rev. Lett.* 133 (2 July 2024), p. 023002. DOI: 10.1103/PhysRevLett.133.023002. URL: https://link.aps.org/doi/10.1103/PhysRevLett.133.023002.

[21] P. Micke et al. “Coherent laser spectroscopy of highly charged ions using quantum logic”. In: *Nature* 578 (7793 Feb. 2020), pp. 60–65. ISSN: 0028-0836. DOI: 10.1038/s41586-020-1959-8.

[22] Pascal Weckesser et al. “Observation of Feshbach resonances between a single ion and ultracold atoms”. In: *Nature* 600 (7889 Dec. 2021), pp. 429–433. ISSN: 0028-0836. DOI: 10.1038/s41586-021-04112-y.

[23] C. Monroe et al. “Large-scale modular quantum-computer architecture with atomic memory and photonic interconnects”. In: *Phys. Rev. A* 89 (2 Feb. 2014), p. 022317. DOI: 10.1103/PhysRevA.89.022317. URL: https://link.aps.org/doi/10.1103/PhysRevA.89.022317.

[24] C. Monroe et al. “Programmable quantum simulations of spin systems with trapped ions”. In: *Rev. Mod. Phys.* 93 (2 Apr. 2021), p. 025001. DOI: 10.1103/RevModPhys.93.025001. URL: https://link.aps.org/doi/10.1103/RevModPhys.93.025001.

[25] A Bautista-Salvador et al. “Multilayer ion trap technology for scalable quantum computing and quantum simulation”. In: *New Journal of Physics* 21.4 (Apr. 2019), p. 043011. DOI: 10.1088/1367-2630/ab0e46. URL: https://dx.doi.org/10.1088/1367-2630/ab0e46.

[26] D. Kielpinski, C. Monroe, and D. J. Wineland. “Architecture for a large-scale ion-trap quantum computer”. In: *Nature* 417 (6890 June 2002), pp. 709–711. ISSN: 0028-0836. DOI: 10.1038/nature00784.

[27] J. M. Pino et al. “Demonstration of the trapped-ion quantum CCD computer architecture”. In: *Nature* 592 (7853 Apr. 2021), pp. 209–213. ISSN: 0028-0836. DOI: 10.1038/s41586-021-03318-4.

[28] Shreyans Jain et al. “Penning micro-trap for quantum computing”. In: *Nature* 627 (8004 Mar. 2024), pp. 510–514. ISSN: 0028-0836. DOI: 10.1038/s41586-024-07111-x.

[29] Florian Kranzl et al. “Controlling long ion strings for quantum simulation and precision measurements”. In: *Phys. Rev. A* 105 (5 May 2022), p. 052426. DOI: 10.1103/PhysRevA.105.052426. URL: https://link.aps.org/doi/10.1103/PhysRevA.105.052426.

[30] Dominik Kiesenhofer et al. “Controlling Two-Dimensional Coulomb Crystals of More Than 100 Ions in a Monolithic Radio-Frequency Trap”. In: *PRX Quantum* 4 (2 Apr. 2023), p. 020317. DOI: 10.1103/PRXQuantum.4.020317. URL: https://link.aps.org/doi/10.1103/PRXQuantum.4.020317.

[31] Marissa D’Onofrio et al. “Radial Two-Dimensional Ion Crystals in a Linear Paul Trap”. In: *Phys. Rev. Lett.* 127 (2 July 2021), p. 020503. DOI: 10.1103/PhysRevLett.127.020503. URL: https://link.aps.org/doi/10.1103/PhysRevLett.127.020503.

[32] M K Joshi et al. “Polarization-gradient cooling of 1D and 2D ion Coulomb crystals”. In: *New Journal of Physics* 22 (10 Oct. 2020), p. 103013. ISSN: 1367-2630. DOI: 10.1088/1367-2630/abb912.

[33] Anthony M. Polloreno, Ana Maria Rey, and John J. Bollinger. “Individual qubit addressing of rotating ion crystals in a Penning trap”. In: *Physical Review Research* 4 (3 July 2022), p. 033076. ISSN: 2643-1564. DOI: 10.1103/PhysRevResearch.4.033076.

[34] Samarth Hawaldar et al. “Bilayer Crystals of Trapped Ions for Quantum Information Processing”. In: *Phys. Rev. X* 14 (3 Aug. 2024), p. 031030. DOI: 10.1103/PhysRevX.14.031030. URL: https://link.aps.org/doi/10.1103/PhysRevX.14.031030.

[35] Tom Manovitz et al. “Quantum Simulations with Complex Geometries and Synthetic Gauge Fields in a Trapped Ion Chain”. In: *PRX Quantum* 1 (2 Oct. 2020), p. 020303. DOI: 10.1103/PRXQuantum.1.020303. URL: https://link.aps.org/doi/10.1103/PRXQuantum.1.020303.

[36] Ulrich Warring et al. “Trapped Ion Architecture for Multi-Dimensional Quantum Simulations”. In: *Advanced Quantum Technologies* 3 (11 Nov. 2020), p. 1900137. ISSN: 2511-9044. DOI: 10.1002/qute.201900137.

[37] Benedikt Fauseweh. “Quantum many-body simulations on digital quantum computers: State-of-the-art and future challenges”. In: *Nature Communications* 15 (1 Mar. 2024), p. 2123. ISSN: 2041-1723. DOI: 10.1038/s41467-024-46402-9.

[38] T. Schaetz et al. “Towards (scalable) quantum simulations in ion traps”. In: *Journal of Modern Optics* 54.16-17 (2007), pp. 2317–2325. DOI: 10.1080/09500340701639631. eprint: https://doi.org/10.1080/09500340701639631. URL: https://doi.org/10.1080/09500340701639631.

[39] K. R. Brown et al. “Coupled Quantized Mechanical Oscillators”. In: *Nature* 471.7337 (Mar. 2011), pp. 196–199. ISSN: 0028-0836, 1476-4687. DOI: 10.1038/nature09721.

[40] M. Harlander et al. “Trapped-Ion Antennae for the Transmission of Quantum Information”. In: *Nature* 471.7337 (Mar. 2011), pp. 200–203. ISSN: 0028-0836, 1476-4687. DOI: 10.1038/nature09800.

[41] Roman Schmied, Janus H. Wesenberg, and Dietrich Leibfried. “Optimal Surface-Electrode Trap Lattices for Quantum Simulation with Trapped Ions”. In: *Phys. Rev. Lett.* 102 (23 June 2009), p. 233002. DOI: 10.1103/PhysRevLett.102.233002. URL: https://link.aps.org/doi/10.1103/PhysRevLett.102.233002.

[42] Manuel Mielenz et al. “Arrays of individually controlled ions suitable for two-dimensional quantum simulations”. In: *Nature Communications* 7 (June 2016), p. 11839. URL: https://doi.org/10.1038/ncomms11839%20http://10.0.4.14/ncomms11839.

[43] Henning Kalis et al. “Motional-mode analysis of trapped ions”. In: *Phys. Rev. A* 94 (2 Aug. 2016), p. 023401. DOI: 10.1103/PhysRevA.94.023401. URL: https://link.aps.org/doi/10.1103/PhysRevA.94.023401.

[44] Frederick Hakelberg et al. "Interference in a Prototype of a Two-Dimensional Ion Trap Array Quantum Simulator". In: *Phys. Rev. Lett.* 123.10 (2019), p. 100504. ISSN: 0031-9007. DOI: 10.1103/physrevlett.123.100504. URL: https://doi.org/10.1103/PhysRevLett.123.100504.

[45] Philip Kiefer et al. "Floquet-Engineered Vibrational Dynamics in a Two-Dimensional Array of Trapped Ions". In: *Phys. Rev. Lett.* 123 (21 Nov. 2019), p. 213605. DOI: 10.1103/PhysRevLett.123.213605. URL: https://link.aps.org/doi/10.1103/PhysRevLett.123.213605.

[46] D Leibfried. "Could a boom in technologies trap {F}eynman's simulator?" In: *Nature* 463.7281 (2010), p. 608.

[47] D. De Motte et al. "Experimental system design for the integration of trapped-ion and superconducting qubit systems". In: *Quantum Information Processing* 15.12 (2016), pp. 5385–5414. DOI: 10.1007/s11128-016-1368-y. URL: https://link.springer.com/article/10.1007/s11128-016-1368-y.

[48] Frederick Hakelberg et al. "Hybrid setup for stable magnetic fields enabling robust quantum control". In: *Scientific Reports* 8 (1 2018), p. 4404. ISSN: 2045-2322. DOI: 10.1038/s41598-018-22671-5. URL: https://doi.org/10.1038/s41598-018-22671-5.

[49] Deviprasath Palani et al. "High-fidelity transport of trapped-ion qubits in a multilayer array". In: *Phys. Rev. A* 107 (5 May 2023), p. L050601. DOI: 10.1103/PhysRevA.107.L050601. URL: https://link.aps.org/doi/10.1103/PhysRevA.107.L050601.

[50] Dylan J Gorman et al. "Two-mode coupling in a single-ion oscillator via parametric resonance". In: *Phys. Rev. A* 89 (6 June 2014), p. 062332. DOI: 10.1103/PhysRevA.89.062332. URL: https://link.aps.org/doi/10.1103/PhysRevA.89.062332.

[51] Pan-Yu Hou et al. "Indirect Cooling of Weakly Coupled Trapped-Ion Mechanical Oscillators". In: *Phys. Rev. X* 14 (2 Apr. 2024), p. 021003. DOI: 10.1103/PhysRevX.14.021003. URL: https://link.aps.org/doi/10.1103/PhysRevX.14.021003.

[52] Peter Lukas Wilhelm Maunz. *High Optical Access Trap 2.0*. Technical Report SAND2016-1234. United States: Sandia National Laboratories, Jan. 2016. DOI: 10.2172/1237003. URL: https://www.osti.gov/biblio/1237003.

[53] *For example, the open source advanced real-time infrastructure for quantum physics experiments (ARTIQ) was initiated and developed by M-Labs in partnership with the Ion Storage Group at NIST/Boulder CO (USA), and is now used and supported by a growing number of research groups around the world [https://m-labs.hk/experiment-control/artiq].*

[54] D Palani, D Hoenig, and L Karpa. "In situ ac Stark shift detection in light storage spectroscopy". In: *Journal of Physics B: Atomic, Molecular and Optical Physics* 54.16 (Sept. 2021), p. 165402. DOI: 10.1088/1361-6455/ac2001. URL: https://dx.doi.org/10.1088/1361-6455/ac2001.

[55] P. Maunz and M. G. Blain. *Personal communication*. Personal communication. 2013.

[56] Henning Kalis. "Initialization of Quantum States in a Two-Dimensional Ion-Trap Array". PhD thesis. 2017.

[57] Roman Schmied, Janus H. Wesenberg, and Dietrich Leibfried. "Optimal Surface-Electrode Trap Lattices for Quantum Simulation with Trapped Ions". en. In: *Phys. Rev. Lett.* 102.23 (June 2009), p. 233002. ISSN: 0031-9007, 1079-7114. DOI: 10.1103/PhysRevLett.102.233002.

[58] Ch Schneider, D. Porras, and T. Schaetz. "Experimental Quantum Simulations of Many-Body Physics with Trapped Ions". In: *Rep. Prog. Phys.* 75.2 (2012), p. 024401.

[59] D T C Allcock et al. "Reduction of heating rate in a microfabricated ion trap by pulsed-laser cleaning". In: *New Journal of Physics* 13 (12 Dec. 2011), p. 123023. ISSN: 1367-2630. DOI: 10.1088/1367-2630/13/12/123023.

[60] G. R. Brady et al. "Integration of Fluorescence Collection Optics with a Microfabricated Surface Electrode Ion Trap". en. In: *Applied Physics B* 103.4 (June 2011), pp. 801–808. ISSN: 0946-2171, 1432-0649. DOI: 10.1007/s00340-011-4453-z.

[61] D. Stick et al. "Demonstration of a Microfabricated Surface Electrode Ion Trap". In: *arXiv preprint arXiv:1008.0990* (2010).

[62] Frederick Hakelberg. "Controlled inter-site coupling in a two-dimensional ion trap array". PhD thesis. University of Freiburg, 2019. DOI: 10.6094/UNIFR/151346.

[63] G. Clos et al. "Decoherence-Assisted Spectroscopy of a Single ${\mathrm{Mg}}{+}$ Ion". In: *Phys. Rev. Lett.* 112.11 (Mar. 2014), p. 113003. DOI: 10.1103/PhysRevLett.112.113003.

[64] M. Mielenz. "Two-Dimensional Arrays of Individually Controlled Ions". PhD thesis.

[65] Philip Kiefer. "Floquet engineering in a 2D array of trapped ions". PhD thesis. 2020.

[66] A. Friedenauer et al. "High Power All Solid State Laser System near 280 Nm". English. In: *Applied Physics B* 84.3 (2006), pp. 371–373. ISSN: 0946-2171. DOI: 10.1007/s00340-006-2274-2.

[67] S. C. Burd et al. "VECSEL Systems for the Generation and Manipulation of Trapped Magnesium Ions". en. In: *Optica* 3.12 (Dec. 2016), p. 1294. ISSN: 2334-2536. DOI: 10.1364/OPTICA.3.001294.

[68] S. C. Burd et al. "VECSEL systems for quantum information processing with trapped beryllium ions". In: *J. Opt. Soc. Am. B* 40.4 (Apr. 2023), pp. 773–781. DOI: 10.1364/JOSAB.475467. URL: https://opg.optica.org/josab/abstract.cfm?URI=josab-40-4-773.

[69] Lennart Guth. "Assembling and Benchmarking the Next Generation of Solid-State Laser Systems for Controlling Trapped Magnesium Ions". Department of Physics. Master's thesis. Freiburg, Germany: University of Freiburg, 2021.

[70] T. W. Hansch and B. Couillaud. "Laser Frequency Stabilization by Polarization Spectroscopy of a Reflecting Reference Cavity". In: *Optics Communications* 35.3 (1980), pp. 441–444. ISSN: 0030-4018. DOI: http://dx.doi.org/10.1016/0030-4018(80)90069-3.

[71] Wayne M. Itano and D. J. Wineland. "Precision measurement of the ground-state hyperfine constant of $^{25}Mg^{+}$". In: *Phys. Rev. A* 24 (3 Sept. 1981), pp. 1364–1373. DOI: 10.1103/PhysRevA.24.1364. URL: https://link.aps.org/doi/10.1103/PhysRevA.24.1364.

[72] G. Bradski. "The OpenCV Library". In: *Dr. Dobb's Journal of Software Tools* (2000).

[73] David Marr and Ellen Hildreth. "Theory of edge detection". In: *Proceedings of the Royal Society of London. Series B. Biological Sciences* 207.1167 (1980), pp. 187–217.

[74] W. Paul. "Electromagnetic Traps for Charged and Neutral Particles". In: *Nobel Lecture* (1989).

[75] Steven Diamond and Stephen Boyd. "CVXPY: A Python-Embedded Modeling Language for Convex Optimization". In: *Journal of Machine Learning Research* 17.83 (2016), pp. 1–5.

[76] J. H. Wesenberg. "Electrostatics of Surface-Electrode Ion Traps". In: *Phys. Rev. A* 78.6 (Dec. 2008), p. 063410. DOI: 10.1103/PhysRevA.78.063410.

[77] A. Friedenauer. "Simulation of the Quantum Ising Model in an Ion Trap". PhD thesis. Ludwigs-Maximilians-Universität München, 2010.

[78] W.D. Phillips. *Laser Cooling and Trapping of Neutral Atoms*. Published: Laser Manipulation of Atoms and Ions, Proceedings of the International School of Physics Enrico Fermi, Course CXVIII, Amsterdam. 1992.

[79] D. J. Wineland and Wayne M. Itano. "Laser Cooling of Atoms". In: *Phys. Rev. A* 20.4 (Oct. 1979), pp. 1521–1540.

[80] Christopher J. Foot. *Atomic Physics*. Oxford: Oxford University Press, 2005.

[81] C. Monroe et al. "Demonstration of a Fundamental Quantum Logic Gate". In: *Phys. Rev. Lett.* 75 (25 Dec. 1995), pp. 4714–4717. DOI: 10.1103/PhysRevLett.75.4714. URL: https://link.aps.org/doi/10.1103/PhysRevLett.75.4714.

[82] Giovanna Morigi, Jürgen Eschner, and Christoph H Keitel. "Ground State Laser Cooling Using Electromagnetically Induced Transparency". In: *Phys. Rev. Lett.* 85.21 (2000), p. 4458.

[83] D. J. Berkeland et al. "Minimization of ion micromotion in a Paul trap". In: *Journal of Applied Physics* 83.10 (May 1998), pp. 5025–5033. ISSN: 0021-8979. DOI: 10.1063/1.367318. eprint: https://pubs.aip.org/aip/jap/article-pdf/83/10/5025/18699946/5025_1_online.pdf. URL: https://doi.org/10.1063/1.367318.

[84] Wayne M. Itano and D. J. Wineland. "Precision measurement of the ground-state hyperfine constant of $^{25}Mg^{+}$". In: *Phys. Rev. A* 24 (3 Sept. 1981), pp. 1364–1373. DOI: 10.1103/PhysRevA.24.1364. URL: https://link.aps.org/doi/10.1103/PhysRevA.24.1364.

[85] Thomas Harty. *Atomic Physics*. Version 1.0.2. URL: https://github.com/OxfordIonTrapGroup/atomic_physics/.

[86] J.J. Sakurai and Jim Napolitano. *Modern Quantum Mechanics*. Addison-Wesley, 1994.

[87] Norman F. Ramsey. "Experiments with separated oscillatory fields and hydrogen masers". In: *Rev. Mod. Phys.* 62 (3 July 1990), pp. 541–552. DOI: 10.1103/RevModPhys.62.541. URL: https://link.aps.org/doi/10.1103/RevModPhys.62.541.

[88] Florian Hasse et al. "Phase-stable traveling waves stroboscopically matched for superresolved observation of trapped-ion dynamics". In: *Phys. Rev. A* 109 (5 May 2024), p. 053105. DOI: 10.1103/PhysRevA.109.053105. URL: https://link.aps.org/doi/10.1103/PhysRevA.109.053105.

[89] Matthias Wittemer. "Particle creation and memory effects in a trapped ion quantum simulator". Department of Physics. Ph.D. thesis. University of Freiburg, 2019.

[90] W M Itano et al. "Quantum Projection Noise: {{Population}} Fluctuations in Two-Level Systems". In: *Phys. Rev. A* 47.5 (1993), p. 3554. DOI: 10.1103/PhysRevA.47.3554.

[91] Robin Thomm. "State Detection of Trapped Magnesium Ions". Unpublished master's thesis. MA thesis. University of Freiburg, 2021.

[92] J.R. Johansson, P.D. Nation, and Franco Nori. "QuTiP 2: A Python framework for the dynamics of open quantum systems". In: *Computer Physics Communications* 184.4 (2013), pp. 1234–1240. ISSN: 0010-4655. DOI: https://doi.org/10.1016/j.cpc.2012.11.019. URL: https://www.sciencedirect.com/science/article/pii/S0010465512003955.

[93] Roy J. Glauber. "Coherent and Incoherent States of the Radiation Field". In: *Phys. Rev.* 131 (6 Sept. 1963), pp. 2766–2788. DOI: 10.1103/PhysRev.131.2766. URL: https://link.aps.org/doi/10.1103/PhysRev.131.2766.

[94] R. Tyler Sutherland et al. "One- and two-qubit gate infidelities due to motional errors in trapped ions and electrons". In: *Phys. Rev. A* 105 (2 Feb. 2022), p. 022437. DOI: 10.1103/PhysRevA.105.022437. URL: https://link.aps.org/doi/10.1103/PhysRevA.105.022437.

[95] I. Talukdar et al. "Implications of surface noise for the motional coherence of trapped ions". In: *Phys. Rev. A* 93 (4 Apr. 2016), p. 043415. DOI: 10.1103/PhysRevA.93.043415. URL: https://link.aps.org/doi/10.1103/PhysRevA.93.043415.

[96] D. Leibfried et al. "Experimental Determination of the Motional Quantum State of a Trapped Atom". In: *Phys. Rev. Lett.* 77 (21 Nov. 1996), pp. 4281–4285. DOI: 10.1103/PhysRevLett.77.4281. URL: https://link.aps.org/doi/10.1103/PhysRevLett.77.4281.

[97] K. G. Johnson et al. "Active Stabilization of Ion Trap Radiofrequency Potentials". en. In: *Review of Scientific Instruments* 87.5 (May 2016), p. 053110. ISSN: 0034-6748, 1089-7623. DOI: 10.1063/1.4948734.

[98] J. Metzner et al. "Two-mode squeezing and SU(1,1) interferometry with trapped ions". In: *Phys. Rev. A* 110 (2 Aug. 2024), p. 022613. DOI: 10.1103/PhysRevA.110.022613. URL: https://link.aps.org/doi/10.1103/PhysRevA.110.022613.

[99] R. J. Epstein et al. "Simplified Motional Heating Rate Measurements of Trapped Ions". en. In: *Physical Review A* 76.3 (Sept. 2007). ISSN: 1050-2947, 1094-1622. DOI: 10.1103/PhysRevA.76.033411.

[100] J. H. Wesenberg et al. "Fluorescence during Doppler cooling of a single trapped atom". In: *Physical Review A* 76 (5 2007). DOI: 10.1103/PhysRevA.76.053416.

[101] Kenji Toyoda et al. "Hong–Ou–Mandel interference of two phonons in trapped ions". In: *Nature* 527 (7576 Nov. 2015), pp. 74–77. ISSN: 0028-0836. DOI: 10.1038/nature15735.

[102] Yue Li et al. "Multi-parameter quantum metrology with stabilized multi-mode squeezed state". In: (Dec. 2023).

[103] Matthias Wittemer et al. "Phonon Pair Creation by Inflating Quantum Fluctuations in an Ion Trap". In: *Phys. Rev. Lett.* 123.18 (2019), p. 180502. ISSN: 10797114. DOI: 10.1103/PhysRevLett.123.180502. arXiv: 1903.05523. URL: https://doi.org/10.1103/PhysRevLett.123.180502.

[104] S. C. Burd et al. "Quantum Amplification of Mechanical Oscillator Motion". en. In: *Science* 364.6446 (June 2019), pp. 1163–1165. ISSN: 0036-8075, 1095-9203. DOI: 10.1126/science.aaw2884.

[105] C. F. Roos et al. "Nonlinear coupling of continuous variables at the single quantum level". In: *Phys. Rev. A* 77 (4 Apr. 2008), p. 040302. DOI: 10.1103/PhysRevA.77.040302. URL: https://link.aps.org/doi/10.1103/PhysRevA.77.040302.

[106] Shiqian Ding et al. "Cross-Kerr Nonlinearity for Phonon Counting". In: *Phys. Rev. Lett.* 119 (19 Nov. 2017), p. 193602. DOI: 10.1103/PhysRevLett.119.193602. URL: https://link.aps.org/doi/10.1103/PhysRevLett.119.193602.

[107] David R. Leibrandt et al. "Laser ablation loading of a surface-electrode ion trap". In: *Phys. Rev. A* 76 (5 Nov. 2007), p. 055403. DOI: 10.1103/PhysRevA.76.055403. URL: https://link.aps.org/doi/10.1103/PhysRevA.76.055403.

[108] K. Zimmermann et al. "Laser ablation loading of a radiofrequency ion trap". In: *Appl. Phys. B* 107 (4 June 2012), pp. 883–889. ISSN: 0946-2171. DOI: 10.1007/s00340-012-4884-1.

[109] Leonard Nitzsche and Tobias Schaetz. "Ablation Loading of Mg+ in a Surface-Electrode Trap". en. MA thesis.

[110] Xinxin Li and Yingchun Guan. "Theoretical fundamentals of short pulse laser–metal interaction: A review". In: *Nanotechnology and Precision Engineering* 3.3 (Aug. 2020), pp. 105–125. ISSN: 1672-6030. DOI: 10.1016/j.npe.2020.08.001. eprint: https://pubs.aip.org/tu/npe/article-pdf/3/3/105/13882563/105_1_online.pdf. URL: https://doi.org/10.1016/j.npe.2020.08.001.

[111] Matthew S. Brown and Craig B. Arnold. "Fundamentals of Laser-Material Interaction and Application to Multiscale Surface Modification". In: *Laser Precision Microfabrication*. Ed. by Koji Sugioka, Michel Meunier, and Alberto Piqué. Berlin, Heidelberg: Springer Berlin Heidelberg, 2010, pp. 91–120. ISBN: 978-3-642-10523-4. DOI: 10.1007/978-3-642-10523-4_4. URL: https://doi.org/10.1007/978-3-642-10523-4_4.

[112] K. Sheridan, W. Lange, and M. Keller. "All-optical ion generation for ion trap loading". In: *Applied Physics B* 104 (4 Sept. 2011), pp. 755–761. ISSN: 0946-2171. DOI: 10.1007/s00340-011-4563-7.

[113] R. B Blakestad et al. "Near-ground-state transport of trapped-ion qubits through a multidimensional array". In: *Phys. Rev. A* 84 (3 Sept. 2011), p. 032314. DOI: 10.1103/PhysRevA.84.032314. URL: https://link.aps.org/doi/10.1103/PhysRevA.84.032314.

[114] R. Bowler et al. "Coherent Diabatic Ion Transport and Separation in a Multizone Trap Array". In: *Phys. Rev. Lett.* 109 (8 Aug. 2012), p. 080502. DOI: 10.1103/PhysRevLett.109.080502. URL: https://link.aps.org/doi/10.1103/PhysRevLett.109.080502.

[115] T. Ruster et al. "Experimental realization of fast ion separation in segmented Paul traps". In: *Phys. Rev. A* 90 (3 Sept. 2014), p. 033410. DOI: 10.1103/PhysRevA.90.033410. URL: https://link.aps.org/doi/10.1103/PhysRevA.90.033410.

[116] A. Walther et al. "Controlling Fast Transport of Cold Trapped Ions". In: *Phys. Rev. Lett.* 109 (8 Aug. 2012), p. 080501. DOI: 10.1103/PhysRevLett.109.080501. URL: https://link.aps.org/doi/10.1103/PhysRevLett.109.080501.

[117] Carmelo Mordini et al. "Multi-zone trapped-ion qubit control in an integrated photonics QCCD device". In: (Jan. 2024).

[118] J. A. Sedlacek et al. "Method for Determination of Technical Noise Contributions to Ion Motional Heating". en. In: *Journal of Applied Physics* 124.21 (Dec. 2018), p. 214904. ISSN: 0021-8979, 1089-7550. DOI: 10.1063/1.5045326.

[119] Q. A. Turchette et al. "Heating of trapped ions from the quantum ground state". In: *Phys. Rev. A* 61 (6 May 2000), p. 063418. DOI: 10.1103/PhysRevA.61.063418. URL: https://link.aps.org/doi/10.1103/PhysRevA.61.063418.

[120] D. A. Hite et al. "100-Fold Reduction of Electric-Field Noise in an Ion Trap Cleaned with In Situ Argon-Ion-Beam Bombardment". In: *Phys. Rev. Lett.* 109 (10 Sept. 2012), p. 103001. DOI: 10.1103/PhysRevLett.109.103001. URL: https://link.aps.org/doi/10.1103/PhysRevLett.109.103001.

[121] M. Brownnutt et al. "Ion-trap measurements of electric-field noise near surfaces". In: *Rev. Mod. Phys.* 87.4 (Dec. 2015), pp. 1419–1482. DOI: 10.1103/RevModPhys.87.1419. URL: http://link.aps.org/doi/10.1103/RevModPhys.87.1419%20http://journals.aps.org/rmp/pdf/10.1103/RevModPhys.87.1419.

[122] J. A. Sedlacek et al. "Distance scaling of electric-field noise in a surface-electrode ion trap". In: *Phys. Rev. A* 97 (2 Feb. 2018), p. 020302. DOI: 10.1103/PhysRevA.97.020302. URL: https://link.aps.org/doi/10.1103/PhysRevA.97.020302.

[123] Robert Joerdans. *Electrode - GitHub Repository*. https://github.com/nist-ionstorage/electrode. Accessed: 2024-08-22. 2024.

[124] R. Bowler et al. "Arbitrary waveform generator for quantum information processing with trapped ions". In: *Review of Scientific Instruments* 84 (3 Mar. 2013), p. 033108. ISSN: 0034-6748. DOI: 10.1063/1.4795552.

[125] Laurence W. Nagel and D.O. Pederson. *SPICE (Simulation Program with Integrated Circuit Emphasis)*. Tech. rep. UCB/ERL M382. EECS Berkeley, Apr. 1973. URL: http://www2.eecs.berkeley.edu/Pubs/TechRpts/1973/22871.html.

[126] Jaroslaw Labaziewicz et al. "Suppression of Heating Rates in Cryogenic Surface-Electrode Ion Traps". In: *Phys. Rev. Lett.* 100 (1 Jan. 2008), p. 013001. DOI: 10.1103/PhysRevLett.100.013001. URL: https://link.aps.org/doi/10.1103/PhysRevLett.100.013001.

[127] Markus Teller et al. "Heating of a Trapped Ion Induced by Dielectric Materials". In: *Phys. Rev. Lett.* 126 (23 June 2021), p. 230505. DOI: 10.1103/PhysRevLett.126.230505. URL: https://link.aps.org/doi/10.1103/PhysRevLett.126.230505.

[128] Lukas Martinetz, Klaus Hornberger, and Benjamin A. Stickler. "Surface-Induced Decoherence and Heating of Charged Particles". In: *PRX Quantum* 3 (3 Aug. 2022), p. 030327. DOI: 10.1103/PRXQuantum.3.030327. URL: https://link.aps.org/doi/10.1103/PRXQuantum.3.030327.

[129] J. A. Sedlacek et al. "Evidence for multiple mechanisms underlying surface electric-field noise in ion traps". In: *Phys. Rev. A* 98 (6 Dec. 2018), p. 063430. DOI: 10.1103/PhysRevA.98.063430. URL: https://link.aps.org/doi/10.1103/PhysRevA.98.063430.

[130] Crystal Noel et al. "Electric-field noise from thermally activated fluctuators in a surface ion trap". In: *Phys. Rev. A* 99 (6 June 2019), p. 063427. DOI: 10.1103/PhysRevA.99.063427. URL: https://link.aps.org/doi/10.1103/PhysRevA.99.063427.

[131] Ivan A. Boldin, Alexander Kraft, and Christof Wunderlich. "Measuring Anomalous Heating in a Planar Ion Trap with Variable Ion-Surface Separation". en. In: *Phys. Rev. Lett.* 120.2 (Jan. 2018). ISSN: 0031-9007, 1079-7114. DOI: 10.1103/PhysRevLett.120.023201.

[132] Robert McConnell et al. "Reduction of trapped-ion anomalous heating by in situ surface plasma cleaning". In: *Phys. Rev. A* 92 (2 Aug. 2015), p. 020302. DOI: 10.1103/PhysRevA.92.020302. URL: https://link.aps.org/doi/10.1103/PhysRevA.92.020302.

[133] D A Hite, K S McKay, and D P Pappas. "Surface science motivated by heating of trapped ions from the quantum ground state". In: *New Journal of Physics* 23 (10 Oct. 2021), p. 103028. ISSN: 1367-2630. DOI: 10.1088/1367-2630/ac2c2c.

[134] E. Kim et al. "Electric-field noise from carbon-adatom diffusion on a Au(110) surface: First-principles calculations and experiments". In: *Physical Review A* 95 (3 Mar. 2017), p. 033407. ISSN: 2469-9926. DOI: 10.1103/PhysRevA.95.033407.

[135] Heng-Chia Chang et al. "Phase Noise in Coupled Oscillators: Theory and Experiment". en. In: *IEEE Transactions on Microwave Theory and Techniques* 45.5 (May 1997), pp. 604–615. ISSN: 00189480. DOI: 10.1109/22.575575.

[136] Steven A. King et al. "Algorithmic Ground-State Cooling of Weakly Coupled Oscillators Using Quantum Logic". In: *Phys. Rev. X* 11 (4 Dec. 2021), p. 041049. DOI: 10.1103/PhysRevX.11.041049. URL: https://link.aps.org/doi/10.1103/PhysRevX.11.041049.

[137] Pan-Yu Hou et al. "Coherently Coupled Mechanical Oscillators in the Quantum Regime". In: (May 2022).

[138] William Cody Burton et al. "Transport of Multispecies Ion Crystals through a Junction in a Radio-Frequency Paul Trap". In: *Phys. Rev. Lett.* 130 (17 Apr. 2023), p. 173202. DOI: 10.1103/PhysRevLett.130.173202. URL: https://link.aps.org/doi/10.1103/PhysRevLett.130.173202.

[139] R. B. Blakestad et al. "High-Fidelity Transport of Trapped-Ion Qubits through an X-Junction Trap Array". In: *Physical Review Letters* 102 (15 Apr. 2009), p. 153002. DOI: 10.1103/PhysRevLett.102.153002. URL: http://link.aps.org/doi/10.1103/PhysRevLett.102.153002%20http://prl.aps.org/pdf/PRL/v102/i15/e153002.

[140] Kenneth Wright et al. "Reliable transport through a microfabricated X -junction surface-electrode ion trap". In: *New Journal of Physics* 15 (3 Mar. 2013), p. 033004. ISSN: 1367-2630. DOI: 10.1088/1367-2630/15/3/033004.

[141] M. Akhtar et al. "A high-fidelity quantum matter-link between ion-trap microchip modules". In: *Nature Communications* 14 (1 Feb. 2023), p. 531. ISSN: 2041-1723. DOI: 10.1038/s41467-022-35285-3.

[142] V. Kaushal et al. "Shuttling-based trapped-ion quantum information processing". In: *AVS Quantum Science* 2 (1 Feb. 2020). ISSN: 2639-0213. DOI: 10.1116/1.5126186.

[143] Christian L. Arrington et al. "Micro-fabricated stylus ion trap". In: *Review of Scientific Instruments* 84.8 (Aug. 2013), p. 085001. ISSN: 0034-6748. DOI: 10.1063/1.4817304. eprint: https://pubs.aip.org/aip/rsi/article-pdf/doi/10.1063/1.4817304/14782838/085001_1_online.pdf. URL: https://doi.org/10.1063/1.4817304.

[144] S. C. Burd et al. "Experimental Speedup of Quantum Dynamics through Squeezing". In: *PRX Quantum* 5 (2 Apr. 2024), p. 020314. DOI: 10.1103/PRXQuantum.5.020314. URL: https://link.aps.org/doi/10.1103/PRXQuantum.5.020314.

[145] Or Katz and Christopher Monroe. "Programmable Quantum Simulations of Bosonic Systems with Trapped Ions". In: *Phys. Rev. Lett.* 131 (3 July 2023), p. 033604. DOI: 10.1103/PhysRevLett.131.033604. URL: https://link.aps.org/doi/10.1103/PhysRevLett.131.033604.

[146] Justin B. Spring et al. "Boson Sampling on a Photonic Chip". In: *Science* 339.6121 (2013), pp. 798–801. DOI: 10.1126/science.1231692.

[147] Nathan K. Lysne et al. "Individual Addressing and State Readout of Trapped Ions Utilizing Radio-Frequency Micromotion". In: *Phys. Rev. Lett.* 133 (3 July 2024), p. 033201. DOI: 10.1103/PhysRevLett.133.033201. URL: https://link.aps.org/doi/10.1103/PhysRevLett.133.033201.

[148] M Kumph et al. "Operation of a Planar-Electrode Ion-Trap Array with Adjustable RF Electrodes". In: *New J. Phys.* 18.2 (Feb. 2016), p. 023047. ISSN: 1367-2630. DOI: 10.1088/1367-2630/18/2/023047.

[149] R. C. Sterling et al. "Fabrication and operation of a two-dimensional ion-trap lattice on a high-voltage microchip". In: *Nature Communications* 5 (1 Apr. 2014), p. 3637. ISSN: 2041-1723. DOI: 10.1038/ncomms4637.

[150] Colin D. Bruzewicz et al. "Scalable loading of a two-dimensional trapped-ion array". In: *Nature Communications* 7 (1 Dec. 2016), p. 13005. ISSN: 2041-1723. DOI: 10.1038/ncomms13005.

[151] Marco Valentini et al. "Demonstration of two-dimensional connectivity for a scalable error-corrected ion-trap quantum processor architecture". In: *arXiv preprint arXiv:2406.02406* (2024). URL: https://arxiv.org/abs/2406.02406.

[152] Alejandro Bermudez, Tobias Schaetz, and Diego Porras. "Photon-Assisted-Tunneling Toolbox for Quantum Simulations in Ion Traps". en. In: *New J. Phys.* 14.5 (May 2012), p. 053049. ISSN: 1367-2630. DOI: 10.1088/1367-2630/14/5/053049.

[153] S. C. Burd et al. "Experimental Speedup of Quantum Dynamics through Squeezing". In: *PRX Quantum* 5 (2 Apr. 2024), p. 020314. DOI: 10.1103/PRXQuantum.5.020314. URL: https://link.aps.org/doi/10.1103/PRXQuantum.5.020314.

[154] Wenchao Ge et al. "Trapped Ion Quantum Information Processing with Squeezed Phonons". In: *Phys. Rev. Lett.* 122.3 (Jan. 2019), p. 030501. ISSN: 0031-9007. DOI: 10.1103/PhysRevLett.122.030501. URL: https://link.aps.org/doi/10.1103/PhysRevLett.122.030501.

[155] D. Porras and J. I. Cirac. "Quantum Manipulation of Trapped Ions in Two Dimensional Coulomb Crystals". In: *Phys. Rev. Lett.* 96 (25 June 2006), p. 250501. DOI: 10.1103/PhysRevLett.96.250501. URL: https://link.aps.org/doi/10.1103/PhysRevLett.96.250501.

[156] Tobias Schaetz. "Trapping ions and atoms optically". In: *J. Phys. B At. Mol. Opt. Phys.* 50.10 (May 2017), p. 102001. ISSN: 0953-4075. DOI: 10.1088/1361-6455/aa69b2. URL: http://stacks.iop.org/0953-4075/50/i=10/a=102001?key=crossref.3eaf9fc0889da7f183d3b55e90b037bb.

[157] Ch Schneider et al. "Optical Trapping of an Ion". In: *Nat. Phot.* 4 (2010), p. 772.

[158] Julian Schmidt et al. "Optical Trapping of Ion Coulomb Crystals". In: *Phys. Rev. X* 8 (2 May 2018), p. 021028. DOI: 10.1103/PhysRevX.8.021028. URL: https://link.aps.org/doi/10.1103/PhysRevX.8.021028.

[159] Daniel Hoenig et al. "Trapping Ion Coulomb Crystals in an Optical Lattice". In: *Phys. Rev. Lett.* 132 (13 Mar. 2024), p. 133003. DOI: 10.1103/PhysRevLett.132.133003. URL: https://link.aps.org/doi/10.1103/PhysRevLett.132.133003.

[160] Jeremy M. Sage, Andrew J. Kerman, and John Chiaverini. "Loading of a surface-electrode ion trap from a remote, precooled source". In: *Phys. Rev. A* 86 (1 July 2012), p. 013417. DOI: 10.1103/PhysRevA.86.013417. URL: https://link.aps.org/doi/10.1103/PhysRevA.86.013417.

[161] Marko Cetina et al. "Bright source of cold ions for surface-electrode traps". In: *Phys. Rev. A* 76 (4 Oct. 2007), p. 041401. DOI: 10.1103/PhysRevA.76.041401. URL: https://link.aps.org/doi/10.1103/PhysRevA.76.041401.

[162] Sumit Tewari and Andrew Webb. "The permanent magnet hypothesis: an intuitive approach to designing non-circular magnet arrays with high field homogeneity". In: *Scientific Reports* 13 (1 Feb. 2023), p. 2774. ISSN: 2045-2322. DOI: 10.1038/s41598-023-29533-9.

[163] U. Warring et al. "Individual-Ion Addressing with Microwave Field Gradients". In: *Phys. Rev. Lett.* 110 (17 Apr. 2013), p. 173002. DOI: 10.1103/PhysRevLett.110.173002. URL: https://link.aps.org/doi/10.1103/PhysRevLett.110.173002.

[164] J. Chiaverini and W. E. Lybarger. "Laserless trapped-ion quantum simulations without spontaneous scattering using microtrap arrays". In: *Phys. Rev. A* 77.2 (Feb. 2008), p. 022324. DOI: 10.1103/PhysRevA.77.022324. URL: http://link.aps.org/doi/10.1103/PhysRevA.77.022324%20http://pra.aps.org/pdf/PRA/v77/i2/e022324.

[165] C. Ospelkaus et al. "Microwave quantum logic gates for trapped ions". In: *Nature* 476 (7359 2011), pp. 181–184. DOI: 10.1038/nature10290.

[166] R. Srinivas et al. "High-fidelity laser-free universal control of trapped ion qubits". In: *Nature* 597 (7875 Sept. 2021), pp. 209–213. ISSN: 0028-0836. DOI: 10.1038/s41586-021-03809-4.

[167] L. Feng et al. "Efficient Ground-State Cooling of Large Trapped-Ion Chains with an Electromagnetically-Induced-Transparency Tripod Scheme". In: *Phys. Rev. Lett.* 125 (5 July 2020), p. 053001. DOI: 10.1103/PhysRevLett.125.053001. URL: https://link.aps.org/doi/10.1103/PhysRevLett.125.053001.

[168] S. L. Todaro et al. "State Readout of a Trapped Ion Qubit Using a Trap-Integrated Superconducting Photon Detector". In: *Phys. Rev. Lett.* 126 (1 Jan. 2021), p. 010501. DOI: 10.1103/PhysRevLett.126.010501. URL: https://link.aps.org/doi/10.1103/PhysRevLett.126.010501.

[169] J. I. Cirac and P. Zoller. "Goals and Opportunities in Quantum Simulation". In: *Nat. Phys.* 8.4 (Apr. 2012), p. 264. DOI: 10.1038/nphys2275.